FUNCTIONAL MATERIALS FOR CHLORIDE REMOVAL AND ANTIMICROBIAL APPLICATIONS IN WATER TREATMENT

SAMA KHALILI MORADKHANLOO

A THESIS SUBMITTED TO THE FACULTY OF GRADUATE

STUDIES IN PARTIAL FULFILLMENT OF THE REQUIREMENTS

FOR THE DEGREE OF MASTER OF APPLIED SCIENCE

GRADUATE PROGRAM IN CIVIL ENGINEERING

YORK UNIVERSITY

TORONTO, ONTARIO

September 2026

©Sama Khalili Moradkhanloo, 2026

Abstract

Road salt application and microbial contamination pose significant challenges to freshwater quality, requiring sustainable and multifunctional treatment technologies. This thesis investigates bio-inspired materials for chloride removal and antimicrobial water treatment through a review and two experimental studies. A comprehensive review of nanoflower-based membrane technologies established a structure-transport-reactivity framework that guided the development of functional materials. A biochar-supported curcumin-copper phosphate hybrid nanoflower (BC-NFs) composite was successfully synthesized and characterized using SEM, EDS, XRD, FTIR, fluorescence microscopy, and BET analysis, confirming the formation of hierarchical nanoflowers uniformly distributed on the biochar surface. The composite exhibited strong antibacterial activity against Escherichia coli but limited chloride adsorption. To address chloride contamination, a sustainable eggshell–superabsorbent polymer (SAP-EGS) composite was developed, achieving 63.13% and 44.1% removal for the targeted water sample chloride removal under optimized conditions and maintaining effective performance over five adsorption–desorption cycles. Collectively, these studies demonstrate the potential of waste-derived, multifunctional materials for sustainable freshwater treatment and environmental remediation.

Dedication

To my husband, Ashkan, for your unwavering love, endless support, and constant encouragement.

Acknowledgement

I would like to express my sincere gratitude to my supervisor, Professor Satinder Kaur Brar, for her mentorship, guidance, and continuous support throughout my master's studies. Her expertise and encouragement have been instrumental in shaping this research and my academic development.

I would also like to express my sincere appreciation to my co-supervisor, Professor Siu-Ning Leung, for his insightful advice, constructive feedback, and continuous encouragement throughout this research. My heartfelt thanks also go to my mentor, Dr. Ratul Das, whose technical expertise, thoughtful discussions, and dedicated support greatly contributed to the success of this work.

I am sincerely grateful to my supervisory committee members, Professor Pulin Mondal and Professor Paul G. O'Brien, for their valuable comments, constructive suggestions, and careful evaluation, which significantly strengthened the quality of this thesis.

I am deeply thankful to my family for their unconditional love, endless patience, unwavering encouragement, and constant belief in me. Their support has been my greatest source of strength throughout this journey. I also thank my friends, colleagues, laboratory members, and the Inzymes Research Group for fostering a collaborative and inspiring research environment. My appreciation also extends to the technical staff for their expertise and assistance throughout the experimental work.

Finally, I gratefully acknowledge the financial support provided by the Natural Sciences and Engineering Research Council of Canada (NSERC), the City of Markham, and the James and Joanne Love Chair in Environmental Engineering. Their generous support made this research possible.

Table of Contents:

Abstract ..... **ii**

Dedication ..... **iii**

Acknowledgement ..... **iv**

Table of Contents: ..... **v**

Table of Figures ..... **x**

Table of Tables ..... **xvi**

Abbreviations: ..... **xvii**

Publications Within this Thesis ..... **xxi**

Publications Outside this Thesis ..... **xxi**

Chapter 1: Background ***1***

1.1 Introduction **1**

1.2 Literature Review **8**

1.2 8

2. Integration of NFs into Membranes 8

1.2.2.1 Working Mechanism 8

1.2.2.2. Technical challenges in fabricating commercial membranes for specific uses: Conventional modalities and NF-based membranes 25

1.2.2.3. Selection of Membrane Materials (Organic or Ceramic) for NF Integration 33

1.2.2.4. Local Membrane Properties: How NF-Based Membranes Work 38

1.2.3. Recent Developments in NF-Based Membranes for Water and Wastewater Treatments 40

1.2.3.1. Recent studies 40

1.2.3.2. Application-Based Case Studies at Lab Scale 41

1.2.4.2. Challenges for Real-World Deployment 50

1.2.5. Future Directions and Opportunities 54

1.2.6. Conclusion 57

1.3 Proposed Research 59

1.3.1 Research Gap 59

1.3.2 Objectives 61

1.3.3 Novelty 62

Chapter 2: Biochar-Supported Curcumin-Copper Phosphate Hybrid Nanoflowers: Synthesis, Characterization and Antibacterial Performance 64

2.1 Introduction 64

2.2. Materials and Methods 67

2.2.1 Materials 67

2.2.2 Synthesis of Curcumin–Copper Phosphate Hybrid Nanoflowers (CCPHNFs) 68

2.2.3 Synthesis of Biochar-Supported Nanoflowers (BC-NFs) 68

2.2.4 Material Characterization 69

2.2.5 Antibacterial Activity 70

2.3. Results and Discussion 71

2.3.1 Characterization of CCPHNFs 71

2.3.1.1 Morphological Analysis (SEM) 71
2.3.1.2 Crystal Structure Analysis (XRD) 74
2.3.1.3 Functional Group Analysis (FTIR) 75
2.3.1.4 Fluorescence Microscopy 77
2.3.2 Characterization of Biochar-Supported Nanoflowers (BC-NFs) 78
2.3.2.1 Morphological Analysis (SEM) 78
2.3.2.2 Elemental Composition and Elemental Mapping Analysis 80
2.3.2.3 Fluorescence Microscopy 81
2.3.2.4 Functional Group Analysis (FTIR) 84
2.3.2.5 Surface Area and Porosity Analysis (BET) 85
2.3.3 Antibacterial Activity Against Escherichia coli 88
2.3.4. Environmental relevance and potential application 91
2.4. Conclusion 94
Chapter 3: Eggshell-Superabsorbent Polymer Composite for Chloride Mitigation in Road Salt-Impacted Freshwater 96
3.1 Introduction 96
3.2 Experimental Materials and Methods 100
3.2.1 Materials 100
3.2.2 Synthesis of SAP-EGS Composite 101
3.2.3 Physicochemical characterization of SAP-EGS Hydrogel 102
3.2.4 Study of Swelling and Adsorption 103
3.2.5. Adsorption Isotherm Analysis 104
3.2.6. SAP-EGS Reusability Test 105

3.2.7. Statistical Analysis 106

3.3. Results and discussion 106

3.3.1 Optimization of EGS Concentration and Monomer Ratio 106

3.3.2 Physicochemical characterization 110

3.3.2.1 Chemical Structure Analysis 110

3.3.2.2 Morphological Analysis 113

3.3.2.3 Energy-Dispersive X-ray Spectroscopy (EDS) 114

3.3.3 Chloride Adsorption Performance 119

3.3.4 Effect of Initial Chloride Concentration 120

3.3.5 Equilibrium Isotherm Analysis 122

3.3.6 Reusability Test 125

3.4 Conclusion 126

Chapter 4: Conclusion and future work 128

4.1 Conclusion 128

4.2. Future Work 129

References: 132

APPENDICES 147

APPENDIX A: Experimental Challenges 147

Preliminary Investigations on Biochar for Chloride Removal 147

Surface Functionalization of Biochar for Chloride Removal 148

APPENDIX B: Supplementary information for Chapter 2 150

APPENDIX C: Supplementary information for Chapter 3 152

Preliminary Chloride Removal Using Eggshell Powder 152

Study of Swelling and Adsorption 153

Absorption Isotherm Analysis 158

Table of Figures

Figure 1- Key properties and applications of NFs in water and wastewater purification..... 3

Figure 2. PRISMA-style schematic of the study selection procedure. 7

Figure 3- Schematic illustration of NECMs by proposing the incorporation of polymers and Nanomaterials, and the working mechanism of NECMs in water/wastewater purification consisting of (A) adsorption (B) and separation 9

Figure 4- Dual mechanisms of NF-modified membranes: hydrophilicity enhancement and surface charge engineering. 21

Figure 5- Key mechanisms-nanosheet petals, defects, and electronic coupling-that narrow the band gap in NFs. 25

Figure 6- Typical membranes utilized for water/wastewater purification 36

Figure 7- Fabrication of some NF-based membrane a) Schematic illustration of the ZnO NF@SiC membrane preparation.(J. Wei et al., 2022) b) Growing mechanism of Cu3(PO4)2·3H2O-protein nanoflowers (M. Li et al., 2016) c) Fabrication process of the DP/COF3/PVDF membrane, utilizing LBL self-assembly and co-deposition techniques.(Dai, Ding, et al., 2024) d) Fabrication of the NF-embedded EVAL nanofiber layer and the growth of Cu3(PO4)2-TR hybrid NF.(Ye et al., 2024) e) Fabrication process of the hierarchically porous nanofibrous membrane.(Luo et al., 2020) f) preparation of ultrahigh antifouling ultrafiltration membrane based on Ag NPs photoreduction modified PVP/BiOCl NF for efficient membrane fouling removal. (Gao et al., 2025). Adapted with permission from Refs. 7, 84, 34, 11, 39, and 62. Copyright permissions obtained from the respective copyright holders. 46

Figure 8- Fabrication of some NF-based membrane a) Fabrication of some NF-based membrane. Schematic illustration for the synthesis of BP/CoNiSe2. (Wen et al., 2025). b) Schematic diagram

of the heterogeneous CoAl-LDH@PANI/pPAN fibrous composite membrane(F. Zhu et al., 2024). c) Schematic diagram of the preparation process of Self-assembled NF-mediated interfacial polymerization through tunable intra- and inter-layer channels(Chen et al., 2025). d) Schematic illustration of the preparation process of PA/COF2/PES membranes(Dai, Hu, et al., 2024a). e) Illustration of the preparation proedure for the ZnCo-LDH@PAN membrane and Formation schematic of ZnCo-LDH nanoparticles on PAN nanofibers(S. Li et al., 2023). f) Schematic diagram of Carbon quantum dots-decorated ZnO heterostructure NFs grown on nanofiber membranes (H. Xu et al., 2023). Adapted with permission from Refs. 76, 83, 74, 20, 75, and 26. Copyright permissions obtained from the respective copyright holders. 49

Figure 9- Morphological and structural characterization of n CPHNFs and CCPHNFs synthesized at different $CuSO_4$ concentrations. SEM images of CCPHNFs synthesized using, (a) 5 mM, (b) 10 mM, (c) 25 mM, (d) 50 mM, (e) 100 mM, and (f) 200 mM $CuSO_4$ and, SEM images of CCPHNFs synthesized using, (g) 5 mM, (h) 10 mM, (i) 25 mM, (j) 50 mM, (k) 100 mM, and (l) 200 mM $CuSO_4$ in the presence of 0.5 μM curcumin. Three representative SEM images (m) at different magnifications are presented for the 100 mM sample to highlight the hierarchical flower-like morphology. 74

Figure 10- X-ray diffraction (XRD) patterns comparing the synthesized copper phosphate nanoflowers with the reference crystalline copper phosphate phase, confirming the successful formation of crystalline CCPHNFs..... 75

Figure 11-a) FTIR spectra of nanoflowers synthesized with and without curcumin. (b) Bright-field optical microscopy image of the synthesized nanoflowers. (c) Fluorescence microscopy image showing the green fluorescence emitted by curcumin. 78

Figure 12- SEM images of the BC-NFs composite at different magnifications, demonstrating the successful incorporation and distribution of hierarchical copper phosphate nanoflowers on the porous biochar surface. (a) 200×, (b) 1,000×, (c) 1,200×, (d) 2,800×, (e) 2,800×, and (f) 10,000×. (g) Elemental mapping obtained by EDS analysis illustrating the distribution of C, Cl, O, Cu, P, S, Ca, and K within the BC-NFs composite. (h) Corresponding EDS spectrum. (i) Bright-field optical microscopy image, scale bar: 1 mm, and (j) fluorescence microscopy image through characteristic green fluorescence. Scale bars: 1 mm. 84

Figure 13. FTIR spectra of pristine biochar and the BC-NFs composite. 85

Figure 14- Antibacterial activity of BC-NFs and CCPHNFs against Escherichia coli was evaluated by the agar well diffusion method at concentrations of 100 and 200 mg mL^{-1} after incubation at 30 °C for 24 h..... 89

Figure 15- Antibacterial activity of the BC-NFs composite against Escherichia coli evaluated by the agar well diffusion method. The agar plate shows the inhibition zones produced by BC-NFs, ciprofloxacin (positive control), and deionized (DI) water (negative control) after incubation at 30 °C for 72 h..... 90

Figure 16- a) Effect of EGS loading on chloride removal performance of the SAP-EGS hydrogel. Error bars represent mean ± SD (n = 3). Different letters indicate significant differences ($p < 0.05$). b) Effect of acrylic acid-to-acrylamide ratio on chloride removal performance of the SAP-EGS hydrogel. Error bars represent mean ± SD (n = 3). Different letters indicate significant differences ($p < 0.05$)..... 108

Figure 17- FTIR spectra of (a) raw EGS, (b) SAP-EGS composite hydrogel before chloride adsorption, and (c) SAP-EGS hydrogel after chloride removal, showing the characteristic functional groups and chemical interactions associated with chloride removal. 112

Figure 18- Morphological and elemental characterization of the synthesized materials. SEM micrographs of the SAP–EGS composite hydrogel at different magnifications (a–f), pristine SAP hydrogel (g–i), and raw EGS powder (j). EDS spectra of pristine SAP (k), SAP–EGS composite before chloride removal (l), and SAP–EGS composite after chloride removal (m), confirming the incorporation of EGS-derived calcium into the hydrogel matrix and the presence of chloride following treatment. 118

Figure 19- Effect of initial chloride concentration on the equilibrium chloride uptake capacity of EGS and the SAP–EGS composite. 122

Figure 20- Adsorption isotherm analysis of chloride removal by the SAP-EGS hydrogel: (a) Langmuir isotherm model and (b) Freundlich isotherm model fitted to the experimental equilibrium data. 124

Figure 21- Reusability of the optimized SAP-EGS hydrogel over consecutive adsorption–desorption cycle 126

Figure 22- AgCl Precipitation on Biochar 148

Figure 23- Schematic illustration of the synthesis and antibacterial evaluation of the biochar-supported curcumin–copper phosphate hybrid nanoflowers (BC–NFs). Curcumin and $CuSO_4$ were self-assembled in phosphate-buffered saline (PBS) to form copper phosphate hybrid nanoflowers directly on the biochar surface. The resulting BC–NFs composite was characterized by SEM and evaluated for antibacterial activity against Escherichia coli using the agar well diffusion method, with ciprofloxacin (CIP) and deionized (DI) water serving as the positive and negative controls, respectively. 150

Figure 24- SEM images of CCPHNFs synthesized using 100 mM $CuSO_4$ in the presence of 0.5 μM curcumin. Four representative SEM images at different magnifications. 151

Figure 25- Antibacterial activity of the biochar-supported curcumin–copper phosphate hybrid nanoflowers (BC–NFs) against Escherichia coli determined by the agar well diffusion assay after **(a)** 18 h and **(b)** 4 days of incubation. The BC–NFs composite maintained a distinct inhibition zone over the incubation period, indicating sustained antibacterial activity. 151
Figure 26- White salt precipitate observed following the preliminary chloride removal experiment using EGS powder after methanol extraction and cooling at 4 °C. 153
Figure 27- Proposed mechanism of chloride removal by the SAP–EGS. (a) The SAP–EGS hydrogel absorbs chloride-containing water while calcium ions are gradually released from the incorporated EGS particles. (b) Methanol addition promotes water desorption from the swollen hydrogel, increasing ion concentration and facilitating interactions between calcium and chloride ions. (c) Upon cooling at 4 °C, calcium-assisted chloride precipitation occurs within the hydrogel matrix, enabling chloride removal from the aqueous phase. 153
Figure 28- Raw triplicate measurements of the final chloride concentration for different EGS loadings used during optimization of the SAP–EGS composite. Each treatment was performed in triplicate (n = 3) under identical experimental conditions. 154
Figure 29- Raw triplicate measurements of the final chloride concentration for different acrylamide (AM) contents during optimization of the SAP–EGS composite. Each formulation was tested in triplicate (n = 3) under identical experimental conditions. 154
Figure 30- Effect of the initial chloride concentration on the chloride removal performance of the optimized SAP–EGS composite. Bars represent the final chloride concentration after treatment, while the line indicates the corresponding chloride reduction efficiency. Error bars represent the standard deviation of triplicate measurements (n = 3). 155

Figure 31- Raw triplicate measurements of the final chloride concentration obtained during five consecutive adsorption–desorption cycles of the optimized SAP–EGS composite. Each cycle was performed in triplicate (n = 3) to evaluate the reusability and stability of the composite. 155
Figure 32- Representative photographs of the SAP–EGS hydrogel (a) before and (b) after the chloride removal experiment, illustrating the physical appearance of the composite following adsorption and methanol-assisted chloride precipitation. 156
Figure 33- Water Sampling Procedure and Sampling Locations at Swan Lake, Markham, Ontario. (a) Preparation of the water sampling device prior to collection. (b) Collection of water samples from the lake using a depth sampler. (c) Transfer of collected water into a clean sample bottle for laboratory analysis. (d) Aerial map of Swan Lake showing the water sampling locations, including the Bridge and Dock sampling sites..... 157

Table of Tables

Table 1. Classification of three-dimensional NFs based on composition, morphology, synthesis method, and membrane integration route. 4

Table 2. Comparison of key parameters between conventional membranes and NF-based membranes 30

Table 3. comparative summary of representative nanoflower-based membrane systems for water and wastewater treatment. 43

Table 4. FTIR absorption bands and corresponding functional group assignments of CCPHNFs synthesized with and without curcumin. 76

Table 5. Characteristic FTIR absorption bands of pristine biochar and the BC-NFs composite.. 84

Table 6. BET surface area and pore characteristics of pristine BC, CCPHNF, and BC-NFs. 87

Table 7. Antibacterial activity of BC-NFs and CCPHNFs against Escherichia coli determined by the agar well diffusion method. 88

Table 8. Antibacterial activity of BC-NFs against Escherichia coli determined by the agar well diffusion method. 89

Table 9. Equilibrium adsorption isotherm parameters for chloride removal by the SAP-EGS hydrogel obtained from the Langmuir and the Freundlich models. 124

Table 10. Experimental equilibrium chloride concentrations (Ce), adsorption capacities (qe), and transformed parameters used for Freundlich and Langmuir adsorption isotherm modeling. 158

Abbreviations:

AA	Acrylic acid
AM	Acrylamide
ANOVA	Analysis of variance
AOPs	Advanced oxidation processes
APS	Ammonium persulfate
ATR	Attenuated total reflectance
BC	Biochar
BC–NFs	Biochar-supported curcumin–copper phosphate hybrid nanoflowers
BET	Brunauer–Emmett–Teller (surface area analysis)
BIEF	Built-in electric field
CCPHNFs	Curcumin–copper phosphate hybrid nanoflowers
CNT	Carbon nanotube
COF	Covalent organic framework
CTS	Chitosan
DI	Deionized
DP	Dopamine
DR3900	Hach DR3900 spectrophotometer
EDS	Energy-dispersive X-ray spectroscopy
EGS	Eggshell
EVAL	Ethylene-vinyl alcohol copolymer
FESEM	Field-emission scanning electron microscopy
FTIR	Fourier-transform infrared spectroscopy

GO	Graphene oxide
JCPDS	Joint Committee on Powder Diffraction Standards
KBr	Potassium bromide
LBL	Layer-by-layer
LDH	Layered double hydroxide
MBA	N,N′-Methylenebisacrylamide
MF	Microfiltration
MOF	Metal-organic framework
MW	Wet membrane mass
MD	Dry membrane mass
NF	Nanoflower
NECMs	Nano-enhanced composite membranes
NMs	Nanomaterials
NSERC	Natural Sciences and Engineering Research Council of Canada
PA	Polyamide
PAM	Polyacrylamide
PAN	Polyacrylonitrile
PBS	Phosphate-buffered saline
PEI	Polyethyleneimine
PDI	Perylene diamide
PES	Polyether sulfone
PSf	Polysulfone
PSO	Pseudo-second order

PVA	Poly (vinyl alcohol)
PVDF	Poly (vinylidene fluoride)
PVP	Polyvinylpyrrolidone
qe	Equilibrium adsorption capacity
qmax	Maximum adsorption capacity
R^2	Coefficient of determination
RO	Reverse osmosis
ROS	Reactive oxygen species
SAP	Superabsorbent polymer
SAP–EGS	Superabsorbent polymer–eggshell composite
SD	Standard deviation
SEM	Scanning electron microscopy
SERS	Surface-enhanced Raman spectroscopy
TFC	Thin-film composite
TNT879	Hach TNT879 Chloride Test Kit
UF	Ultrafiltration
UV	Ultraviolet
XRD	X-ray diffraction
ZnO	Zinc oxide
TiO_2	Titanium dioxide
CuO	Copper(II) oxide
Fe_3O_4	Magnetite (iron oxide)
MnO_2	Manganese dioxide

BiOBr	Bismuth oxybromide
$Zr(OH)_x$	Zirconium hydroxide
eV	Electron volt

Publications Within this Thesis

S. Khalili Moradkhanloo, R.K Das, S. Leung, S.K Brar, Recent Advances in Three-Dimensional Nanoflower-Based Membrane Engineering for Water and Wastewater Treatment: From Fundamental Mechanisms to Large-Scale Applications, Reviews in RSC Advances. IF: 6.1 (Accepted)

S. Khalili Moradkhanloo, R.K Das, S. Leung, S.K Brar, Biochar Supported Curcumin Copper Phosphate Hybrid Nanoflowers with Antibacterial Activity, (submitted, Materials Chemistry and Physic, September 2026)

S. Khalili Moradkhanloo, R.K Das, S. Leung, S.K Brar, Eggshell-Superabsorbent Polymer Composite for Chloride Mitigation in Road Salt-Impacted Freshwater, (to be submitted, October 2026)

Publications Outside this Thesis

Moradkhanloo, S.K., Brar, S.K. (2026). Advanced Treatment Processes for Wastewater for Potable Reuse. In: The Handbook of Environmental Chemistry. Springer, Berlin, Heidelberg. https://doi.org/10.1007/698_2025_1247

Moradkhanloo, S.K., Brar, S.K. (2026). Sludge Reuse in Afforestation and Land Application. In: The Handbook of Environmental Chemistry. Springer, Berlin, Heidelberg. https://doi.org/10.1007/698_2026_1264

Moradkhanloo, S.K., Brar, S.K. Common Treatment Techniques for Wastewater Purification. Chapter 2. In: Conventional and Advanced Technologies for the Reuse of Treated Wastewater. In S. K. Brar, A. S. Dhoble, A. Eldyasti, & S. Chatterjee (Eds.). Elsevier. (Accepted/In Press; Publication scheduled for November 8, 2026

Chapter 1: Background

Recent Advances in Three-Dimensional Nanoflower-Based Membrane Engineering for Water and Wastewater Treatment: From Fundamental Mechanisms to Scale-Up

Sama Khalili Moradkhanloo, Ratul Kumar Das, Siu-Ning Leung, Satinder Kaur Brar

(Accepted)

1.1 Introduction

Nanotechnology has emerged as a revolutionary field in modern science, enabling the design, synthesis, and manipulation of nanoscale materials for diverse applications, including healthcare, environmental science, catalysis, and energy storage. Among the various nanostructured materials, nanoflowers (NFs) represent a significant advancement due to their unique three-dimensional (3D) morphology, high surface-to-volume ratio, and enhanced catalytic and adsorption properties. These attributes make NFs particularly attractive for applications in biosensing, drug delivery, wastewater treatment, and energy conversion. The concept of NFs has evolved through extensive research in nanotechnology and materials science. Originally developed as a class of nanostructures that mimic the morphology of natural flowers, NFs have attracted significant attention due to their enhanced physicochemical properties. Early studies focused on the synthesis of inorganic and organic-inorganic hybrid NFs, which subsequently enabled a broad expansion of their applications across biomedical and industrial fields (Cui & Jia, 2017; Ekata et al., n.d.; Jafari-Nodoushan et al., 2022a).

Subsequent research has focused on improving their synthesis methods, optimizing their structural features, and broadening their practical applications (Jafari-Nodoushan et al., 2022a). NFs exhibit flower-like architectures composed of multiple petal-like nanosheets, providing a high specific

surface area and abundant active sites for interaction with target molecules. These structures can be composed of various metal oxides (e.g., zinc oxide, copper oxide, iron oxide), biomolecules (e.g., proteins, enzymes), or hybrid organic-inorganic materials (Ge et al., 2012a; S. Y. Lee et al., 2024a). The composition of NFs determines their functional properties, such as catalytic activity, stability, and biocompatibility, making them suitable for diverse applications in medicine and environmental science (Wu et al., 2018) NFs offer several advantages that make them superior to other nanostructured materials. Examples from recent studies clearly demonstrate why NFs outperform many other nanostructured materials. For instance, ZnO NFs show significantly higher adsorption capacities for heavy metals compared to spherical or rod-shaped ZnO nanoparticles due to their multilayered petal architecture that exposes more active sites. $Cu_3(PO_4)_2$ NFs exhibit superior catalytic activity in phosphatase-mimicking reactions because their hierarchical surfaces facilitate rapid substrate diffusion and strong surface complexation, a performance not achievable with conventional nanoparticle clusters. In photocatalysis, TiO_2 NFs demonstrate enhanced charge carrier separation and reduced electron-hole recombination relative to TiO_2 nanotubes or nanospheres, leading to faster degradation rates of organic pollutants. Additionally, enzyme-NF hybrid structures, such as protein-inorganic NFs, provide high enzymatic stability and reusability compared to free enzymes or simple enzyme immobilization on flat substrates. Collectively, these examples illustrate that the hierarchical, high specific surface area, and multiscale porosity of NFs can promote adsorption, catalytic, and photochemical performance compared with many other nanoscale morphologies (Dadi et al., 2020; Y. Li et al., 2025; G. Song et al., 2021a; J. Wei et al., 2022; Widiyandari et al., 2023; Ye et al., 2024; Yıldırım et al., 2025). The petal-like structure of NFs provides a larger surface area, enhancing their adsorption capacity and catalytic efficiency (J. Zhu et al., 2018a). Hybrid NFs incorporating biomolecules demonstrate enhanced stability, making

them promising candidates for biomedical applications (Y. Li et al., 2025). The 3D structure of NFs facilitates better charge carrier mobility, which is crucial for applications such as surface-enhanced Raman spectroscopy (SERS) and photocatalysis (Hang et al., 2024). In this context, NFs are widely used in drug delivery, biosensing, environmental remediation, and energy storage (H. Liang et al., 2024; Rahbari-Sisakht & Ismail, 2025b).

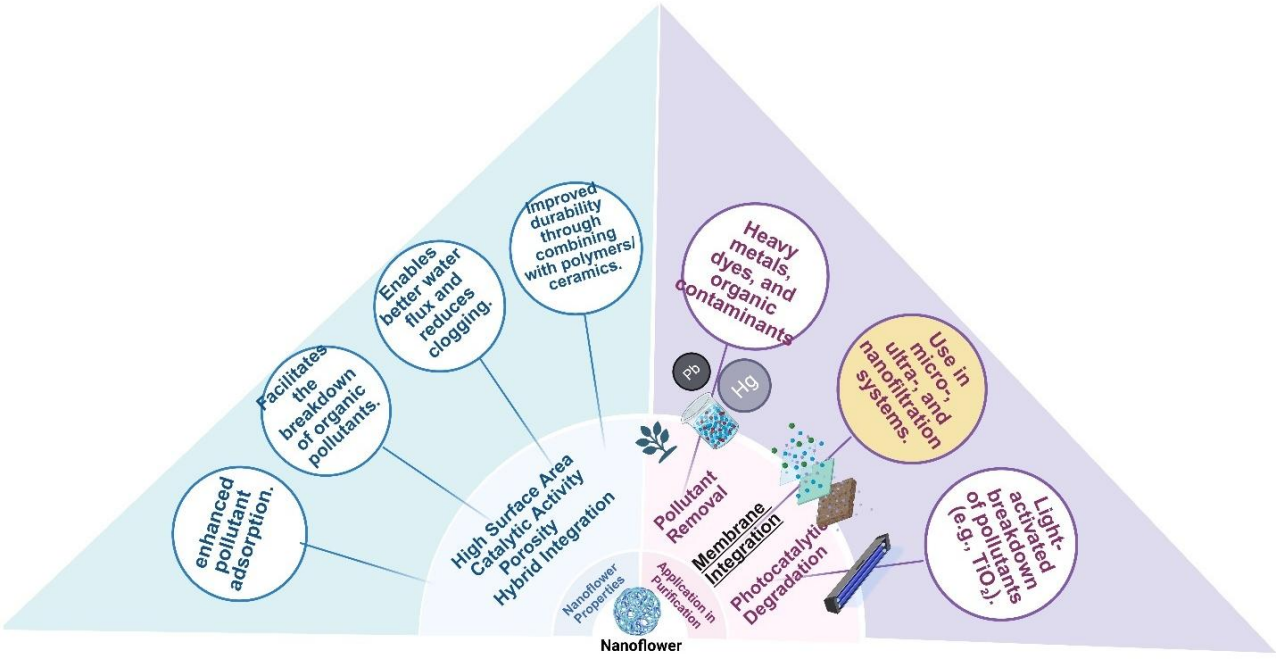

Figure 1- Key properties and applications of NFs in water and wastewater purification.

Application of NFs in water treatment is based on their ability to efficiently remove dyes, heavy metals, and organic pollutants, making them a promising class of materials for sustainable environmental remediation. The development of NFs has been propelled by recent advances in material science, emphasizing structural optimization and functionalization to enhance their performance in water treatment applications (Ahmad et al., 2024; Dai, Hu, et al., 2024a; Kataria & Garg, 2018; S. Y. Lee et al., 2024a; Nayak et al., 2023; Petriev et al., 2021; Widiyandari et al., 2023). NFs exhibit interface properties that make them highly effective in water purification. Their high porosity and layered structure facilitate efficient interaction with contaminants, thereby

enhancing adsorption and catalytic degradation. Metal oxide-based NFs, such as ZnO, CuO, and Fe_3O_4, are widely used due to their photocatalytic properties, enabling the breakdown of complex organic pollutants under visible or UV light (Dai, Hu, et al., 2024a; Shende et al., 2018; Vo et al., 2024). Customization of NFs for water treatment involves tailoring their chemical composition, surface functionalization, and hybridization with biomolecules or other nanomaterials to enhance selectivity and efficiency.

Table 1. Classification of three-dimensional NFs based on composition, morphology, synthesis method, and membrane integration route.

Nanoflower class	**Representative composition**	**Typical flower size (µm)**	**Petal thickness (nm)**	**Common synthesis method**	**Membrane integration route**	**Reference**
Metal oxide NFs	ZnO, TiO_2, CuO, Fe_2O_3, MnO_2, SnO_2	~0.2–5	10–100	Hydrothermal, solvothermal, sol–gel, co-precipitation, green synthesis	Blending, surface coating, and interfacial polymerization	(Kataria & Garg, 2018; Kaur & Kaur, 2022a; X. Li et al., 2023; Y. Liu et al., 2024a; J. Wei et al., 2022; Widiyandari et al., 2023; Witoon et al., 2018; H. Xu et al., 2023)
Metal phosphate NFs	$Cu_3(PO_4)_2$, $Co_3(PO_4)_2$, $Zn_3(PO_4)_2$	~0.5–10	20–200	Biomimetic mineralization, self-assembly	Surface immobilization, in situ growth, mixed-matrix membranes	(G. Song et al., 2021a; Yilmaz et al., 2022)

Nanoflower class	Representative composition	Typical flower size (μm)	Petal thickness (nm)	Common synthesis method	Membrane integration route	Reference
Layered double hydroxide (LDH) NFs	NiCu-LDH, MgAl-LDH, ZnAl-LDH	~0.5–3	5–50	Hydrothermal, co-precipitation	Thin-film nanocomposite (TFN), mixed-matrix membranes	(Guo et al., 2025; J. Zhang et al., 2024; J. Zhao et al., 2024; J. Zhu et al., 2018a)
Metal–organic framework (MOF) NFs	ZIF-8, MIL-series, UiO-based NFs	~0.3–5	20–100	Solvothermal, self-assembly	Interfacial polymerization, TFN membranes	(J. Zhao et al., 2024)
Covalent organic framework (COF) NFs	COF nanoflowers	~0.2–2	20–80	Solvothermal/interfacial synthesis	Thin-film nanocomposite membranes	(Dai, Ding, et al., 2024; Dai, Hu, et al., 2024a; Jafari-Nodoushan et al., 2022a)
MXene-based hierarchical NFs	MXene/NiCu-LDH composites	~0.5–3	Nanosheet petals	Hydrothermal/self-assembly	Surface deposition, composite membranes	(L. Di et al., 2024; Tabesh, Grumme, et al., 2025)
Organic–inorganic hybrid NFs	Protein/$Cu_3(PO_4)_2$, enzyme/phosphate hybrids	~1–20	Nanopetal assemblies	Biomimetic self-assembly	Immobilization on porous or nanofibrous membranes	(Cui & Jia, 2017; Ge et al., 2012a; Jafari-Nodoushan et al., 2022a; J. Zhu et al., 2018a)

Such modifications facilitate the development of hybrid NFs capable of selectively targeting specific pollutants, thereby improving their overall effectiveness in wastewater treatment (Ge et al., 2012a; Vo et al., 2024).

Despite their advantages, the application of NFs in wastewater treatment presents several challenges. One of the main concerns is their reusability and stability, as repeated use may lead to structural degradation and reduced efficiency. Additionally, the cost of large-scale synthesis and potential environmental toxicity associated with the release of nanomaterials into water bodies are critical factors that need to be addressed (S. Y. Lee et al., 2024a).

Efforts are being made to develop eco-friendly and cost-effective synthesis methods, such as green synthesis approaches that utilize plant extracts to fabricate NFs with minimal environmental impact (Witoon et al., 2018). Furthermore, integrating NFs into membrane systems and composite materials can improve their practical applicability and enhance their durability in water treatment processes (Hang et al., 2024). Further research is required to optimize their synthesis, enhance their stability, and assess their long-term environmental impact. By addressing these challenges, NFs could become a mainstream technology in sustainable water treatment, contributing to global efforts in environmental conservation and resource management (Aydin et al., 2024; Petriev et al., 2021; Shende et al., 2018).

Although several recent reviews have discussed nanoflower-based materials or nanocomposite membranes for water treatment, these studies have generally focused on specific material classes, individual membrane processes, or isolated applications. A comprehensive review that systematically examines the relationships among nanoflower morphology, membrane engineering strategies, transport mechanisms, adsorption behavior, photocatalytic activity, antifouling performance, scalability, and environmental sustainability remains lacking. Furthermore, the

emerging role of artificial intelligence (AI) and machine learning (ML) in accelerating membrane material discovery and optimization has received limited attention in previous reviews. Therefore, this review provides an integrated and critical perspective on the design, fabrication, characterization, performance, challenges, and future development of three-dimensional nanoflower-based membranes, while identifying current research gaps and future directions toward practical and large-scale water.

The literature included in this review was identified through structured searches of Web of Science, Scopus, ScienceDirect, and Google Scholar. The search focused primarily on publications from 2010 to June 2026 using combinations of keywords including nanoflower, hierarchical nanostructure, nanomaterial membrane, adsorption, photocatalysis, antifouling, combined using Boolean operators (AND/OR). Additional relevant studies were identified through citation tracking of key publications. Studies were selected based on their relevance to nanoflower-based membrane engineering, including synthesis, characterization, membrane integration, separation mechanisms, antifouling behavior, and water and wastewater treatment applications. Publications unrelated to membrane applications, editorials, patents, conference abstracts, and studies lacking sufficient technical information were excluded. The literature identification and selection process are summarized in the PRISMA-style schematic shown in Fig. 2.

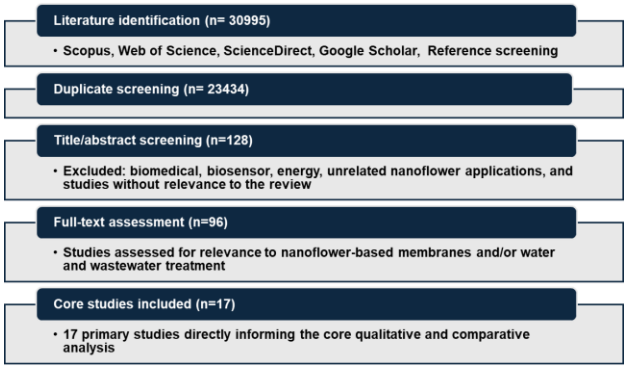

Figure 2. PRISMA-style schematic of the study selection procedure.

Continuous advancements in NF technology have the potential to transform numerous scientific and industrial domains. While NFs show significant promise in water and wastewater purification, further development is required to address existing limitations and ensure their long-term viability in environmental applications. This review provides a critical overview of recent progress and emerging trends in NF-based membranes, covering fundamental concepts and working mechanisms, selection of active materials, structural designs, desirable effects, current challenges, and potential applications in water purification.

1.2 Literature Review

1.2.2. Integration of NFs into Membranes

1.2.2.1 Working Mechanism

Nano-enhanced composite membranes (NECMs) operate through two primary mechanisms: adsorption and separation, as illustrated in Fig.3. The separation mechanism of NECMs is based on the physical structure and permeability of the membrane. Pollutants larger than the membrane's pores are rejected through molecular sieving, while smaller molecules can pass through to deeper layers of the membrane. This approach allows for the effective separation of contaminants during wastewater exudation. The membrane's structural morphology, including its pore size and distribution, plays a significant role in determining separation efficiency. Furthermore, large surface areas and short diffusion pathways contribute to rapid separation and low operational resistance(Shende et al., 2018; Vo et al., 2024; H. Yin et al., 2024).

In adsorption-based removal, NECMs are functionalized with specific chemical groups that interact with and capture target pollutants as water flows through the membrane. This interaction is facilitated by the high surface area and the chemical reactivity of the nanomaterials incorporated

into the membranes. The adsorption mechanism allows pollutants to bind to the active sites on the membrane surface or within its pores. The efficiency of this mechanism depends on the proximity between the pollutants and the adsorptive sites, allowing rapid capture at the submicron scale. This enhances the membrane's capacity to remove contaminants through physical and chemical interactions. The pore-filling mechanism involves embedding active nanomaterials directly into the pores of the polymer membrane. This approach enhances both adsorption and separation by providing additional active sites within the membrane structure. Nanomaterials such as Fe_3O_4 microspheres and $Zr(OH)_x$ nanospheres have been successfully incorporated using this method to improve the removal of heavy metals and organic pollutants.

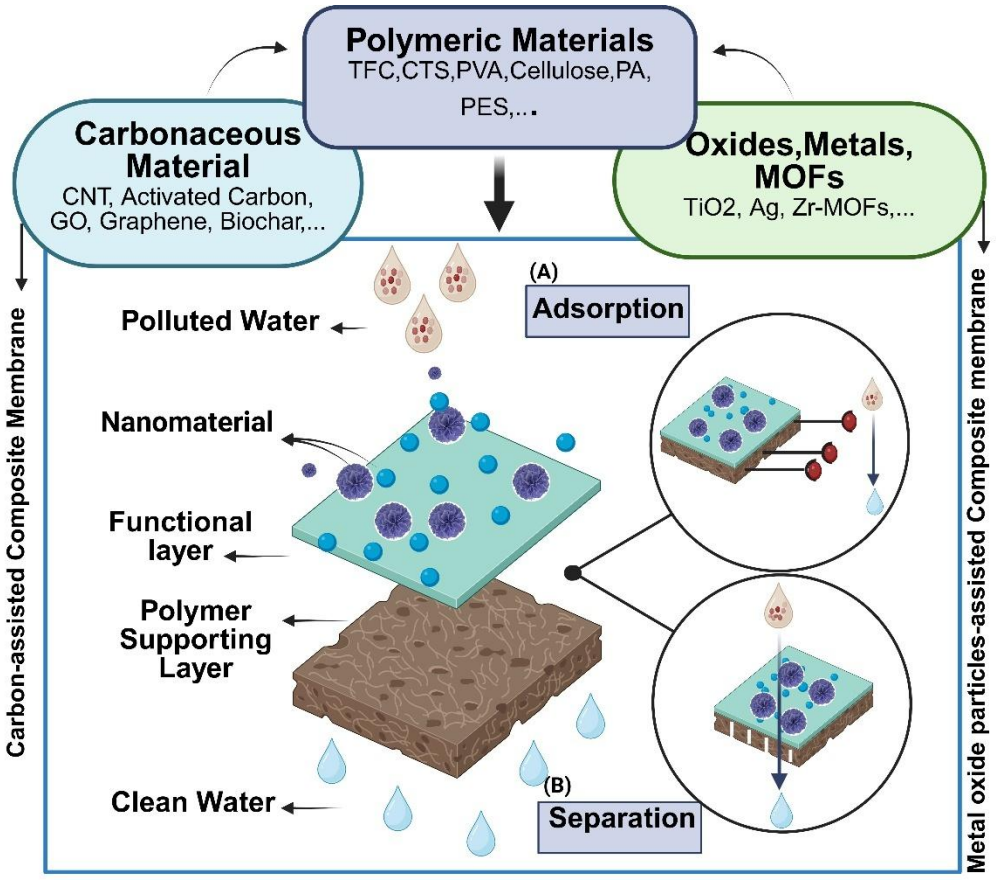

Figure 3- Schematic illustration of NECMs by proposing the incorporation of polymers and Nanomaterials, and the working mechanism of NECMs in water/wastewater purification consisting of (A) adsorption (B) and separation

These two mechanisms, adsorption and separation, work together to enhance the filtration performance of NECMs, making them highly effective for removing a wide range of contaminants from water and wastewater (Vo et al., 2024).

Importantly, the incorporation of NFs significantly enhances all primary mechanisms of pollutant removal: adsorption and separation. Their unique hierarchical, petal-like morphology and abundant exposed reactive sites, create substantially more adsorption sites than spherical or rod-like nanomaterials, enabling stronger chemisorption, ion exchange, and surface complexation with contaminants. For example, MoS_2 NFs integrated onto polymer supports exhibit high edge-plane activity, improved charge separation, and increased pollutant affinity, resulting in enhanced adsorption performance. Similarly, hollow FeCoNi-layered double hydroxide (LDH)-Ag NFs provide layered nanosheets and internal cavities that accelerate mass transfer and strengthen electrostatic adsorption of organic pollutants and pesticides. By exposing more functional planes and binding sites, NFs facilitate rapid contaminant capture at both membrane surfaces and internal pore regions, shifting the system toward chemisorption-dominated uptake and improving overall removal efficiency (Luo et al., 2020; H. Yin et al., 2024).

NFs also influence the separation mechanism by altering membrane surface roughness, hydrophilicity, and polymer cross-linking. When incorporated into thin-film composite (TFC) polyamide (PA) membranes, NFs reshape the ridge-valley topography of the PA selective layer, creating additional nanochannels that facilitate higher water flux while maintaining rejection. This effect is clearly demonstrated in MoS_2/PDI-modified Janus TFC membranes, where NF infusion decreased contact angle, enhanced hydrophilicity, and increased permeability without sacrificing selectivity. Reported membrane flux and permeance span approximately 350 to over 3200 L m^{-2} h^{-1} among representative NF-based membranes

Unlike 1D nanorods or 2D nanosheets, the three-dimensional petal-like architecture of NFs introduces steric hindrance that reduces face-to-face stacking and aggregation within the polymer matrix. This 3D morphology promotes more uniform dispersion and minimizes nanoparticle clustering, which in turn reduces macrovoid formation and improves structural homogeneity during membrane fabrication. Likewise, metal oxide NFs such as ZnO and TiO_2, when embedded within polymer matrices like polysulfone (PSf) or poly vinylidene fluoride (PVDF), reduce foulant adhesion and promote better separation under photocatalytic activation. The hierarchical NF structure contribute to enhanced mechanical stability and more consistent transport pathways during filtration (Sahu et al., 2025; P. Zhao et al., 2023).

In addition, NFs substantially improve the pore-filling mechanism when embedded within membrane pores. Their layered or hollow morphologies generate internal transport tunnels and additional active adsorption zones. This was observed in the FeCoNi-LDH NF system, where the hollow NF structure created interconnected porous channels that facilitated diffusion and increased the availability of adsorption sites within the membrane matrix. By occupying polymer voids with reactive NF structures, the membrane gains both structural reinforcement and enhanced chemical activity, which synergistically improve both adsorption and separation efficiency.

Although the incorporation of NF introduces additional adsorption-active sites, adsorption in NF-based membranes does not operate as an isolated process that inevitably leads to fouling. Instead, adsorption works synergistically with size-based filtration and surface-mediated interactions. The hierarchical NF structure enhances contaminant capture while simultaneously improving membrane hydrophilicity and surface charge, which promotes the formation of a hydration layer and reduces nonspecific foulant adhesion. In addition, many NF-modified membranes exhibit antimicrobial or photocatalytic activity, which suppresses biofilm formation and enables partial

self-cleaning during operation. As a result, adsorption is often localized and reversible rather than causing irreversible pore blockage, allowing NF-based membranes to achieve enhanced removal efficiency without proportionally increasing fouling propensity.

The type of polymer used in the membrane strongly affects how NFs integrate and perform. In TFC PA membranes, the porous support layer (usually polyethersulfone (PES) or PSf) and the ultra-thin PA selective layer formed via interfacial polymerization provide multiple opportunities for NF incorporation. These include before polymerization, within the PA selective layer, or grafted onto the surface. NF deposition onto the support can influence PA growth, leading to denser and more cross-linked selective layers with lower reverse solute flux. Embedding NFs directly into the PA layer creates strong NF-polymer interfacial interactions, enhancing hydrophilicity, catalytic activity, and antifouling properties. This effect has been reported for Au NF that exhibit antimicrobial activity by generating ROS, contributing to reduced biofouling when immobilized on membrane surfaces.

In contrast, polymeric membranes such as PVDF, polyacrylonitrile (PAN), or PSf benefit from NF integration by improving hydrophilicity, enhancing mechanical stability, and creating more efficient water-transport pathways, whereas ceramic membranes gain catalytic synergy and high-temperature/chemical resistance when paired with NFs. Across all membrane types, the integration of NFs consistently enhances rejection performance, increases permeability, and improves antifouling behavior due to their unique structural and chemical features.

It is important to distinguish adsorption from membrane separation and photocatalytic degradation when evaluating membrane performance. Adsorption is governed by the interaction between pollutant molecules and the available active sites on NF surfaces and should therefore be evaluated using adsorption capacity (q, mg g^{-1}), adsorption kinetics, equilibrium isotherms, and mass-

balance analysis rather than rejection efficiency alone. High removal efficiency does not necessarily indicate high adsorption capacity, particularly when pollutant concentrations, adsorbent dosage, or operating conditions differ among studies. Therefore, adsorption performance should be interpreted using standardized adsorption parameters together with mechanistic evidence obtained from kinetic, isotherm, and spectroscopic analyses(Hassan et al., 2024).

Overall, the incorporation of NFs into NECMs improves adsorption, separation, and pore-filling pathways by integrating high surface area, tunable surface chemistry, and hierarchical porosity with polymeric and TFC membrane architectures. Collectively, these enhancements enable NF-based membranes to outperform conventional nanocomposites and represent a promising direction for next-generation high-efficiency water purification systems (L. Di et al., 2024; Rahbari-Sisakht et al., 2025; Sahu et al., 2025; J. Zhang et al., 2024; P. Zhao et al., 2023).

1.2.2.1.1 Water flux, porosity, and pore size (Separation)

The improvement in flux performance is closely related to the physicochemical properties and morphology of the integrated NFs. Their hierarchical and porous architectures provide additional transport pathways for water molecules, facilitating faster permeation across the membrane surface. Furthermore, NFs with high surface area and functional groups can promote interfacial compatibility with the polymer matrix, minimizing macro void formation and contributing to more uniform contributing to a more uniform pore size distribution of the polymer matrix.

Incorporating NFs or other functional nanostructures into the membrane can also lead to the formation of interconnected networks that enhance water transport channels. This interconnected structure not only improves flux but can also contribute to higher contaminant rejection by balancing permeability and selectivity. Representative NF-based membranes have achieved

approximately 95–99.4% contaminant rejection or separation. Overall, NF-modified membranes exhibited improved flux performance due to their high surface porosity, tunable hydrophilicity, and unique three-dimensional morphology, which collectively facilitate efficient water passage through the membrane.

Unlike adsorption, membrane separation is a pressure- or concentration-driven process in which contaminant removal is quantified by permeate flux, solute rejection, and permeate/retentate concentrations. Consequently, membrane performance should be evaluated using water permeance, rejection efficiency, fouling resistance, and long-term operational stability rather than adsorption capacity (Hassan et al., 2024).

To quantitatively relate the above morphological changes to membrane performance, several structural parameters are commonly evaluated in the literature. Membrane porosity, mean pore radius, and permeability are frequently calculated using established transport models and empirical relationships. These equations provide a quantitative framework for relating NF incorporation to measurable changes in pore structure and water transport behavior. By applying them, researchers are able to assess how variations in NF loading, dispersion, and interfacial compatibility influence the effective pore size distribution and overall membrane permeability. Therefore, Equations (1)-(3) are introduced here to illustrate the quantitative methods typically used to correlate membrane morphology with separation performance.

Water flux refers to the volume of water that passes through a membrane per unit area and per unit time, representing the rate of water permeation. In NF-based membrane systems, water flux is commonly evaluated using a crossflow filtration setup and can be calculated using a standard permeation Equation (1). The incorporation of NF structures into the membrane matrix can significantly enhance hydrophilicity amd improve the overall permeability of the system. It may

influence the effective network density by disrupting polymer chain packing or modifying local cross-linking efficiency, potentially increasing free volume within the membrane matrix.

$$J = \frac{V}{A \times t} \qquad (1)$$

where J is the water flux of the membrane, V is the Liquid volume, A is the area of the membrane, and t is the specific time(W. Sun et al., 2026).

Profile solution was used as the wetting liquid. The average porosity (ε) of the membranes was determined using the gravimetric method, as shown in Equation (2):

$$\varepsilon = \frac{M_W - M_D}{A \times \delta \times \rho} \qquad (2)$$

where M_W and M_D (g) are the masses of the wet and dry membranes, A (cm^2) is the effective membrane cross-sectional area perpendicular to the direction of flow, δ (cm) is the membrane thickness, and ρ (1.87 g/cm^3) is the density of the profile solution (W. Sun et al., 2025).

The mean pore size (r_m) of the membranes was calculated using the Guerout–Elford–Ferry equation based on porosity and pure water flux, as given in Equation (3):

$$r_m = \left(\frac{(2.9 - 1.7\varepsilon) \times 8\eta \times \delta \times J}{\varepsilon \times \Delta P}\right)^{0.5} \qquad (3)$$

where η is the viscosity of water (8.9×10^{-4} Pa·s), and ΔP (MPa) is the operating pressure(46.)

1.2.2.1.2. Adsorption kinetics

In most NF-based membranes, the adsorption process is best described by the pseudo-second order (PSO) kinetic model. This is primarily because NFs possess highly reactive surfaces, abundant functional groups, and hierarchical porous structures that promote chemisorption-dominated interactions. The uptake of contaminants on NFs typically involves electron sharing, surface

complexation, ion exchange, or coordination with exposed metal sites. Although a good fit to the PSO model may suggest that chemisorption contributes to adsorption, kinetic fitting alone is still insufficient to conclusively establish the adsorption mechanism. Confirmation requires complementary analyses, including comparison with alternative kinetic models, residual analysis, and independent spectroscopic or mechanistic evidence. Numerous studies on $Cu_3(PO_4)_2$ NFs , ZnO NFs , TiO_2 NFs, and biochar-NF composite membranes consistently show PSO rate constants with correlation coefficients (R^2) exceeding 0.99, confirming that chemical adsorption is the rate-controlling step rather than simple physisorption. Consequently, the PSO kinetic model provides a more accurate representation of pollutant uptake on NF membranes and is widely used to evaluate their adsorption performance. The model can be expressed as:

$$q_t = \frac{q_e^{\,2} \times k_2 \times t}{1 + q_e^{\,2} \times k_2 \times t} \qquad (4)$$

where q_t represents the amount of solute adsorbed on the NF-based membrane at time t, q_e is the equilibrium adsorption capacity, and k_2 is the rate constant of the PSO kinetic model.

Adsorption isotherms are used to explain the interaction between adsorbates and adsorbents and to compare adsorption capacities under equilibrium conditions. The equilibrium adsorption amount can be calculated from the difference between the initial and equilibrium concentrations of the solute as:

$$q_e = \frac{(C_o - C_e) \times V}{m} \qquad (5)$$

where C_0 (mg L^{-1}) is the initial concentration of the adsorbate in solution, C_e (mg L^{-1}) is the equilibrium concentration of the adsorbate in solution, V (L) is the volume of the aqueous solution, and m (g) is the mass of the adsorbent.

Although the PSO kinetic model and the Langmuir isotherm provide accurate descriptions for many NF-based membranes, the validity and parameters of these models are highly sensitive to the physicochemical characteristics of the NFs. Variations in NF composition, such as differences between metal oxides, metal phosphates, and hybrid biochar-NF structures, directly influence the rate constant k_2 in Equation (4) by altering the density of reactive sites, surface charge distribution, and electron-donating or electron-accepting capabilities. For example, NFs with higher metal oxidation states or stronger Lewis's acidity typically exhibit faster chemisorption, producing larger k_2 values and steeper q_t–t curves. Similarly, structural modifications including petal thickness, pore connectivity, and crystallinity can change diffusion pathways and activation energies for surface complexation, thereby affecting both q_e and the overall kinetics.

The Langmuir model frequently provides a satisfactory description of equilibrium adsorption in many NF-based membrane systems. However, a good Langmuir fit should not be interpreted as definitive evidence of homogeneous monolayer adsorption, since multiple adsorption mechanisms may produce similar mathematical behavior. More robust mechanistic interpretation requires comparison with competing isotherm models, statistical evaluation of model fitting, and complementary surface characterization. Studies on $Cu_3(PO_4)_2$ NF, ZnO NFs , TiO_2 NFs , and polymer-NF composite membranes consistently report higher correlation coefficients ($R^2 > 0.98$) for the Langmuir model compared to the Freundlich or Temkin, indicating that adsorption occurs on energetically homogeneous sites. Although Freundlich is occasionally used for heterogeneous systems such as biochar-NF composites, the Langmuir model remains the most accurate for describing equilibrium adsorption on NF surfaces.

The Langmuir isotherm assumes monolayer adsorption on a homogeneous surface and is defined as:

$$q_e = \frac{q_{max} \times k_L \times C_e}{1 + k_L \times C_e} \qquad (6)$$

where k_L and q_{max} represent the Langmuir equilibrium constant and the maximum adsorption capacity.

The Freundlich isotherm, which describes multilayer adsorption on heterogeneous surfaces, can be expressed as:

$$q_e = k_F \times C_e^{1/n} \qquad (7)$$

where k_F and 1/n are the Freundlich constant and the heterogeneity factor of the adsorption process (Kataria & Garg, 2018; M. Song et al., 2025).

The equilibrium parameters in the isotherm equations are equally dependent on NF type. In Equation (6), both q_{max} and k_L reflect the intrinsic uniformity and binding affinity of NF active sites. Metal-phosphate NFs, which possess well-ordered coordination environments, often yield higher q_{max} values due to energetically homogeneous surfaces conducive to monolayer adsorption. In contrast, hybrid systems such as biochar-NF composites introduce heterogeneous surface chemistry, causing deviations toward Freundlich behavior and altering the empirical constants k_F and 1/n in Equation (7). Additionally, the presence of functional groups, defect sites, or dopants in engineered NFs can shift C_e-q_e relationships by modifying electrostatic attraction, π–π interactions, or ion-exchange equilibria.

Other factors, such as pH, ionic strength, competing ions, and the degree of NF agglomeration, also exert substantial influence on the model parameters by changing surface charge states, site accessibility, and diffusional resistance. These multi-level dependencies demonstrate that while PSO and Langmuir models reliably fit NF systems, the underlying constants are not universal and

must be interpreted in the context of NF morphology, composition, and interfacial chemistry. A more mechanistic integration of NF structure-property relationships into these models is essential to advance predictive adsorption modeling for NF-based membranes.

Although the PSO and Langmuir models are frequently reported for NF-based membranes, their widespread application should be interpreted cautiously. Most studies rely solely on high correlation coefficients (R^2) to identify adsorption mechanisms without evaluating alternative kinetic models, residual distributions, or statistical uncertainty. Furthermore, adsorption behavior varies considerably with NF composition, membrane architecture, feed chemistry, and operating conditions, making direct comparison between studies difficult. Future investigations should incorporate nonlinear regression, uncertainty analysis, and spectroscopic characterization to establish more reliable structure-property relationships and clarify the dominant adsorption mechanisms.

1.2.2.1.3 Hydrophilicity or hydrophobicity (contact angle)

Incorporation of NF structures onto membrane surfaces is widely recognized as an effective strategy for tailoring membrane hydrophilicity. The unique hierarchical micro-and-nanostructures of NFs increase the surface roughness and expose a larger number of active sites, which promotes rapid water spreading and results in smaller water contact angles. When combined with hydrophilic functional groups, either intrinsic to the NFs or introduced through additional surface modification, membrane can achieve significantly enhanced wettability. This improvement arises from the synergistic interaction between the three-dimensional NF morphology, which provides abundant pathways for water affinity, and the hydrophilic chemistry, which facilitates the formation of a stable hydration layer. Enhanced hydrophilicity not only accelerates water permeation but also suppresses foulant adhesion, making NF-modified membranes highly advantageous for water

purification and wastewater treatment applications where high flux and antifouling performance are critical (Dai, Ding, et al., 2024).

Although NF incorporation markedly improves membrane hydrophilicity, additional modifications are required to ensure stable and durable wettability under practical operating conditions. Hydration layers generated by NF surfaces may diminish over time due to foulant shielding, polymer chain relaxation, or partial dissolution of metal-based NFs, leading to gradual recovery of hydrophobic characteristics. Therefore, strategies such as covalent tethering of NFs to membrane surfaces, grafting of robust hydrophilic moieties, and construction of multi-layered interfacial architectures are essential for preserving long-term hydrophilicity. Moreover, the hierarchical surface roughness introduced by NFs must be carefully controlled, as excessive surface asperities may promote localized fouling or induce undesirable wetting transitions. Advanced modifications, including zwitterionic functionalization, stable oxide-shell coatings, and hydrophilic polymer brushes, can further enhance interfacial water structuring and suppress foulant adsorption. Overall, effective hydrophilicity optimization in NF-based membranes requires not only introducing highly wettable NFs but also the engineering of chemically stable, strongly anchored, and foulant-resistant interfacial layers capable of maintaining low contact angles during extended membrane operation.

1.2.2.1.4 Surface charge property

Surface charge plays a crucial role in governing the interfacial behavior and separation performance of NF-based membranes. The incorporation of NF structures frequently alters membrane's zeta potential due to the presence of abundant functional groups and the increased surface roughness associated with their hierarchical morphology. When NFs are deposited onto a membrane surface and combined with a hydrophilic modification layer, a substantial change in

surface charge is typically observed. In many systems, the pristine substrates exhibit a relatively negative zeta potential, whereas the introduction of NFs followed by a secondary hydrophilic coating further increases the negative charge, as illustrated in Fig.4. This enhancement is attributed to the exposure of polar groups and the improved NF dispersion across the membrane surface, together producing a more uniformly charged interface. An increased negative surface charge strengthens electrostatic repulsion toward negatively charged pollutants, suppresses fouling, and improves separation efficiency. These findings highlight the importance of surface charge engineering in NF-modified membranes and demonstrate how hierarchical nanostructures combined with hydrophilic layers can synergistically optimize zeta potential for advanced water treatment applications (Dai, Hu, et al., 2024a; J. kun Yin et al., 2025).

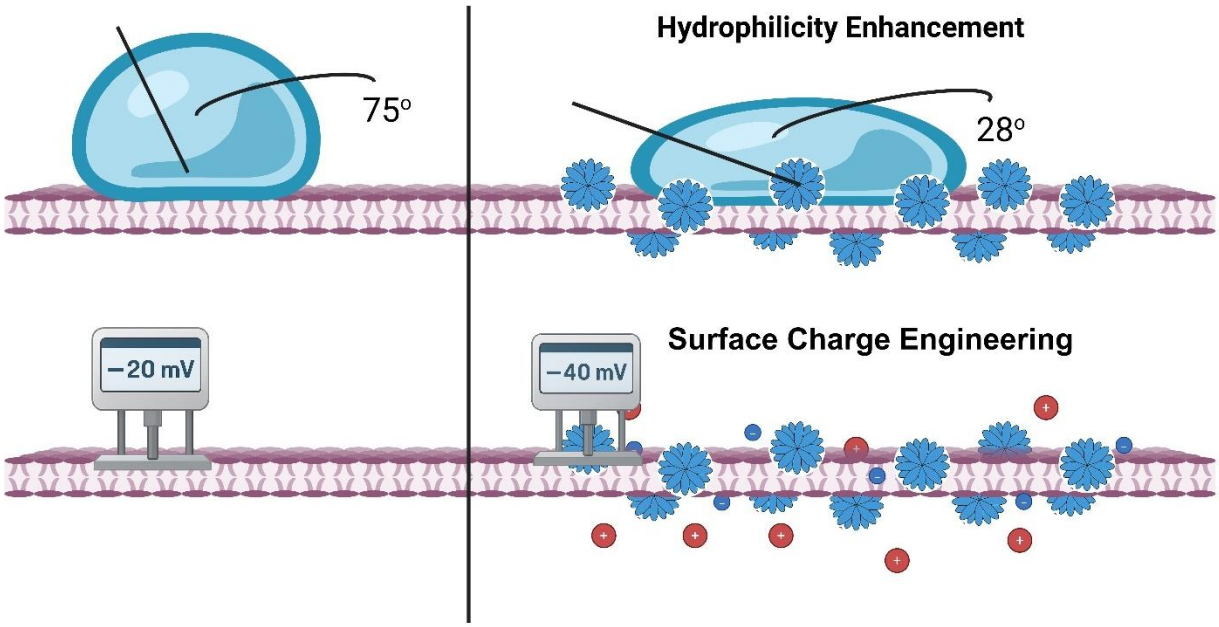

Figure 4- Dual mechanisms of NF-modified membranes: hydrophilicity enhancement and surface charge engineering.

1.2.2.1.5 The energy band gaps of NF

The energy band gap (E_g) of NFs is a critical parameter governing their optical absorption, photocatalytic activity, and electron-hole separation efficiency. Owing to their hierarchical architectures composed of ultrathin nanosheets or nanopetals, NFs exhibit electronic structures that differ significantly from bulk materials. This morphology induces quantum confinement, surface defects, and lattice distortion, which collectively contribute to tunable band-gap behavior and directly impact membrane-related applications such as photocatalysis-assisted filtration, self-cleaning, and pollutant degradation (Jiang et al., 2023; X. Liu et al., 2021; Y. Zhou et al., 2024).

Recent studies demonstrate that band-gap engineering in NFs can be systematically achieved through strategies such as cation doping, facet manipulation, and heterostructure construction. For example, δ-MnO_2 NFs doped with Mg^{2+}, Na^+, and K^+ ions exhibit substantial bandgap narrowing (Mg=MnO_2: 1.08 eV; Na-MnO_2: 0.90 eV; K-MnO_2: 0.76 eV), compared with the reported ~2.3 eV for undoped MnO_2. The increasing ionic radius of the dopants ($Mg^{2+} < Na^+ < K^+$) promotes electron donation into MnO_2 layers and stabilizes interlayer spacing, thereby reducing the excitation energy required for electron transition from the valence to conduction band. This tunability enhances visible and near-infrared light absorption, enabling effective activation under low-energy irradiation. Consequently, such band-gap manipulation significantly increases photothermal and photocatalytic efficiencies, as demonstrated in the doped MnO_2 NF systems(X. Liu et al., 2021).

Band-gap tuning has also been demonstrated in $Sn_{1-}Ce_xO_2$ NFs, where Ce doping introduces oxygen vacancies and modifies surface electronic states. These structural modifications reduce the band gap and enhance surface-enhanced Raman scattering (SERS) activity by enabling stronger charge-transfer interactions between analytes and the semiconductor surface. In addition, the hierarchical NF morphology exposes a high density of active sites, where Ce-induced defect states

facilitate more efficient electron-photon coupling, thereby amplifying optical responses(Jiang et al., 2023).

Similarly, BiOBr NFs with tunable (001) facets display band gaps ranging from 2.51 to 2.70 eV, depending on the dominant exposed facet. By adjusting synthesis parameters, preferential growth of nanosheets with high-energy surfaces can be achieved, thereby modulating the electronic band structure. BiOBr NFs with a larger proportion of exposed (001) facet exhibit narrower band gaps and enhanced photocatalytic degradation of organic dyes. Their hierarchical, flake-like petals promote rapid charge carrier separation and suppress recombination, which are critical for oxidative degradation reactions (Y. Zhou et al., 2024). Moreover, the combined influence of ultrathin nanosheet curvature, vacancy-induced mid-gap states, and inter-petal electronic coupling in NFs significantly narrows the bandgap, as illustrated in Fig. 5, enabling more efficient electron excitation and enhanced photocatalytic performance.

Photocatalytic degradation differs fundamentally from both adsorption and membrane rejection because contaminants are chemically transformed rather than merely retained or accumulated. Accordingly, photocatalytic performance should ideally be evaluated using mineralization efficiency (e.g., TOC removal), catalyst stability, reactive oxygen species generation, and identification of transformation products, in addition to apparent degradation efficiency (Hassan et al., 2024).

Overall, these findings demonstrate that the band gap of NFs is not fixed but highly tunable, enabling the rational design of NF-based membranes with targeted optical and catalytic properties. In water treatment applications, narrower band gaps enable activation under solar or visible light, improve reactive oxygen species (ROS) generation, support self-cleaning membrane functions, and enable integration with advanced oxidation processes (AOPs). Thus, band-gap engineering

represents a powerful strategy for optimizing NFs to achieve enhanced pollutant removal, antifouling performance, and energy-efficient water purification. Narrowing the band gap is commonly considered an effective strategy for enhancing photocatalytic performance as band-gap energy alone does not determine catalytic efficiency. Charge-carrier separation, reactive oxygen species generation, catalyst recovery, and long-term photostability often exert equally important influences on membrane performance. Future studies should therefore evaluate photocatalytic activity using comprehensive metrics, including mineralization efficiency, catalyst durability, and quantum efficiency, rather than relying primarily on band-gap values.

While band-gap engineering remains an important strategy for improving visible-light absorption, photocatalytic performance is typically governed by multiple interrelated factors beyond the band-gap value alone. The relative positions of the conduction and valence bands determine the redox potential available for the generation of reactive oxygen species (ROS), including hydroxyl radicals (•OH), superoxide radicals ($\bullet O_2^-$), and singlet oxygen, which are responsible for pollutant oxidation and degradation. In addition, efficient separation of photogenerated electron–hole pairs and suppression of charge-carrier recombination are essential for maximizing photocatalytic activity. Operational parameters, such as light intensity, irradiation wavelength, catalyst loading, and solution chemistry, also significantly influence degradation efficiency. Moreover, photocatalytic performance should ideally be evaluated not only by pollutant removal efficiency but also by mineralization indicators such as total organic carbon (TOC) removal and the identification of intermediate transformation products to ensure complete degradation and minimize the formation of potentially harmful by-products. Catalyst stability and recovery are equally important considerations for practical implementation, particularly for reusable membrane-based photocatalysts. Recent studies, such as that reported by Hassan et al. (2025), have

demonstrated that integrating adsorption, photocatalysis, and magnetic recovery within multifunctional nanocomposites can simultaneously enhance contaminant removal, facilitate catalyst recycling, and improve long-term operational sustainability, highlighting a promising direction for next-generation nanoflower-based membrane systems(52).

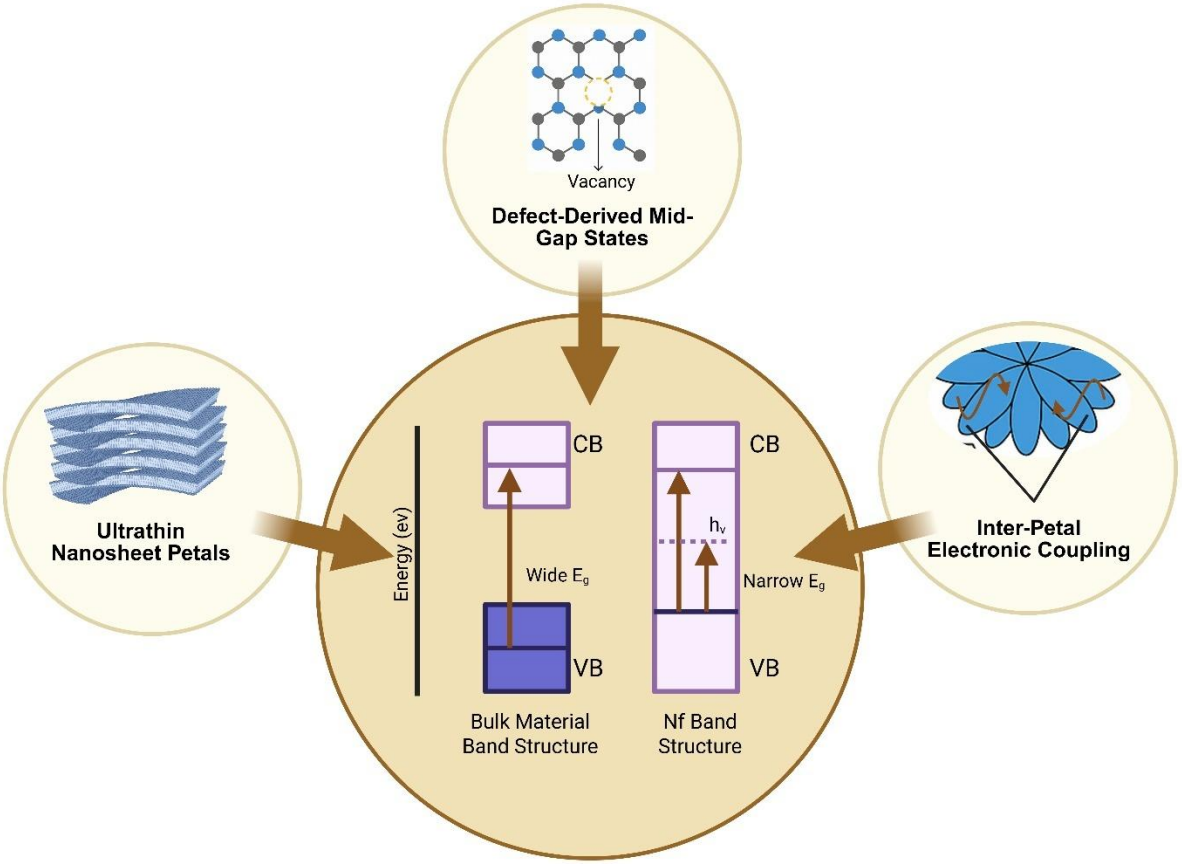

Figure 5- Key mechanisms-nanosheet petals, defects, and electronic coupling-that narrow the band gap in NFs.

1.2.2.2. Technical challenges in fabricating commercial membranes for specific uses: Conventional modalities and NF-based membranes

Membrane technology has become a cornerstone of modern separation processes, including desalination, wastewater treatment, and industrial separations. Despite its widespread adoption, the fabrication of commercial membranes for specific uses remains challenging. Key challenges

arise from material selection, membrane fouling, structural stability, energy efficiency, and scalability. Addressing these challenges is crucial for developing cost-effective, durable, and high-performance membranes capable of meeting industry demands.

One of the primary challenges in membrane fabrication lies in the selection of materials that deliver optimal performance for specific applications. Polymeric membranes, such as PA, PSf, and PES, are widely used due to their cost-effectiveness and ease of fabrication. However, these materials often exhibit inherent trade-offs between permeability and selectivity, which can limit their overall separation efficiency (Imteyaz et al., 2025; M. Liu et al., 2025; Y. Liu et al., 2025).

To enhance membrane performance, nanomaterials (NMs) have been integrated into polymeric membranes. Carbon nanotubes (CNTs), titania nanotubes (TNTs), and metal oxides like ZnO and TiO_2 have shown potential in improving membrane characteristics. Despite these benefits, nanomaterial incorporation introduces challenges related to uniform dispersion, potential leaching, and long-term stability. Ensuring robust compatibility between nanomaterials and polymeric matrices therefore remains a major obstacle to the large-scale commercialization of polymer nanocomposite membranes (Dai, Hu, et al., 2024a; J. Di et al., 2024; Jafari-Nodoushan et al., 2022a).

Fouling is one of the most critical challenges affecting membrane performance and operational longevity. It occurs due to the accumulation of organic matter, inorganic scaling, biofouling, and particulate deposition on the membrane surface. Because these fouling mechanisms differ in origin and behavior, they require distinct and targeted mitigation strategies:

1. Organic Fouling: Caused by natural organic matter, proteins, and oils. Hydrophilic membrane surfaces and antifouling coatings can reduce organic fouling (García-Ávila et al., 2024; Qi et al., 2025; K. Wang et al., 2023).
2. Inorganic Scaling: Results from the precipitation of salts like calcium carbonate and magnesium hydroxide. Anti-scaling agents and pH control can help minimize scaling (García-Ávila et al., 2024; J. Sun et al., 2025).
3. Biofouling: Arises from the growth of microorganisms and biofilm formation. Silver nanoparticles and antibacterial coatings have shown effectiveness in suppressing biofouling (Y. Li et al., 2025; C. Song et al., 2025).
4. Particulate Fouling: Occurs due to the deposition of suspended solids, which can clog membrane pores. Proper pre-treatment, including filtration and coagulation, is essential to reduce particulate fouling (Gao et al., 2025; M. Liu et al., 2025; K. Wang et al., 2023).

Despite advancements in antifouling strategies, completely preventing fouling remains challenging. Therefore, membranes require frequent cleaning and periodic replacement, leading to increased operational costs. Commercial membranes must also withstand high operating pressures and harsh chemical environments. Mechanical deformation and chemical degradation are common issues that limit membrane lifespan. For instance, reverse osmosis (RO) membranes operate under high pressures, which can induce material fatigue and structural failure over time (Y. Y. Lee et al., 2024).

Enhancing membrane mechanical strength involves optimization of support layers and the selection of robust materials. Thin-film composite (TFC) membranes with improved interfacial adhesion and reinforced support structures offer enhanced mechanical durability. However,

balancing mechanical strength and permeability is challenging, as increased membrane density often leads to have reduced water flux.

Energy consumption is another critical concern in pressure-driven membrane processes, such as RO and nanofiltration. The energy required to overcome osmotic pressure and hydraulic resistance contributes significantly to overall operational costs. While highly permeable membranes with lower resistance can reduce energy consumption, increasing permeability often compromises selectivity (Kong et al., 2024; Samavati et al., 2025).

Recent research has focused on designing membranes with high permeability while maintaining adequate salt rejection. Techniques such as modified interfacial polymerization and the incorporation of nanomaterials (e.g., NFs, nanoparticles, and other nanostructured fillers) into membrane matrices have shown considerable promise.

In addition, nanoscale engineering of the selective layer-through controlled pore formation and structural tuning-has been explored to enhance transport efficiency without compromising selectivity. However, translating these innovations to commercial-scale membrane fabrication has advanced significantly, scaling production to industrial levels presents substantial technical and economic challenges. (67) Key challenges in large-scale membrane production include ensuring batch-to-batch consistency, ensure uniform membrane thickness and defect-free structures, developing scalable coating and deposition techniques, reducing production costs while maintaining quality, and addressing environmental concerns related to membrane disposal and recycling (X. Li et al., 2023; Tao et al., 2018; Vo et al., 2024; J. Wei et al., 2022).

Membrane technology has advanced substantially in water treatment and separation processes, utilizing microfiltration (MF), ultrafiltration (UF), and nanofiltration. Despite these advances,

fabricating membranes that balance permeability, selectivity, and antifouling performance remains a significant challenge. Conventional polymeric membranes often suffer from fouling, degradation under harsh operating conditions, and limited selectivity (J. Di et al., 2024). Integrating NF structures into membranes offers a promising strategy to address these limitations by improving surface properties and enhancing adsorption capacity (Khraisheh et al., 2021).

The fabrication of commercial membranes for filtration applications involves several technical challenges, including achieving optimal porosity, stability, and resistance to fouling. Conventional membranes frequently encounter pore clogging, limited mechanical strength, and chemical degradation under harsh operating conditions. Recent advances in NF-based membranes offer promising solutions to address these limitations by leveraging unique hierarchical architectures that enhance filtration efficiency and durability. Incorporation of NFs into various membrane technologies, including PA and ceramic composites, has been widely explored to enhance their antifouling properties and permeability (S. Y. Lee et al., 2024a; Z. Li et al., 2020).

NFs exhibit a large surface area and superior structural stability, making them promising candidates to improve the selectivity and retention performance of micro-, ultra-, and nanofiltration membranes. Their roles in hybrid membrane systems have been demonstrated in several studies, highlighting their catalytic, adsorptive, and antimicrobial functions in water purification (Aydin et al., 2024). Furthermore, the hierarchical morphology of NFs enables enhanced molecular sieving, allowing more effective separation of contaminants from water (Qi et al., 2025).

Membrane fouling remains a significant challenge in filtration processes, leading to reduced efficiency and higher maintenance costs. Incorporation of NFs has been shown to mitigate fouling

by introducing self-cleaning and antimicrobial properties, thereby extending membrane lifespan and sustaining performance. Moreover, NF-based membranes have demonstrated enhanced water flux and selectivity, which are essential for improving filtration effectiveness across diverse applications (J. Wei et al., 2022). A comparison of key performance parameters between conventional membranes and NF-based membranes is presented in Table 1.

Table 2. Comparison of key parameters between conventional membranes and NF-based membranes

Parameter	NF-Based Membranes	Conventional Membranes
Adsorption Efficiency	High (due to larger surface area and porosity)	Moderate (limited by surface structure)
Fouling Resistance	Improved (with antifouling agents like Ag, TiO_2)	Prone to fouling (requires frequent cleaning)
Mechanical Strength	Moderate (enhanced with hybrid supports)	High (established materials are more robust)
Fabrication Complexity	High (requires precise synthesis and hybridization)	Low (simpler and well-established processes)
Scalability	Challenging (requires advanced synthesis methods)	Easier (standardized mass production)
Cost of Production	High (complex synthesis and hybrid integration)	Lower (simpler and cost-effective)
Environmental Impact	Potential nanoparticle leaching (needs regulation)	Minimal (fewer safety concerns)
Application Versatility	Wide (customizable for specific pollutants)	Limited (fixed design and function)
Stability in Harsh Conditions	Moderate (requires reinforcement)	High (better tolerance to pressure and pH)

Incorporation of NFs into membrane structures has led to significant improvements in permeability, selectivity, and antifouling performance. However, several unresolved scientific and engineering challenges continue to limit their commercial adoption. A major limitation arises from the discrepancy between laboratory-scale evaluations and the complex physicochemical conditions encountered in real feedwaters. Laboratory studies often rely on single solutes or

simplified matrices, whereas full-scale systems are exposed to fluctuating ionic strength, competing anions, natural organic matter, colloids, surfactants, and diverse microbial communities. These constituents can alter electrostatic interactions, destabilize NF-polymer interfaces, and accelerate degradation mechanisms that are typically not captured in short-term controlled studies.

The hierarchical architecture of NFs provides high surface reactivity but also introduces structural vulnerability during long-term filtration. Crossflow shear, pressure fluctuations, and repeated cleaning cycles may deform the petal-like motifs, promote delamination, or induce dissolution. However, mechanistic investigations of these degradation pathways remain limited, and the potential release of NF fragments into permeate streams raises concerns regarding both performance reliability and environmental safety. The absence of standardized protocols to quantify NF leaching under realistic operating conditions therefore represents a critical barrier to regulatory approval and large-scale deployment.

Scalability constitutes another major challenge. Most NF synthesis routes, including hydrothermal mineralization, biomolecule-assisted nucleation, template-guided growth, and multi-step hybridization, are batch-dependent and poorly suited to continuous industrial membrane fabrication. Moreover, NF morphology is highly sensitive to precursor concentration, nucleation rate, solution chemistry, and growth kinetics, all of which are difficult to maintain uniformly across large membrane areas. These sensitivities can lead to variability in pore distribution, surface functionality, and defect density, ultimately undermining the consistency required for commercial membrane modules.

From a materials engineering perspective, interfacial compatibility between NFs and polymer matrices remains insufficiently understood. Adhesion is driven by hydrogen bonding, van der

Waals interactions, or covalent bridges; however, stress transfer mechanisms within hybrid layers have not been fully characterized. In the absence of robust interfacial anchoring, NF-modified surfaces may undergo functional deterioration during prolonged operation or aggressive cleaning cycles involving alkaline or acidic environments. Furthermore, the improvement in hydrophilicity and surface charge imparted by NFs may diminish over time due to foulant shielding, surface rearrangement, or pore compaction, potentially compromising long-term membrane performance. These evolving interfacial dynamics highlight the need for in situ monitoring tools capable of capturing real-time NF performance during filtration.

Economic and environmental considerations further complicate commercial translation. NF synthesis often relies on high-purity reagents, precise reaction control, and multistep processing, which increase cost and energy demand. In addition, the environmental fate of released NF fragments remains poorly understood. Limited data exists regarding their dissolution behavior, bioaccumulation in aquatic systems, ecotoxicity, and end-of-life disposal, creating significant uncertainty surrounding the overall sustainability of NF-based membrane technologies.

In summary, while NF-enhanced membranes exhibit strong potential at the laboratory scale, their industrial viability requires coordinated advances across multiple fronts. These include developing a mechanistic understanding of NF degradation and leaching, improving interfacial stability under realistic hydraulic and chemical stresses, establishing scalable synthesis routes compatible with industrial membrane manufacturing, and conducting comprehensive environmental and economic assessments. Addressing these fundamental challenges is essential to enable the successful transition of NF-based membranes from laboratory research to reliable full-scale water treatment technologies.

Nanoflower-based materials have demonstrated promising performance in water treatment, with reported separation and degradation efficiencies ranging from approximately 88% to 99.4% in representative studies. Meanwhile, their potential environmental release and long-term stability should also be considered. Dissolved metal release should be distinguished from particulate detachment, as these represent different release pathways and require different analytical approaches. Dissolved metal ions released from copper-containing nanoflowers can be quantified using inductively coupled plasma techniques, such as ICP-OES or ICP-MS, while particulate release can be evaluated using complementary nanoparticle characterization approaches, including particle-size, morphology, and elemental analyses. A mass-balance assessment can further determine the distribution of metals between the treated water, retained material, and released particulate fraction. These assessments are important for determining the environmental stability and practical applicability of nanoflower-based materials (Lead et al., 2018).

Current research has predominantly focused on improving membrane performance under controlled laboratory conditions. However, relatively few studies systematically investigate long-term operation under realistic wastewater matrices containing natural organic matter, competing ions, microorganisms, and fluctuating hydraulic conditions. Bridging this gap represents one of the most important challenges for translating NF-based membranes from laboratory research to practical water treatment applications.

1.2.2.3. Selection of Membrane Materials (Organic or Ceramic) for NF Integration

The selection of membrane materials plays a crucial role in determining the efficiency, durability, and applicability of NF-based membranes. Both organic and ceramic materials offer distinct

advantages, and their selection depends on the targeted operating conditions and separation requirements. Organic polymer membranes, including PA and PAN, are widely used due to their flexibility, ease of fabrication, and cost-effectiveness. However, these materials often suffer from lower mechanical strength and susceptibility to chemical degradation under harsh operating environments (Kim & Rhee, 2023; W. Zhang et al., 2024).

In general, membranes used for water and wastewater purification are divided into three typical types, namely, inorganic membranes, polymeric membranes, and composite membranes (Fig. 6). Inorganic membranes, particularly ceramic membranes, provide superior thermal, chemical, and mechanical stability, making them ideal for aggressive filtration environments. The integration of NFs into ceramic matrices has been shown to improve permeability, fouling resistance, and contaminant removal efficiency. Recent research has highlighted the use of NF-enhanced ceramic membranes in wastewater treatment and pharmaceutical filtration, where they outperform conventional membranes. Ceramic substrates present challenges related to uniform NF anchoring due to their rigid microstructure. NF adhesion on ceramic surfaces depends strongly on interfacial chemistry, including metal-oxygen coordination, surface hydroxylation, and charge matching. Insufficient interfacial binding energy can result in NF detachment or fragmentation during backwashing, high-shear crossflow, or aggressive cleaning cycles, raising concerns related to performance degradation and nanoparticle release. However, systematic studies quantifying adhesion strength, interfacial degradation mechanisms, or ceramic-NF compatibility remain scarce (D. N. Lee et al., 2023; Vo et al., 2024).

Polymeric membranes, such as those based on PA and PAN, offer structural tunability and ease of functionalization, which facilitate NF incorporation. Nevertheless, their viscoelastic nature may lead to surface rearrangement, pore collapse, or gradual degradation of NF–polymer interfaces

under hydraulic pressure, temperature fluctuations, or long-term chemical exposure. These dynamic structural changes can progressively shield or deactivate NF active sites, diminishing hydrophilicity, surface charge density, and catalytic functionality over time.

Composite membranes, including inorganic-organic hybrid systems, represent another promising platform for NF integration, combining the structural robustness of inorganic materials and the functional tunability of polymers. These hybrid systems enable precise control over surface chemistry, pore architecture, and interfacial properties, resulting in highly efficient filtration systems (Luo et al., 2020). Synergistic interactions between NFs and hybrid substrates have been further explored in applications such as oil-water separation and biocatalysis (Ye et al., 2024). Moreover, innovative strategies, including NF-modified carbon nanotubes, have expanded the applicability of hybrid membranes, enhancing their catalytic performance and selectivity for complex water treatment challenges (Deng et al., 2025).

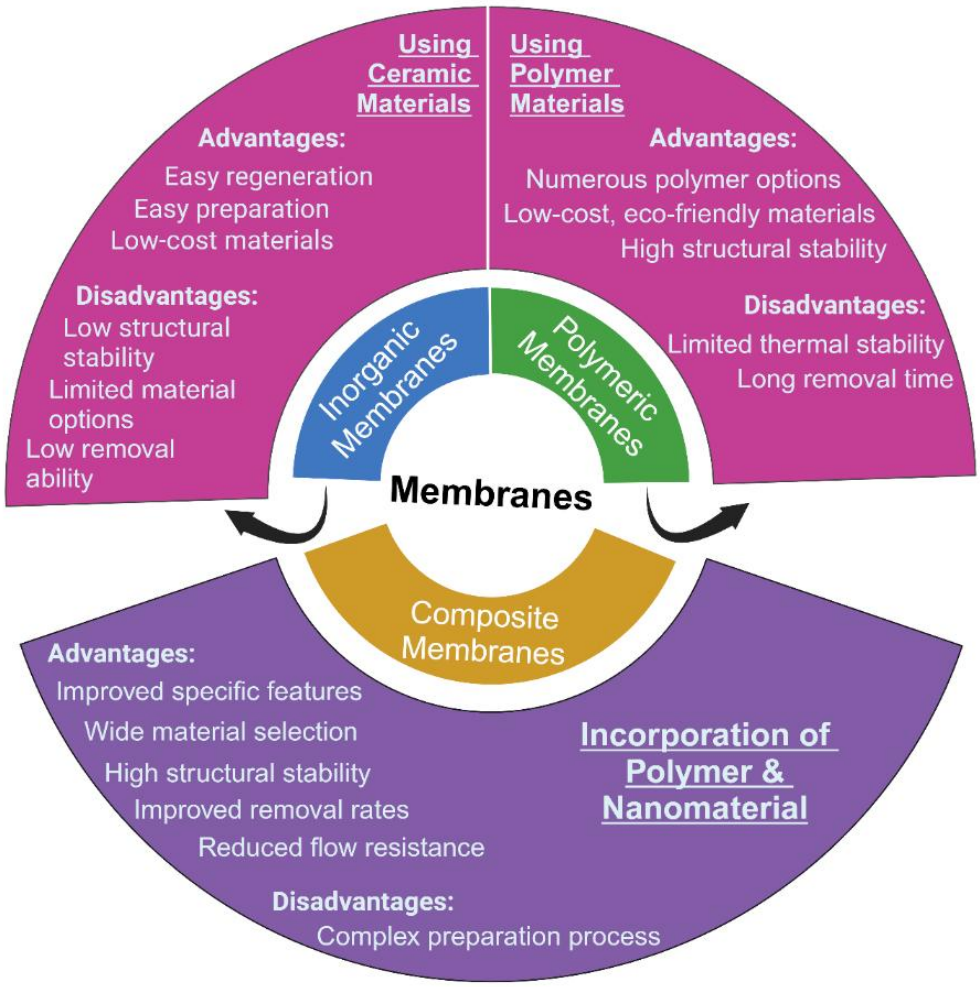

Figure 6- Typical membranes utilized for water/wastewater purification

Despite these advances, several critical scientific and engineering gaps remain in the optimization of membrane materials for NF integration. A major challenge lies in the intrinsic mismatch between the hierarchical, metastable morphology of NFs and the physicochemical behavior of the membrane substrates that support them. Composite substrates introduce additional complexity. Achieving synergistic performance requires precise control over interfacial morphology, pore connectivity, and chemical gradients across hybrid layers. Most existing studies rely on laboratory-scale fabrication methods that fail to capture defect formation, phase segregation, and thermal mismatch stresses that are likely to occur during large-scale production. Furthermore, interaction

between NF functionality and hybrid matrix dynamics under real wastewater compositions, including competing ions, natural organic matter, multivalent cations, surfactants, and biofilm precursors, remains insufficiently understood. Material selection strategies rarely integrate life cycle, environmental, or regulatory considerations. For example, the long-term leaching behavior of metal-phosphate or metal-oxide NFs, their transformation into secondary nano- or ionic species, and their interactions with aquatic biota are not yet comprehensively evaluated. Similarly, the environmental footprint associated with ceramic sintering, high-purity precursors, and solvent-intensive hybrid fabrication processes is often overlooked.

Overall, while polymeric, inorganic, and composite substrates each provide distinct advantages, the scientific basis for selecting optimal membrane material for specific NF architectures remains incomplete. Future progress will require multiscale investigations that integrate interfacial chemistry, mechanical stability, fouling dynamics, and environmental safety under realistic operating conditions and scalable manufacturing processes. Only through this deeper mechanistic understanding can NF-based membranes transition from promising research materials to robust, commercially deployable water purification technologies. No single membrane material can currently satisfy all practical requirements for water purification. Polymeric membranes generally offer superior processability and lower fabrication costs, whereas ceramic membranes provide greater chemical and mechanical stability. Hybrid membrane systems appear to offer the greatest potential by combining the advantages of both materials; however, further optimization of NF-polymer interfacial compatibility and large-scale manufacturing remains necessary before widespread commercialization can be achieved.

1.2.2.4. Local Membrane Properties: How NF-Based Membranes Work

NF-based membranes operate by integrating functional nanomaterials that modify the local physicochemical properties of filtration surfaces. Through tailored control of hydrophilicity, mechanical strength, and reactive surface interactions, these membranes achieve enhanced filtration performance. Several studies have shown that NFs incorporation increases water flux, reduces biofouling, and improves contaminant rejection rates across diverse membrane platforms (Chen et al., 2025).

A defining advantage of NF-based membranes is their ability to facilitate selective adsorption and catalytic degradation of pollutants. Metal oxide NFs, such as ZnO and CeO_2, introduce antimicrobial and photocatalytic functionalities that significantly improve water treatment efficiency (H. Xu et al., 2023). Their high surface reactivity and tunable pore structures further facilitate the removal of pharmaceuticals, heavy metals, and other emerging contaminants (S. Li et al., 2023).

NFs also contribute to enhanced antifouling properties by creating self-cleaning surfaces that inhibit organic and microbial buildup. This functionality is particularly valuable in long-term filtration applications, where membrane longevity and operational stability are critical (J. Wei et al., 2022). By leveraging these properties, NF-based membranes have demonstrated potential in advanced filtration systems, particularly for desalination and wastewater treatment (Dai, Hu, et al., 2024a).

Beyond surface effects, NF-membrane interactions can improve mechanical robustness and stability under high-pressure operation. This has been particularly significant in industrial

wastewater treatment and pharmaceutical purification, where membranes must withstand sustained hydraulic stress (Luo et al., 2020).

Recent studies further reveal that NF incorporation can fundamentally alter the electronic and charge-transfer environment at the membrane surface, resulting in accelerated reaction kinetics and improved pollutant capture. Heterostructure NFs, such as carbon quantum dot–decorated ZnO NFs grown directly on nanofibrous membranes, create highly active photocatalytic interfaces that enhance light absorption, promote charge separation, and enable rapid degradation of organic contaminants under visible-light irradiation. For example, photocatalytic degradation reported at approximately 88–92% for the CQD–ZnO NF membrane. The hierarchical petals increase catalytic site density while facilitating directional electron transport, thereby strengthening oxidative reactions and enabling self-regeneration of the membrane surface during operation (H. Xu et al., 2023).

Similarly, NF–substrate heterojunctions such as $CoNiSe_2$ NFs anchored on layered supports exhibit built-in electric fields (BIEF) arising from interfacial work function differences. These internal fields promote electron redistribution and optimize the adsorption-desorption energetics and enhance selective pollutant capture and catalytic transformation. The radially aligned nanosheets form interconnected mesoporous channels that improve mass transfer, lower flow resistance, and support higher permeability without compromising rejection performance (Wen et al., 2025).

Other NF systems, such as Mo-modified NiFe LDH NFs, demonstrate how top-down etching and interlayer modification generate high-valence metal sites, oxygen-rich surface, and abundant defect-rich regions. When integrated into membranes, these features strengthen adsorptive interactions with charged and polar contaminants, improve wettability, and provide stronger

chemical anchoring to the membrane matrix. Such NFs also exhibit superior mechanical resilience and structural integrity under cyclic hydraulic stresses encountered in industrial processes (Guo et al., 2025).

Moreover, NF architectures grown directly on electrospun or porous substrates, such as LDH-wrapped fibers, ZnO NF/SiC composites, and hybrid $Cu_3(PO_4)_2$-based NFs, exhibit exceptional structural stability and resistance to particle leaching. Their anchored hierarchical growth distributes mechanical loads, preserves pore integrity, and introduces organized nanochannels that support rapid water transport and selective sieving. These properties further elevate the contaminant removal efficiency of the composite membrane.

Collectively, these findings demonstrate that NFs do more than simply increase surface roughness or introduce reactive sites. Instead, they engineer the local membrane microenvironment, enabling synergistic improvements in wettability, charge transport, catalytic activity, pore architecture, and mechanical endurance. This multifunctional impact underscores the growing recognition of NF-enabled membranes as next-generation filtration platforms capable of addressing emerging contaminants while maintaining high-flux and long-term stability under demanding wastewater treatment conditions.

1.2.3. Recent Developments in NF-Based Membranes for Water and Wastewater Treatments

1.2.3.1. Recent studies

NFs have recently emerged as a highly promising nanostructured material for enhancing membrane performance in water treatment. These hierarchical, flower-like nanostructures exhibit high surface area, superior adsorption capacities, and improved catalytic functionalities. Their

integration into membranes has primarily targeted improvements in hydrophilicity, antifouling performance, and mechanical stability. NFs synthesized from metal oxides, carbon-based materials, and hybrid composites have been successfully incorporated into both polymeric and ceramic membranes, demonstrating improved permeability and selective pollutant removal efficiency. For instance, titanium dioxide (TiO_2) NFs integrated into PVDF membranes enhanced photocatalytic degradation of organic contaminants while maintaining high flux stability. Similarly, zinc oxide (ZnO) NFs embedded in PSf membranes improved hydrophilicity and reduced biofouling tendencies, extending operational lifespan. These studies collectively highlight the potential of NFs to advance next-generation membrane systems for sustainable water treatment (Pervez et al., 2020).

Composite materials consist of two or more active components with distinct physical and chemical properties have further expanded NF applications. Nano-enhanced composite membranes (NECMs) integrate nanoscale fillers with polymeric barrier layers, providing tailored performance for water and wastewater treatment. Typically, these membranes feature a polymer support layer at the base and a functional NF-enriched upper layer(J. Di et al., 2024; Kanth et al., 2025; Vo et al., 2024).

1.2.3.2. Application-Based Case Studies at Lab Scale

Laboratory-scale studies have demonstrated the versatility and efficacy of NF-enhanced membranes in treating various types of wastewater streams. Copper oxide (CuO) NF-coated membranes showed significant improvement in heavy metal ion removal due to their high adsorption affinity and electrostatic interactions (Izadi et al., 2019). Cobalt-based NFs incorporated into membrane bioreactors (MBRs) enhanced microbial attachment, aiding biofouling control and stabilizing permeate quality (Bjorge et al., 2009; Pervez et al., 2020).

Graphene oxide (GO) NFs integrated into ultrafiltration membranes reduced irreversible fouling by 50% and enhanced water permeability compared to conventional polymeric membranes (Pervez et al., 2020). Silver (Ag) NF-embedded membranes exhibited strong antibacterial properties, reducing biofilm formation and extending membrane operational life (Raj et al., 2022). These laboratory-scale experiments underscore the versatility and potential of NFs in membrane applications. The findings support further development toward pilot-scale evaluations for real-world implementations.

Additional studies underscore the broad functional versatility of NFs across diverse materials. Metal-organic framework (MOF)-derived NFs were incorporated into PA and PVDF substrates to improve hydrophilicity and surface charge density, improving water permeation and reducing organic fouling in the filtration of dye-rich effluents. Covalent organic framework (COF) NFs created super-hydrophilic separation layers for efficiently treating oil-water emulsions, with hierarchical petals promoting rapid water wetting and minimizing oil adhesion. Carbon-based NFs enhanced adsorption-driven removal of pharmaceutical residues, benefiting from their large external surface area and rapid contaminant diffusion pathways. Metal phosphate and metal oxide NFs further improved removal of charged pollutants, such as heavy metals and oxyanions, through combined electrostatic and surface complexation mechanisms. Collectively, these studies demonstrate that NFs, whether carbonaceous, inorganic, or hybrid, provide tunable surface chemistry, hierarchical porosity, and catalytic or adsorptive functionality that significantly elevate membrane performance across a wide spectrum of wastewater types. (Dai, Hu, et al., 2024a; Guo et al., 2025; Mohamad Esham et al., 2025; Wen et al., 2025; J. kun Yin et al., 2025)

A recent investigation on Black@ZnO-Gr–modified carbon fiber membranes highlighted the benefits of hierarchical ZnO NF structures in degreasing wastewater treatment. The ZnO-graphene

coating enhanced hydrophilicity, adsorption capacity, and photocatalytic self-cleaning, enabling efficient oil and organic pollutant removal while maintaining strong antifouling stability (W. Sun et al., 2026). Figures 7 through 8 and Table 3 summarize representative NF synthesis pathways and membrane architectures developed in recent studies, illustrating the diversity of fabrication methods and structural configurations.

Table 3. comparative summary of representative nanoflower-based membrane systems for water and wastewater treatment.

Ref.	Nanoflower / Loading	Membrane Type	Feed Composition	Filtration Mode	Rejection / Separation
(J. Wei et al., 2022)	ZnO nanoflower; loading NR	SiC ceramic	Water-in-oil emulsion	Pressure-driven filtration	~98.9–99.2% water rejection
(S. Li et al., 2023)	ZnCo-LDH nanoflower; loading NR	PAN nanofibrous membrane	Oil-in-water emulsion	Crossflow filtration	>99%; up to 99.4%
(Luo et al., 2020)	Inorganic–organic hybrid nanoflowers; enzyme-loaded	3D porous nanofibrous membrane	Organic dye solutions	Membrane-supported catalytic treatment	High dye degradation
(H. Xu et al., 2023)	CQD-decorated ZnO heterostructure nanoflowers; loading NR	PAN nanofiber membrane	Methylene blue solution	Photocatalytic membrane treatment	92.08% degradation under UV; 88.36% under sunlight
(Ye et al., 2024)	$Cu_3(PO_4)_2$–trypsin nanoflower; 282.1 ± 18.2 μg cm^{-2}	EVAL nanofiber membrane	β-Lactoglobulin solution	Permeation / tangential flow	98.1% degradation under permeation; 71.7% under tangential flow
(Dai, Ding, et al., 2024)	COF nanoflowers; loading NR	Nanoflower-functionalized composite membrane	Oil-in-water emulsion	Vacuum filtration	>98%; 98.4% after 10 cycles

Ref.	Nanoflower / Loading	Membrane Type	Feed Composition	Filtration Mode	Rejection / Separation
(Dai, Hu, et al., 2024a)	COF nanoflowers; loading NR	Nano-wrinkled polyamide membrane	Salt solution + antibiotics	Pressure-driven membrane separation	Desalination and antibiotic rejection
(F. Zhu et al., 2024)	CoAl-LDH@PANI nanoflower; loading NR	PAN nanofibrous membrane	Organic contaminants and emulsified wastewater	Photocatalytic membrane filtration	Organic contaminant degradation + oil/water separation
(Gao et al., 2025)	Ag@BiOCl nanoflower; loading NR	PES ultrafiltration membrane	Humic acid solution	Ultrafiltration / visible-light self-cleaning	~95% HA rejection
(Mohamad Esham et al., 2025)	TiO_2 nanoflower–calcium bentonite; loading NR	Hollow-fiber microfiltration membrane	Real refinery-produced water	Photocatalytic–membrane treatment	Refinery-water contaminant removal
(M. Li et al., 2016)	Copper-based protein nanoflowers; loading NR	Nanoscale fibrous membrane	Enzymatic/catalytic model feed	Membrane-supported catalytic treatment	Catalytic treatment performance

Collectively, these studies demonstrate that NF-based membranes consistently improve membrane performance compared with unmodified membranes; however, the reported improvements vary considerably because of differences in nanoflower composition, membrane fabrication methods, operating conditions, and feed-water characteristics. Consequently, direct comparison among published studies remains challenging. Recent research indicates a clear shift from single component nanoflowers toward multifunctional hybrid architectures that simultaneously integrate adsorption, photocatalysis, and antifouling properties. Nevertheless, standardized testing protocols and long-term performance evaluations are still lacking, limiting the ability to identify the most effective membrane designs for practical applications.

a)

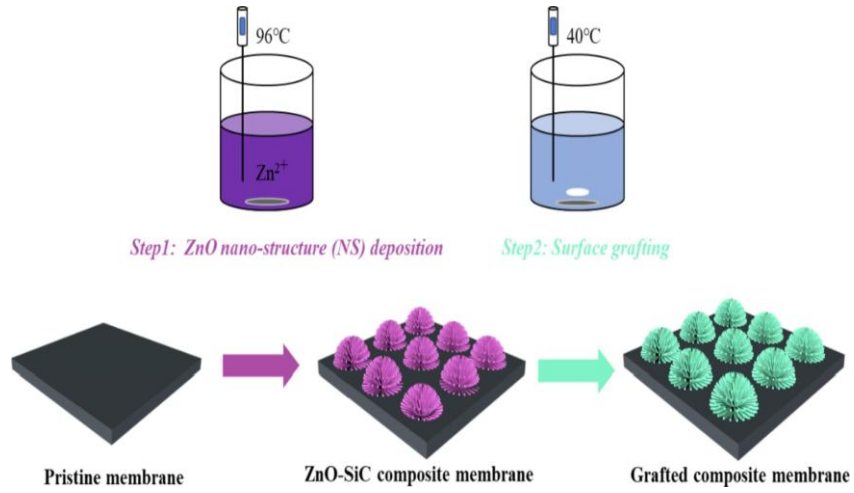
96°C
40°C
Zn2+
Step1: ZnO nano-structure (NS) deposition
Step2: Surface grafting
Pristine membrane
ZnO-SiC composite membrane
Grafted composite membrane

b)


Cu2+
Protein
PBS solution
Formation of Cu3(PO4)2 ·3H2O nuclei
Geminate crystals
Active sites
Oriented growth
Self organization
Immobilized Protein-Cu3(PO4)2 ·3H2O hybrid nanoflowers
Nuclei
Active sites
Self organization
Geminate crystals
Oriented growth
5 um

c)


Tp
Pa
Dopamine
PEG
DP
LBL
self-assembly
Co-deposition
PVDF
COF3/PVDF
DP/COF3/PVDF

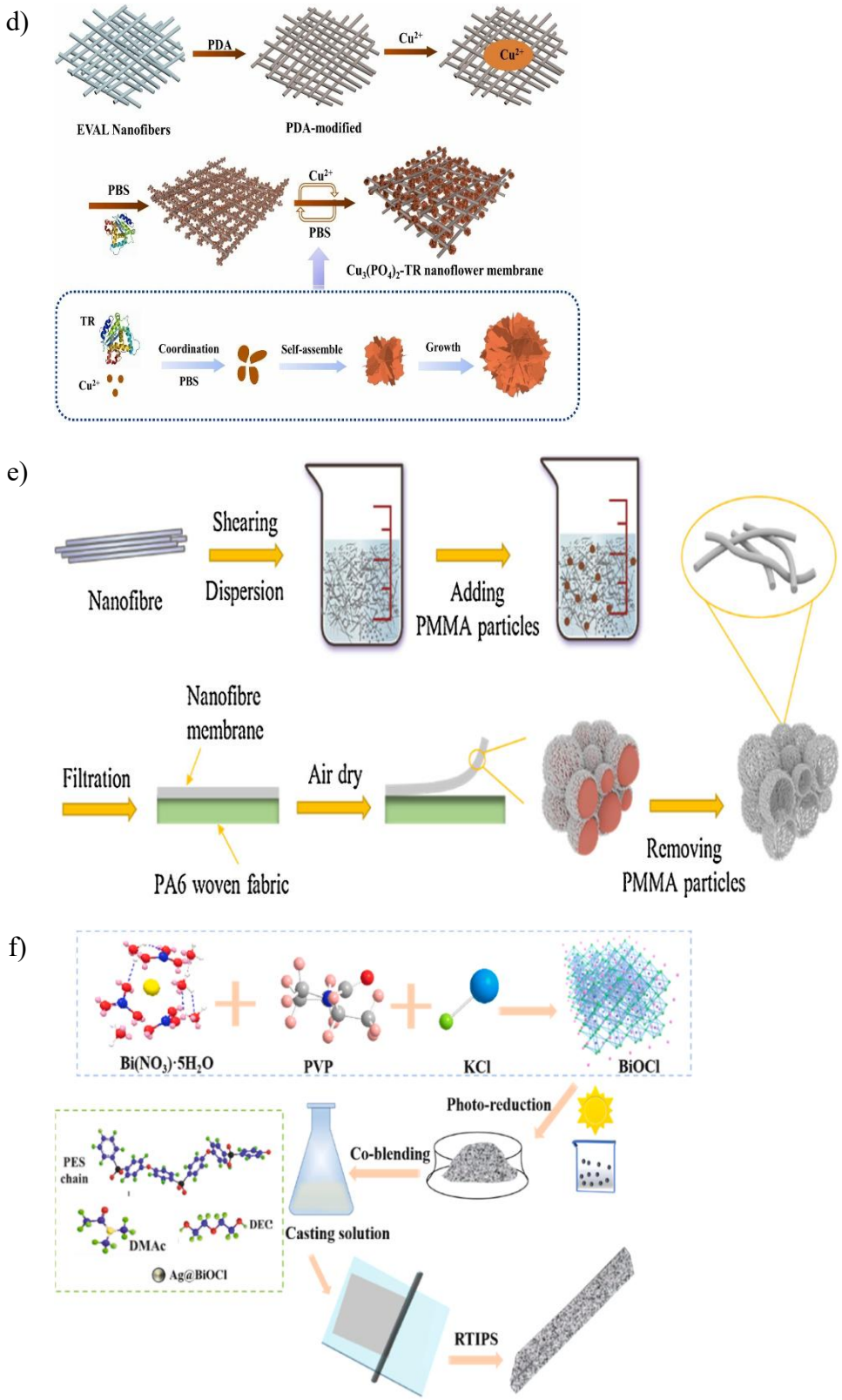

Figure 7- Fabrication of some NF-based membrane a) Schematic illustration of the ZnO NF@SiC membrane preparation.(J. Wei et al., 2022) b) Growing mechanism of Cu3(PO4)2·3H2O-protein

nanoflowers (M. Li et al., 2016) c) Fabrication process of the DP/COF3/PVDF membrane, utilizing LBL self-assembly and co-deposition techniques.(Dai, Ding, et al., 2024) d) Fabrication of the NF-embedded EVAL nanofiber layer and the growth of Cu3(PO4)2-TR hybrid NF.(Ye et al., 2024) e) Fabrication process of the hierarchically porous nanofibrous membrane.(Luo et al., 2020) f) preparation of ultrahigh antifouling ultrafiltration membrane based on Ag NPs photoreduction modified PVP/BiOCl NF for efficient membrane fouling removal. (Gao et al., 2025). Adapted with permission from Refs. 7, 84, 34, 11, 39, and 62. Copyright permissions obtained from the respective copyright holders.

a)

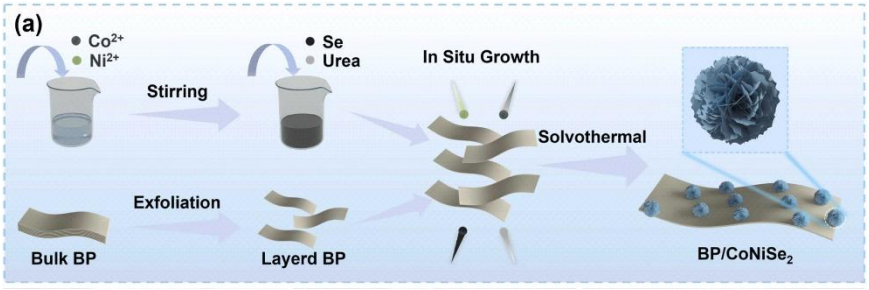

b)

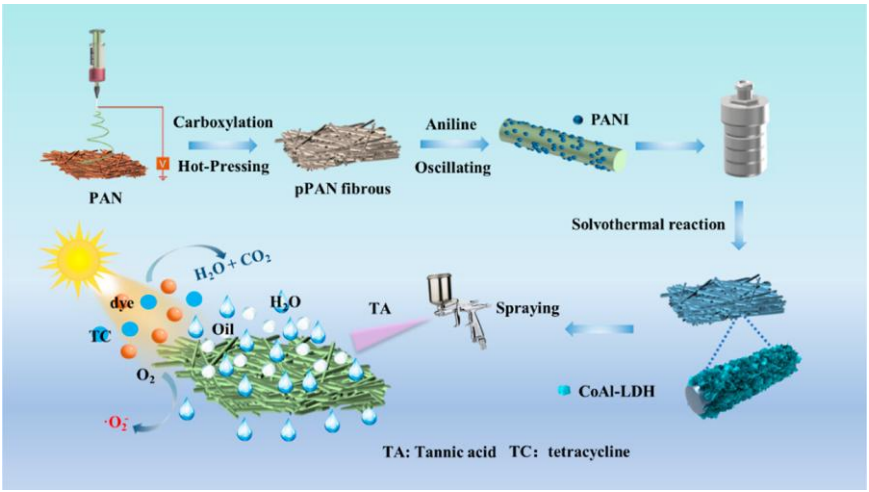

c)

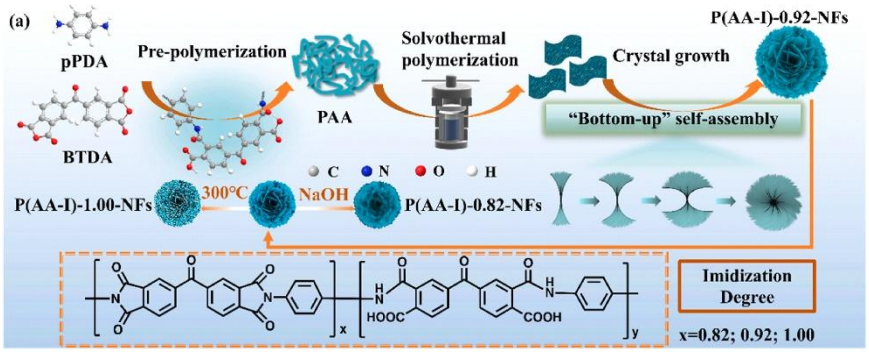

d)

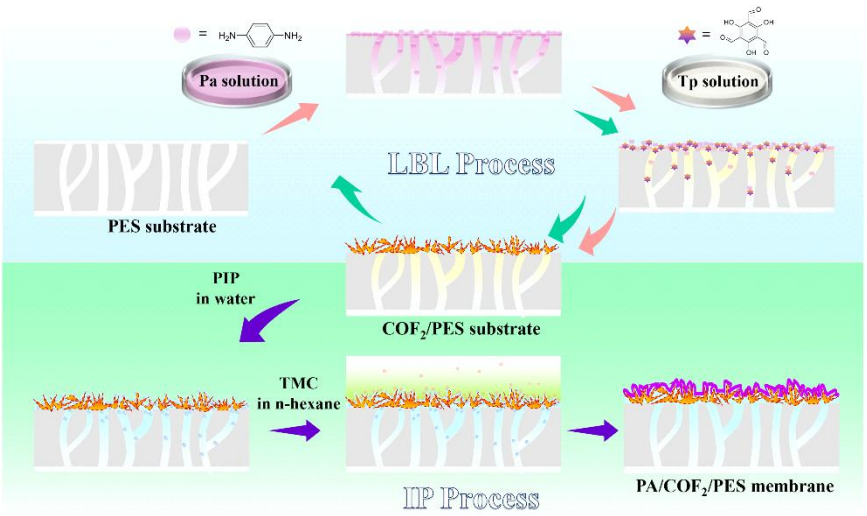
Pa solution
Tp solution
LBL Process
PES substrate
PIP
in water
COF2/PES substrate
TMC
in n-hexane
IP Process
PA/COF2/PES membrane

e)

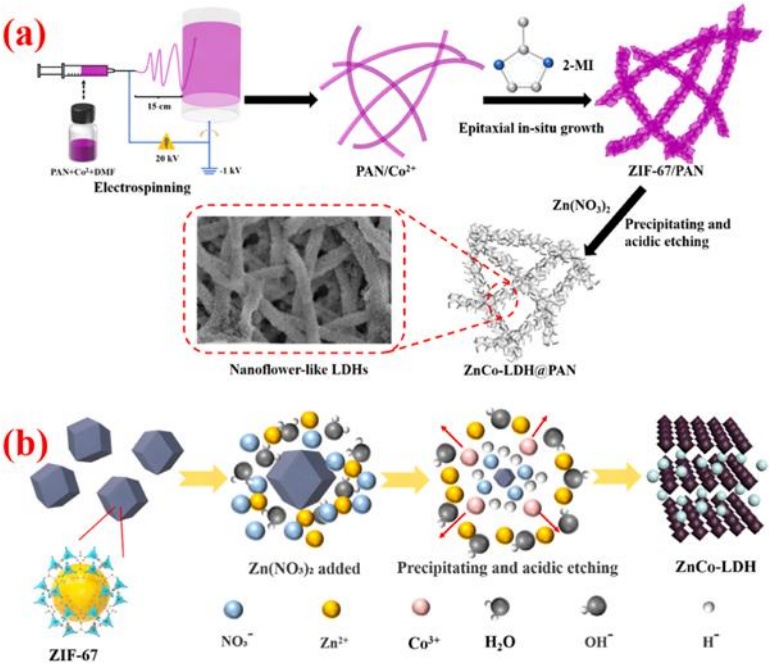
(a)
15 cm
20 kV
-1 kV
PAN+Co2+DMF
Electrospinning
PAN/Co2+
2-MI
Epitaxial in-situ growth
ZIF-67/PAN
Zn(NO3)2
Precipitating and
acidic etching
Nanoflower-like LDHs
ZnCo-LDH@PAN
(b)
ZIF-67
Zn(NO3)2 added
Precipitating and acidic etching
ZnCo-LDH
NO3-
Zn2+
Co3+
H2O
OH-
H+

f)

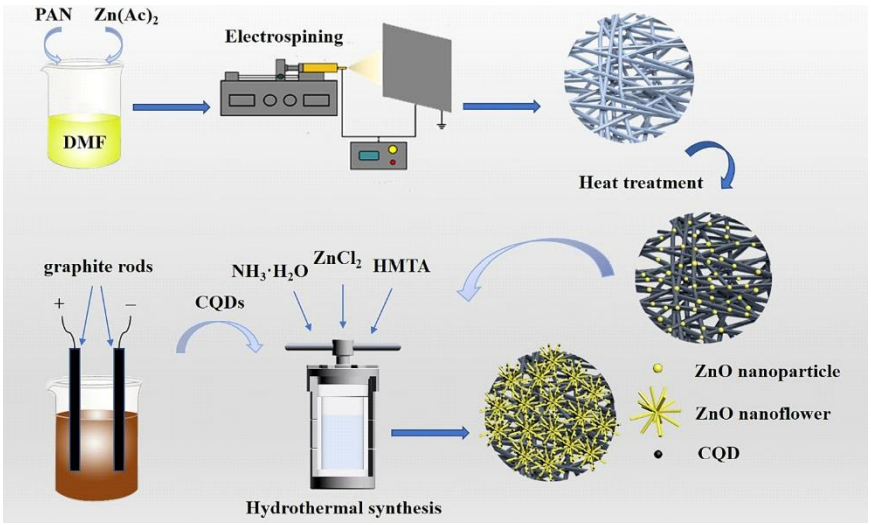
PAN
Zn(Ac)2
DMF
Electrospining
Heat treatment
graphite rods
NH3·H2O
ZnCl2
HMTA
CQDs
ZnO nanoparticle
ZnO nanoflower
CQD
Hydrothermal synthesis

Figure 8- Fabrication of some NF-based membrane a) Fabrication of some NF-based membrane. Schematic illustration for the synthesis of BP/CoNiSe2. (Wen et al., 2025). b) Schematic diagram of the heterogeneous CoAl-LDH@PANI/pPAN fibrous composite membrane(F. Zhu et al., 2024). c) Schematic diagram of the preparation process of Self-assembled NF-mediated interfacial polymerization through tunable intra- and inter-layer channels(Chen et al., 2025). d) Schematic illustration of the preparation process of PA/COF2/PES membranes(Dai, Hu, et al., 2024a). e) Illustration of the preparation proedure for the ZnCo-LDH@PAN membrane and Formation schematic of ZnCo-LDH nanoparticles on PAN nanofibers(S. Li et al., 2023). f) Schematic diagram of Carbon quantum dots-decorated ZnO heterostructure NFs grown on nanofiber membranes (H. Xu et al., 2023). Adapted with permission from Refs. 76, 83, 74, 20, 75, and 26. Copyright permissions obtained from the respective copyright holders.

1.2.4. Scalability of Fabrication Techniques

1.2.4.1.Scope: Large-Scale Application

NF-based membranes exhibit exceptional potential in laboratory-scale water and wastewater treatment due to their unique structural properties, including large surface area, higher adsorption capabilities, and improved catalytic activity. However, translating these laboratory innovations into commercially viable, large-scale applications present multiple technical and economic challenges.

A primary hurdle is the development of scalable and cost-effective fabrication methods. Current techniques, including electrochemical deposition and template-assisted growth, face limitations in producing uniform NF structures across large membrane areas (Pervez et al., 2020). Roll-to-roll manufacturing and continuous production processes show promise in achieving consistent membrane quality and large-scale output (Rahbari-Sisakht & Ismail, 2025b). Electrospinning is emerging as a viable large-scale production method, producing fibrous nanostructures with tunable porosity to enhance water filtration efficiency (Khraisheh et al., 2021).

Beyond the scalable synthesis of nanoflowers, the development of robust membrane architectures is equally important for successful industrial implementation. One promising strategy is the incorporation of nanoflower-based materials into multilayer non-woven sandwich structures,

where the active nanocomposite is immobilized between mechanically robust porous substrates. Such architectures provide enhanced structural integrity, minimize nanomaterial detachment and leaching, improve handling during continuous-flow operation, and facilitate replacement or regeneration of the active layer. Furthermore, non-woven supports are compatible with established textile and roll-to-roll manufacturing technologies, making them attractive for large-scale membrane fabrication. A recent study by Hassan et al. demonstrated this concept using a non-woven Nomex sandwich filter containing an activated carbon/polypyrrole (AC/PPy) nanocomposite fabricated by hot pressing. The multilayer filter exhibited excellent mechanical stability, prolonged operational durability, and reusability while maintaining high contaminant removal performance, illustrating how sandwich architectures can facilitate the practical immobilization of functional nanocomposites in scalable filtration systems (Hassan et al., 2025).

Although this approach has primarily been demonstrated using activated carbon/polymer composites, the same design principle could be extended to nanoflower-based membranes, where non-woven sandwich configurations may improve nanoflower immobilization, reduce catalyst leaching, enhance mechanical durability, and support pilot- and industrial-scale water treatment applications.

1.2.4.2. Challenges for Real-World Deployment

Despite promising advances in laboratory-scale studies, several barriers must be overcome before NF-based membranes can be applied in full-scale water treatment facilities. One significant concern is scalability and fabrication costs. Producing NFs with uniform morphology and controlled functionalization at industrial scale remains challenging (Pervez et al., 2020; Rahimi-Kashkouli et al., 2020). Optimization of fabrication cost and mass production efficiency is essential for commercial viability. Another challenge is the stability and durability of NF-based membranes.

NF-enhanced membranes must maintain structural integrity under high pressures, fluctuating pH levels, and dynamic ionic environments. Long-term studies are needed to evaluate performance retention under operational conditions (Gao et al., 2025; Mannina et al., 2018). Membrane fouling and compatibility issues also remain a barrier to real-field applications. While NFs improve antifouling performance, irreversible fouling mechanisms, such as organic and biofouling in real wastewater environments, require further investigation (Deng et al., 2025; Pervez et al., 2020; Rahimi-Kashkouli et al., 2020). Furthermore, environmental and health concerns need to be thoroughly addressed. Potential NF leaching into treated water poses environmental and human health risks (Brunelli et al., 2021). Understanding the fate, transformation, and toxicity of released NFs is crucial for regulatory approvals and safe deployment. Addressing these challenges through continued research and development will be critical to unlocking the full potential of NF-enhanced membranes in real-world water treatment applications.

In addition to treatment performance, the environmental safety of nanoflower-based materials should be considered during repeated use and regeneration. Changes in pH, ionic strength, natural organic matter, and cleaning conditions may influence nanoflower stability and potentially promote metal dissolution or particulate detachment. Therefore, long-term studies should evaluate material stability over multiple treatment and cleaning cycles, together with ecotoxicological assessment of potentially released species. Appropriate recovery and end-of-life management strategies should also be considered to minimize uncontrolled release of nanomaterials into aquatic environments and to support their safe implementation at larger scales (Kühnel & Nickel, 2014).

Although recent publications increasingly report excellent laboratory-scale performance, relatively few studies include pilot-scale demonstrations, continuous-flow experiments, or comprehensive techno-economic analyses. Future research should therefore focus on validating

membrane performance under realistic operating conditions while simultaneously evaluating manufacturing cost, environmental sustainability, and long-term operational reliability

1.2.4.2.1. Mechanical and Chemical Stability

Maintaining mechanical integrity and chemical stability is crucial for industrial applications. NF membranes may exhibit brittleness or structural degradation under high pressures and extreme pH (Vo et al., 2024). Strategies such as hybridizing NFs with robust support materials (e.g., MOFs and polymer composites) and applying surface cross-linking techniques have shown promise in enhancing durability (Brunelli et al., 2021). For example, embedding $Cu_3(PO_4)_2$ NFs within a nanofiber support layer improves mechanical strength while maintaining high permeability (Luo et al., 2020).

1.2.4.2.2. Fouling Mitigation

Membrane fouling remains a significant bottleneck in scaling NF membranes. Organic, inorganic, and biological matter accumulation reduces permeability and increases maintenance costs (Rahbari-Sisakht & Ismail, 2025a). Mitigation strategies include incorporating antifouling agents such as Ag nanoparticles and titanium dioxide (TiO2), as well as enhancing surface hydrophilicity (García-Ávila et al., 2024). Hybrid NF membranes incorporating photocatalytic nanomaterials have demonstrated self-cleaning capabilities under light exposure, further suppressing fouling (Gao et al., 2025).

Although contact angle measurements provide useful information regarding membrane hydrophilicity, they alone are insufficient to demonstrate durable antifouling performance. A comprehensive evaluation should include quantitative metrics such as normalized flux decline (NFD), reversible and irreversible fouling ratios (Rr and Rir), flux recovery ratio (FRR), filtration

duration, cleaning efficiency, membrane stability, and performance over repeated fouling–cleaning cycles. A limited number of studies have comprehensively reported these parameters. For example, Ag@BiOCl nanoflower-modified ultrafiltration membranes achieved an FRR of 85.98% following visible-light-assisted self-cleaning while simultaneously reporting reversible and irreversible fouling ratios, silver leaching, and antibacterial performance, providing a comprehensive assessment of membrane durability(Aydin et al., 2024; Gao et al., 2025; Luo et al., 2020). Similarly, nanoflower-branched ZnCo-LDH/PAN membranes exhibited an FRR of 97.8% and maintained stable separation performance over 10 consecutive filtration cycles, demonstrating excellent chemical and mechanical stability. Other promising systems, including nano-wrinkled polyamide membranes incorporating covalent organic framework (COF) nanoflowers, ZnO nanoflower@SiC ceramic membranes, and enzyme-immobilized nanofibrous membranes, also demonstrated enhanced permeability, fouling resistance, and operational stability during prolonged filtration or repeated reuse(Dai, Hu, et al., 2024a; K. Wang et al., 2023; J. Wei et al., 2022; F. Zhu et al., 2024). However, many studies primarily reported reductions in contact angle or improvements in surface hydrophilicity without quantitatively evaluating long-term fouling behavior, making direct comparison of membrane durability challenging. Collectively, these findings indicate that improved hydrophilicity alone should not be interpreted as evidence of durable antifouling behavior. Future investigations should therefore adopt standardized antifouling evaluation protocols that integrate surface characterization with quantitative performance metrics, including FRR, normalized flux decline, reversible and irreversible fouling ratios, cleaning efficiency, long-term filtration stability, and mechanical durability, to enable meaningful comparison and accelerate the practical development of nanoflower-based membrane systems.

1.2.4.2.3. Economic Viability and Market Integration

The economic feasibility of NF-enhanced membranes is influenced by fabrication costs, operational efficiency, and maintenance requirements. Although these membranes demonstrate superior performance, high production costs and specialized fabrication infrastructure requirements hinder widespread adoption (Qi et al., 2025; Vo et al., 2024). Collaborative research and industry partnerships are essential to develop cost-effective fabrication methods and pilot-scale demonstrations. Enhancing membrane longevity and reducing maintenance through robust hybrid designs are key to achieving economic viability and market competitiveness (Khraisheh et al., 2021; M. Yu et al., 2017).

1.2.5. Future Directions and Opportunities

Future research should focus on optimizing NF structural properties to enhance selectivity and permeability while maintaining mechanical stability. Innovations in membrane surface engineering, including bio-inspired coatings and hybrid material integration, offer promising strategies to mitigate fouling and improve structural robustness (Rahbari-Sisakht & Ismail, 2025a). Furthermore, the adoption of advanced synthesis techniques, such as 3D printing and scalable nanofiber fabrication, will play a significant role in overcoming current manufacturing limitations. (Y. Y. Lee et al., 2024) The integration of computational modeling and AI-driven design can further accelerate material discovery by predicting processing-structure-property relationships of NFs and composites with their incorporation before experimental synthesis, reducing development time and cost.

Artificial intelligence (AI) and machine learning (ML) are expected to become indispensable tools for the next generation of nanoflower-based membrane development. Recent advances

demonstrate that data-driven approaches can establish quantitative relationships between membrane composition, nanostructure, fabrication parameters, and separation performance, enabling the prediction of permeability, selectivity, fouling resistance, and long-term stability while substantially reducing experimental effort. Modern ML workflows integrate experimental data, molecular descriptors, computational simulations, and high-throughput screening to accelerate membrane material discovery and optimization. Explainable AI techniques, such as SHAP analysis and partial dependence plots, further reveal the influence of key structural parameters—including pore size, surface chemistry, functional groups, nanoparticle loading, and zeta potential—on membrane performance, thereby providing valuable design guidelines rather than merely predictive models. More recently, generative AI, large language models, inverse design strategies, and physics-informed machine learning have emerged as promising approaches for discovering novel membrane materials with targeted properties by coupling computational prediction with experimental validation. For nanoflower-functionalized membranes, these emerging methodologies could significantly accelerate the optimization of nanoflower morphology, composition, interfacial interactions, and membrane fabrication conditions, leading to multifunctional membranes with improved permeability, selectivity, antifouling properties, and operational stability. Despite these advances, challenges associated with limited standardized datasets, model interpretability, and the integration of multi-scale experimental and computational data remain barriers to widespread implementation. Future research should therefore emphasize the development of open membrane databases, hybrid physics-informed AI frameworks, and autonomous high-throughput experimentation to enable the rational design of next-generation nanoflower-based membranes for sustainable water treatment and environmental remediation (Cairone et al., 2024; Ignacz et al., 2025; L. Liang et al., 2025).

Future studies should further evaluate the environmental safety and long-term stability of the BC–NF material. In particular, potential copper release should be quantified using ICP-OES or ICP-MS under relevant water-treatment conditions, while complementary particle characterization should be performed to distinguish dissolved metal release from particulate detachment. Metal and particle mass-balance analyses would provide further information on the stability of the nanoflowers and the fate of copper during treatment. Repeated cleaning and regeneration experiments should also be conducted to determine whether material reuse promotes copper leaching or structural deterioration. In addition, ecotoxicological assessment and appropriate recovery and end-of-life disposal strategies should be investigated before considering larger-scale application of the material (Bour et al., 2015; Tran et al., 2024).

In conclusion, NF-based membranes offer promising possibilities for water and wastewater treatment; however, addressing challenges related to scalability, stability, fouling, and economic viability is equally important. Continuous-flow hydrothermal or solvothermal synthesis, additive manufacturing, and electrospinning approaches can enable uniform, large-scale production of NF membranes with precise architecture. Evaluating chemical stability under extreme pH, oxidizing environments, and high-pressure operation, along with life-cycle analysis and cost modeling, will ensure the membranes are both durable and economically viable. Ultimately, interdisciplinary collaboration among material scientists, chemical engineers, environmental researchers, and data scientists will be pivotal in translating NF-based membranes from laboratory innovation to industrial-scale application, unleashing their full potential in sustainable and energy-efficient water treatment systems. Current research trends indicate a gradual transition from empirical membrane development toward data-driven materials engineering. Machine learning, high-throughput computational screening, and digital process optimization are expected to accelerate the

identification of optimal NF morphologies, compositions, and fabrication conditions. These approaches may substantially reduce experimental costs while enabling the rational design of multifunctional membranes with improved permeability, selectivity, durability, and environmental safety.

1.2.6. Conclusion

Three-dimensional nanoflower (NF)-based membranes have emerged as a new generation of multifunctional membrane materials capable of addressing several long-standing challenges in water and wastewater treatment. Their hierarchical flower-like architectures provide high surface area, abundant exposed active sites, interconnected transport pathways, and tunable surface chemistry, enabling simultaneous enhancement of adsorption, membrane separation, photocatalytic activity, hydrophilicity, antifouling behavior, and contaminant selectivity. Unlike conventional nanomaterials, the unique three-dimensional morphology of NFs promotes improved interfacial compatibility with membrane matrices, efficient mass transport, and higher accessibility of reactive sites, and overall membrane performance.

This review critically demonstrates that the performance of NF-based membranes is governed not only by their chemical composition but also by the intricate relationships among nanoflower morphology, petal thickness, defect density, surface functionality, interfacial adhesion, and membrane fabrication strategy. The literature consistently shows that rational engineering of these structural characteristics can simultaneously improve water permeability, contaminant rejection, catalytic efficiency, and fouling resistance while mitigating the traditional permeability-selectivity trade-off. Nevertheless, the reported performance improvements vary considerably because of differences in synthesis methods, membrane substrates, operating conditions, and characterization

protocols, highlighting the urgent need for standardized evaluation procedures that enable meaningful comparison across different studies.

Despite remarkable laboratory-scale progress, several fundamental challenges continue to limit the practical implementation of NF-based membranes. Long-term structural stability under realistic operating conditions, nanoflower detachment and metal leaching, membrane durability during repeated cleaning cycles, and performance in complex water matrices containing natural organic matter, competing ions, microorganisms, and suspended solids remain insufficiently understood. Furthermore, most published studies rely on short-term experiments using simplified synthetic feed solutions, while relatively few investigations have evaluated pilot-scale operation, long-term membrane performance, environmental safety, life-cycle sustainability, or techno-economic feasibility. Addressing these knowledge gaps will be essential for translating laboratory achievements into reliable industrial technologies.

Future progress will depend on integrating advanced materials engineering with computational and data-driven approaches. Artificial intelligence, machine learning, molecular simulations, and digital modeling provide unprecedented opportunities to accelerate nanoflower design, predict membrane performance, optimize fabrication parameters, and establish quantitative structure-property-performance relationships. When combined with scalable manufacturing techniques such as continuous hydrothermal synthesis, electrospinning, additive manufacturing, and roll-to-roll membrane production, these emerging technologies have the potential to significantly reduce development time while improving reproducibility, cost-effectiveness, and commercial scalability.

Overall, 3D NF-based membranes represent a highly promising and rapidly evolving platform for sustainable water purification. Their ability to integrate multiple treatment mechanisms within a single membrane architecture offers significant opportunities for developing energy-efficient,

high-performance, and environmentally sustainable separation technologies. Future research should move beyond maximizing laboratory-scale performance toward establishing standardized testing protocols, validating long-term operation under realistic conditions, ensuring environmental safety, and developing economically viable manufacturing strategies. Achieving these objectives will require close collaboration among materials scientists, membrane engineers, environmental researchers, computational scientists, and industrial stakeholders. Such interdisciplinary efforts will ultimately enable the successful transition of NF-based membranes from promising laboratory materials to robust, commercially deployable technologies capable of addressing global water and wastewater treatment challenges.

1.3 Proposed Research

1.3.1 Research Gap

The literature reviewed in this chapter demonstrates that advanced functional materials have shown considerable potential for water and wastewater treatment because of their high surface area, abundant active sites, tunable physicochemical properties, and multifunctional capabilities. Nanoflower (NF)-based materials have emerged as promising candidates due to their hierarchical architectures and excellent catalytic, adsorption, and antimicrobial performance. However, despite these advances, several challenges remain, including material stability, recovery, scalability, cost, and practical implementation. These limitations highlight the need to develop sustainable, high-performance materials using environmentally friendly and economically feasible design strategies.Although nanoflower-based materials have demonstrated excellent catalytic and antimicrobial properties, most reported systems consist of free-standing particles that suffer from aggregation, recovery difficulties, and reduced structural stability. While biochar has emerged as an environmentally friendly support material because of its porous structure and abundant surface

functional groups, studies integrating biochar with curcumin-mediated copper phosphate nanoflowers remain very limited. Moreover, the synergistic interactions among biochar, curcumin, and copper phosphate nanoflowers, together with their influence on composite structure and antibacterial performance, have not been comprehensively investigated.

In addition, among current water quality challenges, road salt application has become a major source of chloride contamination in freshwater systems. Existing chloride removal technologies, including reverse osmosis, electrodialysis, and ion exchange, are generally energy-intensive, expensive, and unsuitable for large-scale environmental remediation. Although SAPs have been widely investigated for the removal of heavy metals and organic contaminants, and waste eggshells have demonstrated considerable potential as calcium-rich materials for environmental applications, these materials have largely been studied independently. Their integration into a single composite system for chloride removal from road salt-contaminated freshwater has received little attention, and the combined mechanisms of water absorption, ion concentration, and calcium-assisted chloride capture have not been systematically investigated. Furthermore, the application of such sustainable materials for treating real freshwater systems remains largely unexplored.

Motivated by these research gaps, this thesis investigates two complementary approaches for developing sustainable functional materials for water treatment. The first study develops BC–NFs through an in situ biomimetic self-assembly strategy. In this approach, biochar acts as a sustainable support for the growth and stabilization of copper phosphate nanoflowers in the presence of curcumin. This approach aims to produce a multifunctional material with enhanced structural stability and antibacterial performance.

Building upon the broader insights gained from the literature review, particularly the need for sustainable and application-specific materials, the second experimental study adopts a different

material design strategy by developing SAP–EGS for chloride removal from freshwater. While the BC–NFs composite provides a multifunctional antibacterial platform, the SAP–EGS composite addresses chloride contamination, collectively contributing to the development of environmentally sustainable materials for water treatment and environmental remediation.

1.3.2 Objectives

I. To synthesize and characterize a sustainable biochar-supported curcumin–copper phosphate nanoflower (BC-NFs) composite and evaluate its physicochemical properties and antimicrobial performance for potential water treatment applications.

Hypothesis: Immobilizing curcumin–copper phosphate nanoflowers on a porous biochar support will improve nanoflower stability, surface area, and antimicrobial activity through synergistic interactions between biochar, curcumin, and copper phosphate, making the BC-NFs composite a promising multifunctional material for water treatment applications.

II. To develop and evaluate a sustainable superabsorbent polymer–eggshell (SAP-EGS) composite for efficient chloride removal from freshwater, with emphasis on material characterization, removal mechanisms, adsorption performance, and practical application for urban lake water treatment.

Hypothesis: The integration of waste EGS with a superabsorbent polymer (SAP) will significantly enhance chloride removal from freshwater by combining water absorption, chloride concentration, and calcium-mediated precipitation, resulting in higher removal efficiency than either material used individually.

1.3.3 Novelty

The novelty of this research lies in the development of two sustainable material systems that utilize waste-derived resources and advanced functional materials to address important challenges in water treatment. First, this research develops a sustainable biochar-supported curcumin–copper phosphate nanoflower (BC–NFs) composite through an in situ biomimetic self-assembly approach. While biochar-supported nanomaterials, copper phosphate nanoflowers, and curcumin-based antimicrobial systems have each been investigated individually, their integration into a single multifunctional platform has not been previously reported. In this study, porous biochar serves as a sustainable support for the in-situ growth of hierarchical copper phosphate nanoflowers in the presence of curcumin, producing a multifunctional material with enhanced structural stability, high surface area, and improved antibacterial performance. The synergistic interactions among biochar, curcumin, and copper phosphate nanoflowers provide complementary structural and functional advantages while utilizing waste-derived materials.

In addition, this study introduces a novel SAP-EGS composite for chloride removal from freshwater. Unlike conventional chloride removal technologies that rely on energy-intensive membrane processes or ion-exchange systems, the proposed material combines the water absorption capacity of superabsorbent polymers with the calcium-rich composition of waste EGSs to facilitate chloride removal through a synergistic absorption and calcium-mediated removal mechanism. To the best of our knowledge, this is the first study to integrate waste EGSs with a superabsorbent polymer for chloride remediation in freshwater systems. Together, these studies demonstrate innovative strategies for transforming low-cost, renewable resources into high-value functional materials for sustainable water treatment and environmental remediation, supporting the principles of the circular economy.

Chapter 2: Biochar-Supported Curcumin-Copper Phosphate Hybrid Nanoflowers: Synthesis, Characterization and Antibacterial Performance

Sama Khalili Moradkhanloo, Ratul Kumar Das, Siu-Ning Leung, Satinder Kaur Brar (submitted to Materials Chemistry and Physic)

2.1 Introduction

Biochar is a sustainable, porous support material with a large surface area and abundant functional groups that facilitate nanomaterial immobilization, contaminant adsorption, and mass transfer. Its tunable surface chemistry improves nanoparticle dispersion, structural stability, and composite performance, making it suitable for multifunctional materials in environmental remediation and antibacterial applications. (Q. Song et al., 2024). Biochar provides nucleation and anchoring sites that improve nanomaterial dispersion and reduce aggregation. Its conductive carbon framework can facilitate electron transfer and enhance the catalytic and photocatalytic performance of supported nanomaterials. Consequently, biochar-supported composites can offer improved adsorption, stability, and contaminant removal compared with pristine nanomaterials. TiO_2-biochar and ZnO-biochar composites further demonstrate the synergistic benefits of combining biochar with semiconductor nanomaterials.(Ahmad et al., 2024; Kamali et al., 2021; W. Xu et al., 2024) Recent studies have demonstrated that biochar-supported composites can

achieve over 93% degradation of naphthenic acids under simulated solar irradiation. (An et al., 2024)

Nanoflowers (NFs) are hierarchical three-dimensional structures with interconnected nanosheets or petal-like features that provide high surface area, abundant active sites, and porous networks. These properties enhance mass transfer, adsorption, catalysis, and antibacterial performance, making NFs useful in environmental and biomedical applications. Organic–inorganic hybrid nanoflowers (HNFs), introduced by Zare and co-workers in 2012, are formed through coordination-driven self-assembly of organic molecules with metal phosphate crystals. Their morphology and properties can be tailored by controlling synthesis conditions such as pH, temperature, metal concentration, and reaction time. (Ge et al., 2012b; Jafari-Nodoushan et al., 2022b; S. Y. Lee et al., 2024a)

Consequently, HNFs have been widely investigated for enzyme immobilization, biosensing, biocatalysis, pollutant degradation, adsorption, wastewater treatment, and biomedical applications. More recently, enzyme-free and biomolecule-assisted HNFs incorporating amino acids, plant metabolites, and natural polymers have expanded their applications to antibacterial materials and advanced environmental technologies. Similarly, inorganic metal oxide NFs, such as ZnO, exhibit enhanced photocatalytic, sensing, and antibacterial performance owing to their high surface-to-volume ratio, porous architecture, and improved light absorption. Overall, the hierarchical morphology, tunable composition, and multifunctional physicochemical properties of NFs make them promising building blocks for next-generation materials for simultaneous adsorption, catalysis, and microbial control in water treatment systems.(Cui & Jia, 2017; S. Y. Lee et al., 2024a; Nayak et al., 2023; Yilmaz et al., 2022)

Curcumin is a natural polyphenol with antioxidant, anti-inflammatory, and antibacterial properties. It can inhibit bacteria through several mechanisms and also acts as a reducing, capping, and structure-directing agent in nanoparticle synthesis. These properties make it a useful component for developing stable and biocompatible hybrid antibacterial nanomaterials (El-Kattan et al., 2025).

Curcumin is a natural polyphenol with antioxidant, anti-inflammatory, and antibacterial properties. It can inhibit bacteria through several mechanisms and also acts as a reducing, capping, and structure-directing agent in nanoparticle synthesis. These properties make it a useful component for developing stable and biocompatible hybrid antibacterial nanomaterials.(Alobaidi & Rahmah, 2026; El-Kattan et al., 2025; Gwon et al., 2024; Koca et al., 2020; Yilmaz et al., 2022)

The combination of biochar with functional nanomaterials has been shown to enhance material stability and nanoparticle dispersionwhile preserving the high surface area and porous architecture of the biochar support. These synergistic interactions improve catalytic and antibacterial performance, making biochar an attractive substrate for immobilizing HNFs and developing multifunctional composites for environmental remediation and antibacterial applications.(Kaur & Kaur, 2022b; Y. Li et al., 2020; Y. Liu et al., 2024b; Mankomal et al., 2024; Weidner et al., 2022)

Although biochar-supported nanomaterials, copper phosphate NFs, and curcumin-based antimicrobial systems have each been reported independently, to the best of our knowledge, this study is the first to integrate these three components through an in situ biomimetic self-assembly approach to produce a sustainable multifunctional material. The resulting hierarchical BC-NFs platform combines the structural advantages of porous biochar, the bioactivity of curcumin, and the high surface area of copper phosphate nanoflowers. The porous biochar matrix was employed to improve curcumin–copper phosphate hybrid nanoflower (CCPHNFs) immobilization, structural

stability, and accessibility of active sites, while the combined presence of copper phosphate nanoflowers and curcumin was hypothesized to contribute to antibacterial activity. It was further hypothesized that biochar would enhance nanoflower dispersion and accessibility of antibacterial active sites, resulting in improved antibacterial performance. The synthesized BC-NFs composite was characterized using scanning electron microscopy (SEM), energy-dispersive X-ray spectroscopy (EDS), X-ray diffraction (XRD), Fourier-transform infrared spectroscopy (FTIR), fluorescence microscopy, and Brunauer–Emmett–Teller (BET) analysis, and its antibacterial activity against *Escherichia coli* was evaluated. Given the importance of controlling microbial contamination and biofouling in water treatment systems, BC-NFs also shows potential as an antibacterial filtration material or as a functional material for incorporation into membrane-based treatment systems.

2.2. Materials and Methods

2.2.1 Materials

Biochar used in this study was supplied by Bella Biochar (Natural Capital), Canada, and was produced from landfill-diverted forest debris and wood waste, with a particle size of less than 2 mm. Curcumin (≥94% purity), copper(II) sulfate pentahydrate ($CuSO_4 \cdot 5H_2O$), sodium chloride (NaCl), potassium chloride (KCl), disodium hydrogen phosphate (Na_2HPO_4), and potassium dihydrogen phosphate (KH_2PO_4) were purchased from Sigma-Aldrich. Escherichia coli (E. coli) strain used for the antibacterial assays was obtained from the Agricultural Research Service Culture Collection (NRRL, USA). Ciprofloxacin (CIP) tablets were used as a reference antibacterial agent. Deionized water (DI water) was used throughout all experiments.

2.2.2 Synthesis of Curcumin–Copper Phosphate Hybrid Nanoflowers (CCPHNFs)

CCPHNFs were synthesized using a biomimetic self-assembly approach. Briefly, 10 mL of PBS solution was mixed with 10 mL of $CuSO_4$ solution at various concentrations (0.8, 5, 10, 25, 50, 100, and 200 mM). Subsequently, 2 ml of 5.5 μM curcumin solution prepared in methanol was added to each mixture.

The resulting suspensions were incubated at room temperature for 72 h to allow the formation of CCPHNFs. After incubation, the precipitates were separated from the supernatant by centrifugation at 12000 rpm for 11 min. The collected precipitates were washed several times with deionized water and dried in room temperature for 72 hrs. for further characterization. For FTIR analysis, copper phosphate nanoflowers (CPHNFs) were prepared as a control using the same synthesis conditions and material concentrations, but without the addition of curcumin.

2.2.3 Synthesis of Biochar-Supported Nanoflowers (BC-NFs)

BC-NFs were synthesized following a similar procedure. Briefly, various amounts (0.1, 0.2,0.4,0.8 g) of biochar were submerged in 10 mL of PBS solution. Subsequently, 10 mL of 100 mM $CuSO_4$ solution and 2 mL of 0.5 μM curcumin methanolic solution were added to the suspension.

The mixture was incubated at room temperature for 72 h to facilitate the in-situ growth of CCPHNFs on the biochar surface. Following incubation, the resulting BC-NFs composite was collected by centrifugation, washed thoroughly with deionized water to remove unreacted species, and dried before characterization and antibacterial testing.

2.2.4 Material Characterization

The morphology and microstructure of the synthesized CCPHNFs prepared at different $CuSO_4$ concentrations using a JEOL JSM-6610LV scanning electron microscope (JEOL Ltd., Tokyo, Japan). Before imaging, the samples, including the BC–NFs composite, were sputter-coated with platinum and examined under high-vacuum conditions using a Zeiss Gemini 360 FESEM for scanning electron microscopy (SEM).. Elemental composition and elemental distribution of BC-NFs were determined using energy-dispersive X-ray spectroscopy (EDS).

The crystalline structure of the synthesized CCPHNFs was analyzed using X-ray diffraction (XRD) Bruker D8 Advance ECO diffractometer (Bruker AXS GmbH, Karlsruhe, Germany) equipped with Cu Kα radiation (λ = 1.5406 Å). The diffraction patterns of the synthesized CCPHNFs were compared with standard copper phosphate crystal patterns to confirm successful CCPHNFs formation.

FTIR was employed to identify the surface functional groups of CCPHNFs and CPHNFs, and pristine BC and the BC-NFs. FTIR spectroscopy was performed using a PerkinElmer Spectrum Two FT-IR spectrometer (PerkinElmer Inc., Waltham, MA, USA) employing the KBr pellet technique. Approximately 1–2 mg of each dried sample was thoroughly mixed with spectroscopic-grade KBr and compressed into transparent pellets under high pressure. The FTIR spectra were recorded over the wavenumber range of 4000–400 cm^{-1} to identify the functional groups and chemical bonds present in the biochar, CCPHNFs, and BC-NFs composite.

The specific surface area, pore volume, and pore size distribution of BC, CCPHNFs, and BC-NFs samples were determined using NOVA 1200e Brunauer–Emmett–Teller (BET) nitrogen absorption instrument.

2.2.5 Antibacterial Activity

The antibacterial activity of the synthesized BC-NFs composite was evaluated against Escherichia coli (E. coli) using the agar well diffusion method. Briefly, E. coli cultures were uniformly spread onto nutrient agar plates to form a bacterial lawn. Three wells of equal diameter were aseptically made in each agar plate using a sterile cork borer. For the first plate, 20 µL of the *E. coli* culture was spread onto the agar surface, while 15 µL was used for the second and third plates**.** Three wells of equal diameter were aseptically made in each agar plate using a sterile cork borer. For the first plate, 20 µL aliquots of BC-NFs and CCPHNFs suspensions were added to the respective wells. For the second plate, 20 µL of ciprofloxacin (CIP), 20 µL of sterile DI water, and 20 µL of BC-NFs suspension were added to the respective wells. For the third plate, 20 µL aliquots of CPHNFs and curcumin solutions were added to the respective wells. The plates were incubated at 30 °C for 24 h, after which the diameters of the inhibition zones surrounding each well were measured.The experiment was conducted using three independent agar plates, with each treatment tested once per plate (n = 3), and the results were reported as mean ± standard deviation (SD). The diameters of the inhibition zones were measured from digital images using Fiji (ImageJ) after calibration with a known reference length. Only the clear inhibition zone surrounding the well was measured, excluding the diameter of the well itself. The antibacterial activity of the BC-NFs composite was assessed by comparing the inhibition zone diameters with those of the positive and negative controls.

2.3. Results and Discussion

2.3.1 Characterization of CCPHNFs

2.3.1.1 Morphological Analysis (SEM)

The morphology of the synthesized CCPHNFs was investigated using SEM. Samples were synthesizedingCuSO₄ concentrations ranging from 0.8 to 200 mM in the presence and absence of curcumin. As shown in Figure 9, the CuSO₄ concentration significantly influenced the nucleation and growth of the flower-like structures.As the CuSO₄ concentration increased, a gradual transition from poorly developed aggregates to more defined flower-like hierarchical structures was observed. At lower concentrations (0.8–25 mM), the structures were less developed and more irregular, whereas higher concentrations (50–200 mM) promoted the formation of more distinct spherical architectures composed of interconnected nanosheets. CCPHNFs SEM images are provided in Figure 9(g-m).

Samples synthesized without curcumin exhibited irregular aggregates and poorly developed morphologies, particularly at low CuSO₄ concentrations which are shown in Figure 9(a-f). In contrast, the addition of curcumin promoted the formation of well-defined hierarchical architectures. At CuSO₄ concentrations of 50–200 mM, spherical CCPHNFs composed of densely packed nanosheets were observed. Among the synthesized samples, the 100 and 200 mM CuSO₄ conditions produced well-defined flower-like structures. The 100 mM condition was selected for subsequent characterization and composite preparation based on the overall morphology and experimental considerations.

Higher magnification images revealed that the CCPHNFs consisted of interconnected petal-like nanosheets radiating outward from a central core, forming highly rough and porous

microspheres . The hierarchical architecture is expected to provide a large accessible surface area and abundant active sites, which are advantageous for antibacterial applications.

The formation of these structures can be attributed to the coordination interactions between Cu^{2+} ions, phosphate ions originating from PBS, and curcumin molecules acting as organic structure-directing agents during the self-assembly process.

The improved hierarchical morphology observed in the presence of curcumin can be attributed to its interaction with Cu^{2+} during copper phosphate formation. Curcumin contains an α,β-unsaturated β-diketone moiety capable of chelating Cu^{2+}, with the enolic group participating in metal coordination. Koshy and Das reported that this curcumin–Cu^{2+} interaction plays an important role in the formation of curcumin–copper phosphate hybrid nanoflowers and suggested that the metal-binding sites of curcumin can influence crystal growth planes rather than simply increasing the overall growth rate. They further observed that curcumin accumulation on primary copper phosphate crystals promoted the formation of interconnected nano-petals and more developed hierarchical structures.

Accordingly, the more defined flower-like morphology observed for the CCPHNFs in the present study is likely associated with curcumin-mediated modification of the nucleation and subsequent crystal-growth process. Curcumin may coordinate with Cu^{2+} during the early stages of formation, influencing the availability and growth of different crystal faces and promoting the development of the interconnected nanosheet/petal architecture. This interpretation is consistent with the reported observation that curcumin concentration affects the morphology of copper phosphate hybrid nanoflowers, where increasing curcumin concentration altered crystal-growth planes and resulted in more highly foliated structures.

a)

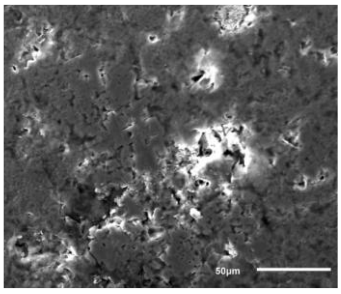

b)

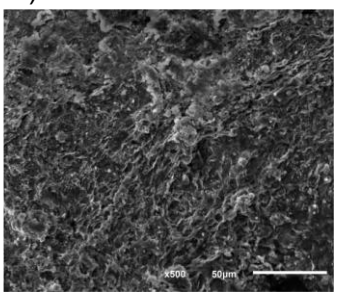

c)

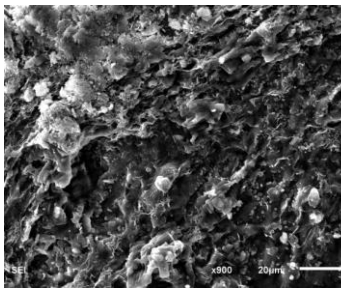

d)

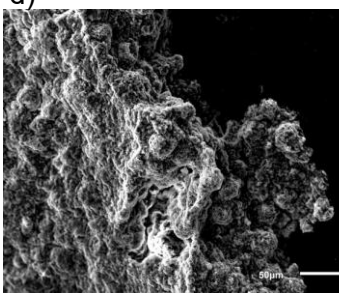

e)

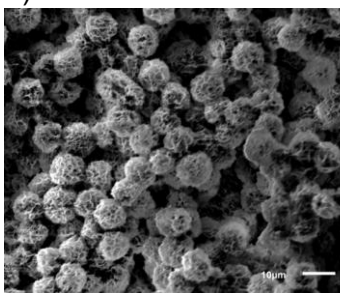

f)

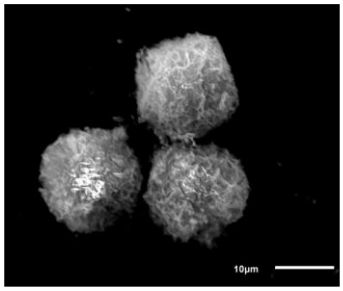

g)

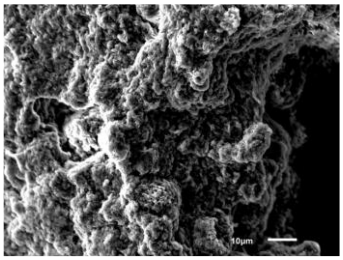

h)

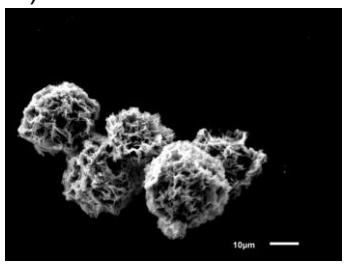

i)

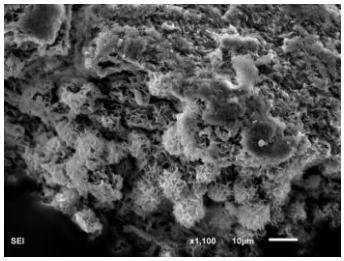

j)

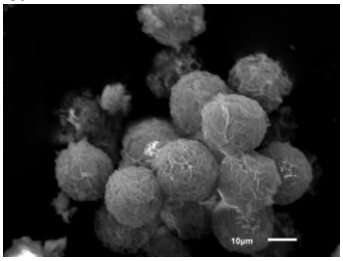

k)

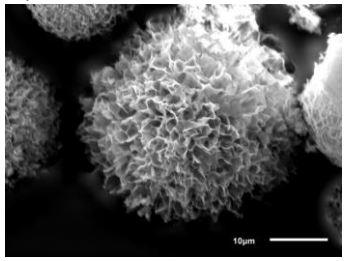

l)

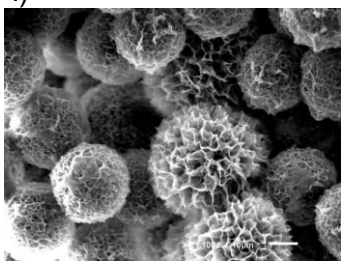

m)

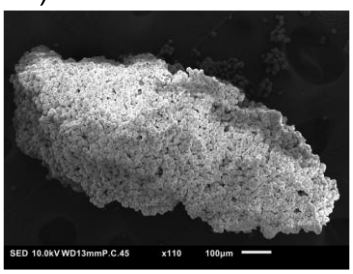

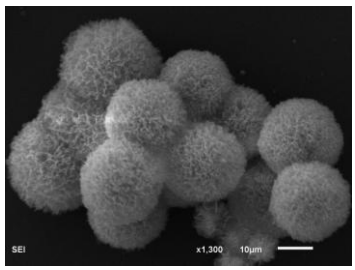

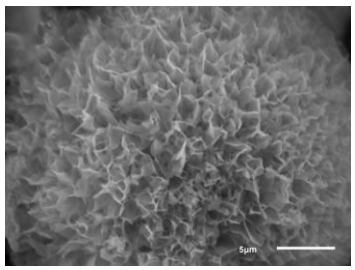

Figure 9- Morphological and structural characterization of n CPHNFs and CCPHNFs synthesized at different $CuSO_4$ concentrations. SEM images of CCPHNFs synthesized using, (a) 5 mM, (b) 10 mM, (c) 25 mM, (d) 50 mM, (e) 100 mM, and (f) 200 mM $CuSO_4$ and, SEM images of CCPHNFs synthesized using, (g) 5 mM, (h) 10 mM, (i) 25 mM, (j) 50 mM, (k) 100 mM, and (l) 200 mM $CuSO_4$ in the presence of 0.5 μM curcumin. Three representative SEM images (m) at different magnifications are presented for the 100 mM sample to highlight the hierarchical flower-like morphology.

2.3.1.2 Crystal Structure Analysis (XRD)

The XRD patterns of the synthesized copper phosphate crystal and copper phosphate hybrid nanoflowers (CCPHNFs) are presented in Figure 10. Both samples exhibited diffraction features characteristic of copper (II) phosphate trihydrate ($Cu_3(PO_4)_2 \cdot 3H_2O$), consistent with the standard JCPDS card No. 00-022-0548. The CCPHNFs pattern showed prominent reflections at approximately 12.95°, 29.81°, 33.47°, and 53.37° (2θ), which correspond to the (021), (004), (114), and (152) planes, respectively. These values are in good agreement with previously reported characteristic reflections of $Cu_3(PO_4)_2 \cdot 3H_2O$ at 12.82° (021), 29.55° (004), 33.80° (114), and 53.55° (152). In addition, diffraction features were observed at approximately 18°, 20°, 24°, 37°, 41°, 45°, and 56°, further supporting the formation of the copper phosphate phase. A prominent low-angle reflection was observed at approximately 8° in both samples; however, its position differs from the reported 8.93° (020) reflection, and therefore this peak was not assigned to a specific crystal plane. Overall, the agreement of the major diffraction peaks with the reported $Cu_3(PO_4)_2 \cdot 3H_2O$ reflections supports the formation of the copper phosphate phase in the synthesized CCPHNFs.

Compared with the synthesized copper phosphate crystal, the CCPHNFs exhibited lower intensities and broader profiles for several of the prominent reflections, together with a slightly higher background. These features are consistent with reduced crystallinity and potentially smaller crystallite dimensions in the hybrid nanoflowers. Peak broadening, however, can also arise from factors such as lattice strain, structural defects, or other sources of disorder; therefore, crystallite

size was not directly quantified in this study. The observed changes in diffraction profile are likely associated with the incorporation of curcumin during nanoflower formation, although XRD alone cannot establish the specific contribution of the self-assembly process to peak broadening. Importantly, the characteristic copper phosphate reflections were retained after incorporation of curcumin, indicating that the formation of the hybrid structure did not result in a detectable change in the underlying $Cu_3(PO_4)_2 \cdot 3H_2O$ crystal phase. Similar preservation of the copper phosphate crystal phase has been reported for hybrid $Cu_3(PO_4)_2$ nanoflowers formed in the presence of organic or biomolecular components. .

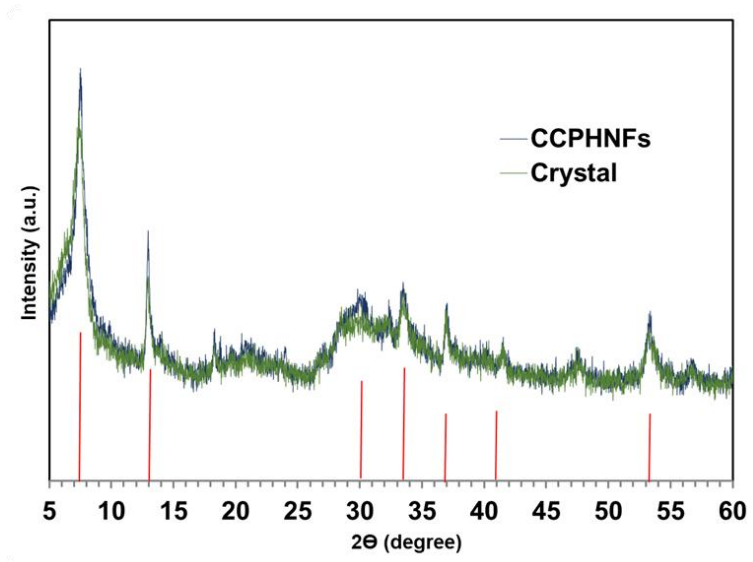

Figure 10- X-ray diffraction (XRD) patterns comparing the synthesized copper phosphate nanoflowers with the reference crystalline copper phosphate phase, confirming the successful formation of crystalline CCPHNFs.

2.3.1.3 Functional Group Analysis (FTIR)

FTIR spectroscopy was employed to investigate the chemical structure of CPHNFs and CCPHNFs(Figure 11. a. and Table 4). Both spectra exhibited characteristic phosphate-related absorption bands in the region between 500 and 1200 cm^{-1}, corresponding to Cu–O, P–O, and P–O–Cu vibrations, confirming the formation of copper phosphate structures.

The CCPHNFs displayed additional absorption bands associated with aromatic C=C vibrations and hydroxyl (O–H) stretching groups. These bands are characteristic of curcumin and indicated its successful incorporation within the CCPHNFs matrix.

Compared with CPHNFs , the curcumin-containing sample exhibited increased peak intensity and slight band shifts in several regions, suggesting interactions between curcumin functional groups and copper ions during CCPHNFs formation. These interactions likely facilitated the self-assembly process and contributed to the development of the hierarchical flower-like morphology observed by SEM.

Table 4. FTIR absorption bands and corresponding functional group assignments of CPHNFs and CCPHNFs .

Peak Position (cm^{-1})	**Functional Group / Vibration**	**Attribution**
~3400–3300	O–H stretching	Hydroxyl groups of curcumin and adsorbed water
~1630	Aromatic C=C stretching / H–O–H bending	Characteristic aromatic structure of curcumin
~1100–1030	ν_3(P–O) asymmetric stretching	Phosphate groups in the copper phosphate framework
~990–960	P–O–Cu stretching	Copper phosphate network formation
~620–560	O–P–O bending	Phosphate groups in copper phosphate
~560–500	Cu–O vibration	Cu–O bonds confirming copper phosphate nanoflower formation

Overall, the FTIR results confirm the successful formation of a CCPHNFs structure containing both inorganic phosphate networks and organic curcumin functionalities.

FTIR analysis confirmed the presence of phosphate- and copper-related functional features in the synthesized CCPHNs, while changes in the characteristic bands of curcumin indicate interactions between curcumin functional groups and copper ions. Curcumin contains an enolic β-diketone group capable of coordinating with Cu^{2+} ions. Previous studies on curcumin–copper

phosphate hybrid nanoflowers have reported that this interaction can influence crystal growth and promote the development of interconnected nanopetals. Therefore, the presence of curcumin likely contributes not only to the chemical composition of the hybrid nanoflowers but also to their hierarchical morphology through modification of the crystal-growth process.

2.3.1.4 Fluorescence Microscopy

Fluorescence microscopy was employed to verify the presence of curcumin within the synthesized CCPHNFs. As shown in Figure 11. b-c, the bright-field image revealed the aggregated morphology of the CCPHNFs particles, while the corresponding fluorescence image exhibited a distinct green fluorescence distributed throughout the sample. The observed fluorescence is attributed to the intrinsic fluorescent properties of curcumin, indicating that curcumin was present in the synthesized CCPHNFs and retained its fluorescent properties after synthesis. This observation is consistent with the presence of curcumin within the CCPHNFs, while its incorporation and interactions with the copper phosphate matrix are further supported by the FTIR analysis discussed below. The presence of curcumin may contribute to the antibacterial properties of the CCPHNFs through its intrinsic bioactivity

a)

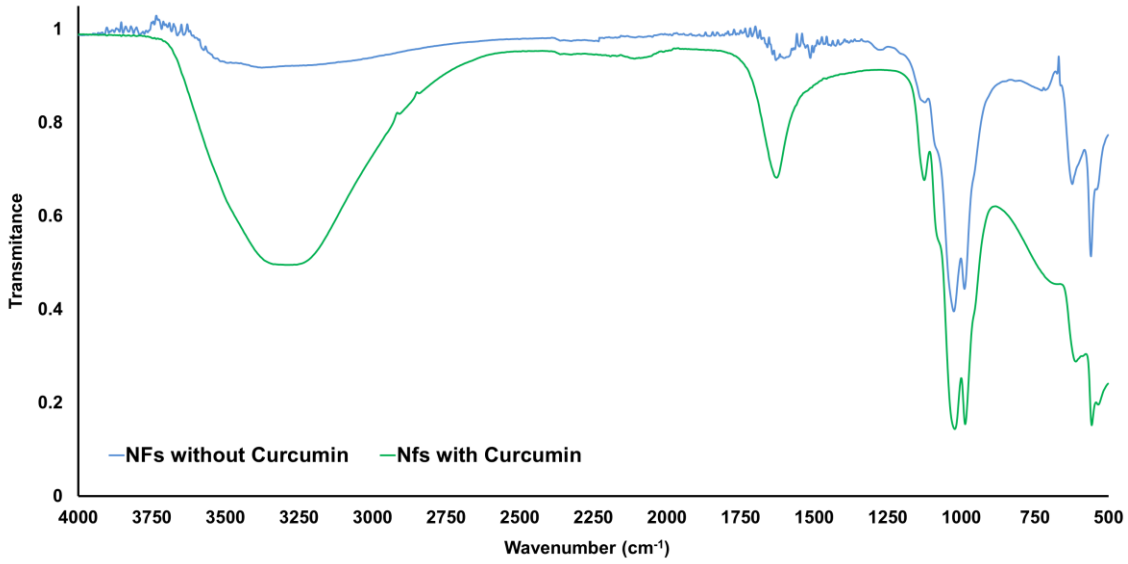

b)

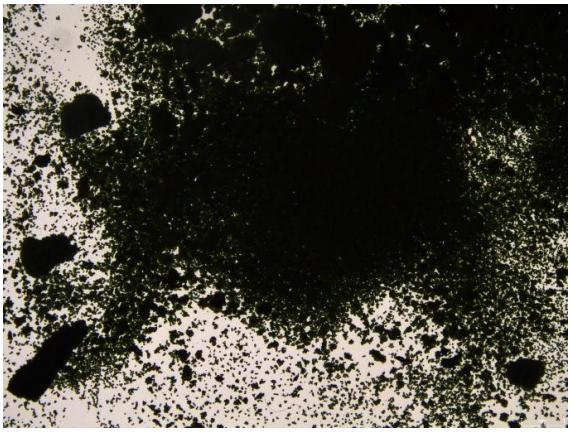

c)

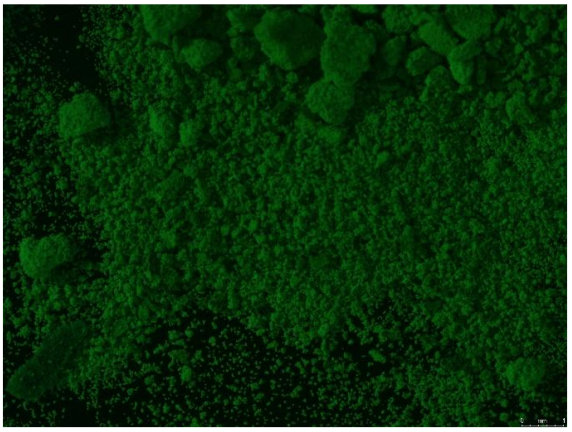

Figure 11-a) FTIR spectra of nanoflowers synthesized with and without curcumin. (b) Bright-field optical microscopy image of the synthesized nanoflowers. (c) Fluorescence microscopy image showing the green fluorescence emitted by curcumin.

2.3.2 Characterization of Biochar-Supported Nanoflowers (BC-NFs)

2.3.2.1 Morphological Analysis (SEM)

The morphology of the BC–NFs composite synthesized using 0.2 g biochar, 100 mM $CuSO_4$, and 0.5 µM curcumin was investigated using SEM (Figure 12). At low magnification

(Figure 12a), the biochar exhibited an irregular three-dimensional structure with interconnected channels and cavities of different sizes. Following the in situ synthesis, numerous flower-like structures were observed distributed over the biochar surface. The presence of these structures across different regions of the biochar indicates that CCPHNFs formed directly on the biochar substrate during the synthesis process.

The CCPHNFs were predominantly observed on the external surfaces of the biochar, while a smaller number of structures were also visible within the larger pores and cavities (Figure 12b–e). Therefore, the SEM images suggest that CCPHNF formation occurred mainly at the exposed biochar surfaces rather than throughout the internal pore network. The presence of nanoflowers at different locations on the biochar suggests that the surface provided sites for heterogeneous nucleation, where interactions between the biochar surface and the Cu^{2+}/phosphate/curcumin precursors may have promoted the initial formation of CCPHNF nuclei.

Higher-magnification images (Figure 12c–e) clearly show the hierarchical morphology of the CCPHNFs, consisting of interconnected nanosheet- or petal-like features assembled into flower-like structures. These structures appear smaller than the CCPHNFs synthesized without biochar under the corresponding conditions (Figure 12g). The reduced size of the biochar-supported nanoflowers is likely associated with heterogeneous nucleation on the biochar surface. The availability of additional nucleation sites may promote the formation of a greater number of nuclei, thereby distributing the available precursor species among more growing structures and limiting the growth of individual nanoflowers. This interpretation is consistent with the observed smaller and more dispersed flower-like structures on the biochar surface.

At the highest magnification (Figure 12f), the porous architecture of the biochar is clearly visible, including interconnected cavities and channels. The retention of these structural features

after CCPHNF formation indicates that the overall porous framework of the biochar was preserved during the synthesis process. The resulting composite therefore combines the microporous structure of the biochar with the hierarchical surface morphology of the CCPHNFs, producing a multiscale surface architecture.

The observed hierarchical and porous features may provide accessible surface areas for interactions with microorganisms and may facilitate mass transfer within the composite. These characteristics could contribute to the antibacterial performance observed for BC–NFs. However, SEM morphology alone does not establish the strength of CCPHNF attachment, the exact amount of CCPHNF loading, or the reusability of the composite2.3.2.2 Elemental Composition and Elemental Mapping Analysis

The elemental composition and distribution of the BC-NFs composite were investigated by EDS and elemental mapping (Figure 12. g-h). The EDS analysis showed that carbon (C) was the predominant element in the BC-NFs composite, accounting for approximately 70 wt.%, followed by oxygen (O) at approximately 15 wt.%. Copper (Cu), associated with the copper phosphate nanoflowers, represented approximately 7 wt.%, while phosphorus (P) was detected at approximately 1 wt.%. Minor amounts of chlorine (Cl), calcium (Ca), potassium (K), sulfur (S), and iron (Fe) were also detected, each contributing approximately ≤1 wt.%. The presence of Cu and P, together with their spatial association with the flower-like structures in the elemental maps, supports the incorporation of CCPHNFs into the biochar matrix. The EDS spectrum further verified the presence of C, O, Cu, and P, while the detected tungsten (W) peak originated from the conductive coating applied during SEM sample preparation and is not part of the composite

composition. These results confirm the successful synthesis of the BC–NF composite and the homogeneous distribution of the CCPHNFs on the porous biochar support.

2.3.2.3 Fluorescence Microscopy

As illustrated in Figure 12. i-j, Fluorescence microscopy was employed to verify the incorporation of curcumin-containing CCPHNFs within the biochar matrix. Curcumin is a naturally fluorescent molecule and therefore serves as an indicator of successful CCPHNF immobilization.

As shown in Figure 12, localized fluorescent regions were observed on the BC-NFs surface. These fluorescent domains were absent in pristine biochar and correspond to regions where curcumin-containing CCPHNFs were attached. The fluorescence signal confirms that curcumin remained associated with the CCPHNF structures following synthesis and washing procedures.

The observed fluorescence further supports the successful formation of a BC-NFs composite and provides additional evidence for the immobilization of CCPHNFs onto the biochar surface.

a)

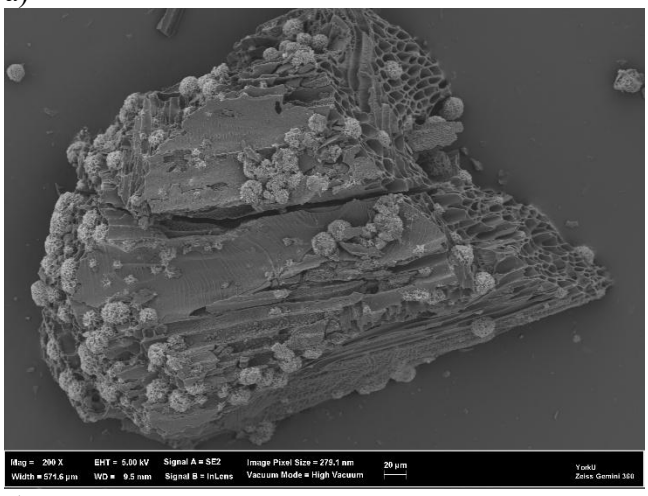

b)

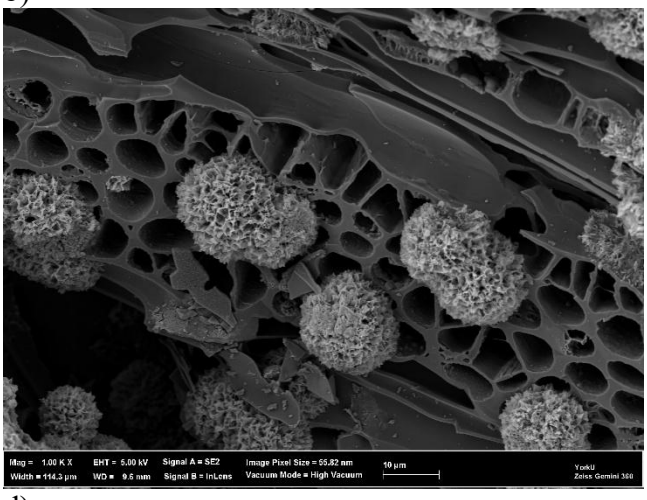

c)

d)

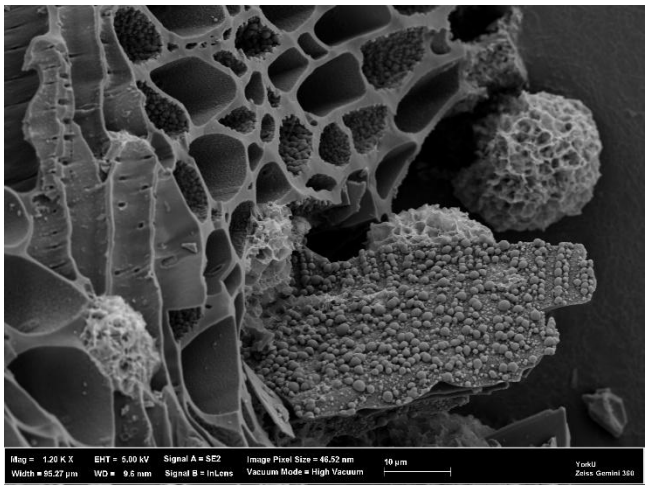
Mag = 1.20 K X
EHT = 5.00 kV
Signal A = SE2
Image Pixel Size = 46.52 nm
10 µm
Width = 95.27 µm
WD = 9.5 mm
Signal B = InLens
Vacuum Mode = High Vacuum
YorkU
Zeiss Gemini 360

e)


Mag = 2.80 K X
EHT = 5.00 kV
Signal A = SE2
Image Pixel Size = 19.94 nm
1 µm
Width = 40.83 µm
WD = 9.5 mm
Signal B = InLens
Vacuum Mode = High Vacuum
YorkU
Zeiss Gemini 360

f)

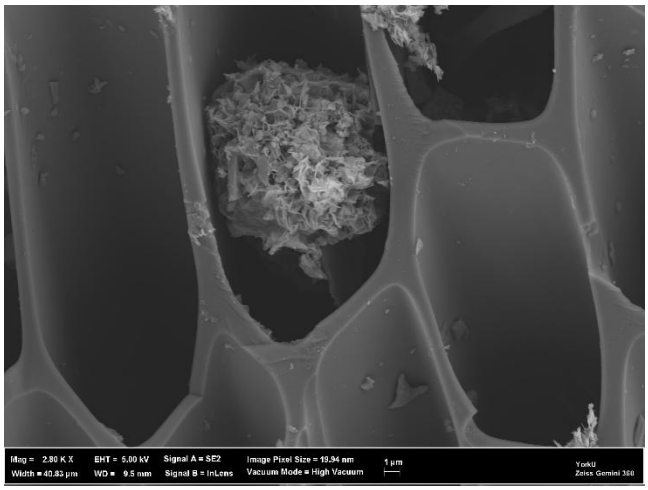
Mag = 2.80 K X
EHT = 5.00 kV
Signal A = SE2
Image Pixel Size = 19.94 nm
1 µm
Width = 40.83 µm
WD = 9.5 mm
Signal B = InLens
Vacuum Mode = High Vacuum
YorkU
Zeiss Gemini 360

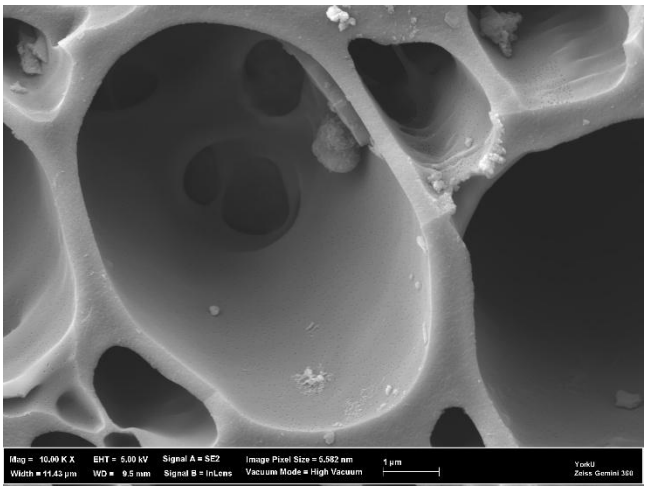
Mag = 10.00 K X
EHT = 5.00 kV
Signal A = SE2
Image Pixel Size = 5.582 nm
1 µm
Width = 11.43 µm
WD = 9.5 mm
Signal B = InLens
Vacuum Mode = High Vacuum
YorkU
Zeiss Gemini 360

g)

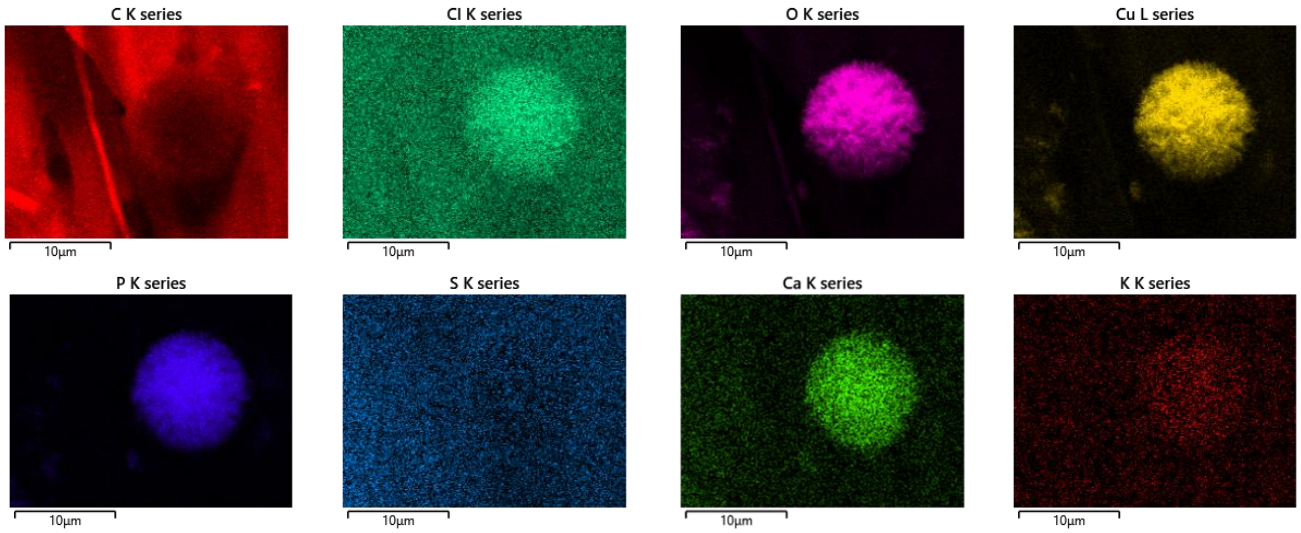
C K series
Cl K series
O K series
Cu L series
P K series
S K series
Ca K series
K K series
10µm

h)

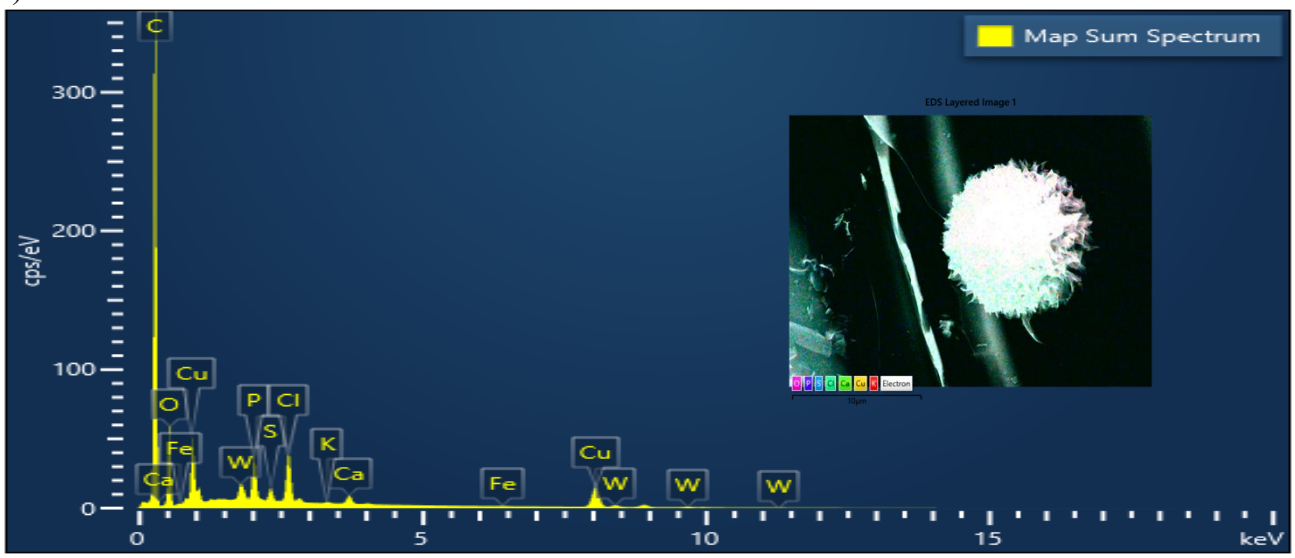
Map Sum Spectrum
EDS Layered Image 1
cps/eV
300
200
100
0
C
O
Cu
Fe
Ca
W
P
Cl
S
K
Ca
Fe
Cu
W
W
W
0
5
10
15
keV

i)

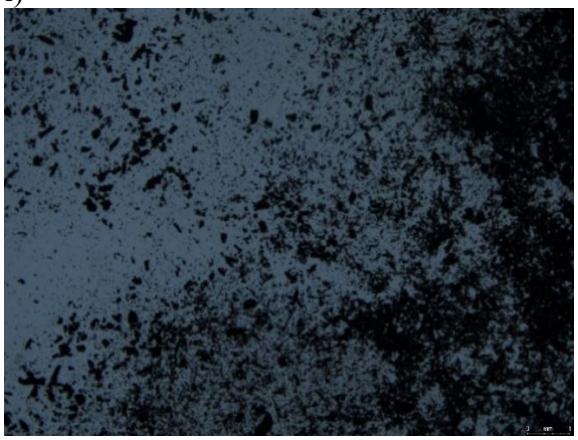

j)

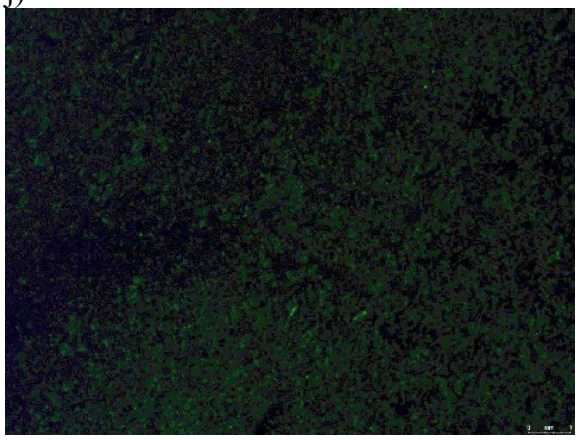

Figure 12- *SEM images of the BC-NFs composite at different magnifications, demonstrating the successful incorporation and distribution of hierarchical copper phosphate nanoflowers on the porous biochar surface. (a) 200×, (b) 1,000×, (c) 1,200×, (d) 2,800×, (e) 2,800×, and (f) 10,000×. (g) Elemental mapping obtained by EDS analysis illustrating the distribution of C, Cl, O, Cu, P, S, Ca, and K within the BC-NFs composite. (h) Corresponding EDS spectrum. (i) Bright-field optical microscopy image, scale bar: 1 mm, and (j) fluorescence microscopy image through characteristic green fluorescence. Scale bars: 1 mm.*

2.3.2.4 Functional Group Analysis (FTIR)

FTIR spectroscopy was used to evaluate changes in surface chemistry following CCPHNFs deposition onto the biochar substrate. Figure 5 compares the FTIR spectra of pristine biochar and the BC-NFs composite (Table 5 and Fig 13).

The spectrum of pristine biochar exhibited a broad absorption band around 3200–3600 cm^{-1} corresponding to O–H stretching vibrations from hydroxyl groups. Additional bands observed near 1600 cm^{-1} were attributed to aromatic C=C vibrations and carbonyl-containing functional groups commonly present in biochar.

Following CCPHNFs deposition, new absorption bands appeared in the region between approximately 500 and 1200 cm^{-1}. These bands correspond to Cu–O, P–O, and P–O–Cu vibrations characteristic of copper phosphate structures. The appearance of these peaks confirms the successful attachment of CCPHNFs onto the biochar surface.

Furthermore, slight changes in the intensity of O–H and aromatic bands suggest interactions between biochar functional groups and the deposited CCPHNFs. These interactions likely contribute to the stability of the BC-NFs composite and facilitate CCPHNF immobilization.

Table 5. Characteristic FTIR absorption bands of pristine biochar and the BC-NFs composite.

Peak Position (cm^{-1})	Functional Group / Vibration	Attribution
3200–3600	O–H stretching	Hydroxyl groups and adsorbed water on the biochar surface

~1600	Aromatic C=C stretching / C=O vibration	Aromatic carbon framework and oxygen-containing functional groups of biochar
1100–1030	ν_3(P–O) asymmetric stretching	Phosphate groups of copper phosphate nanoflowers
990–960	P–O–Cu stretching	Copper phosphate framework
620–560	O–P–O bending	Phosphate groups in copper phosphate
560–500	Cu–O vibration	Cu–O bonds confirming successful immobilization of CCPHNFs on biochar

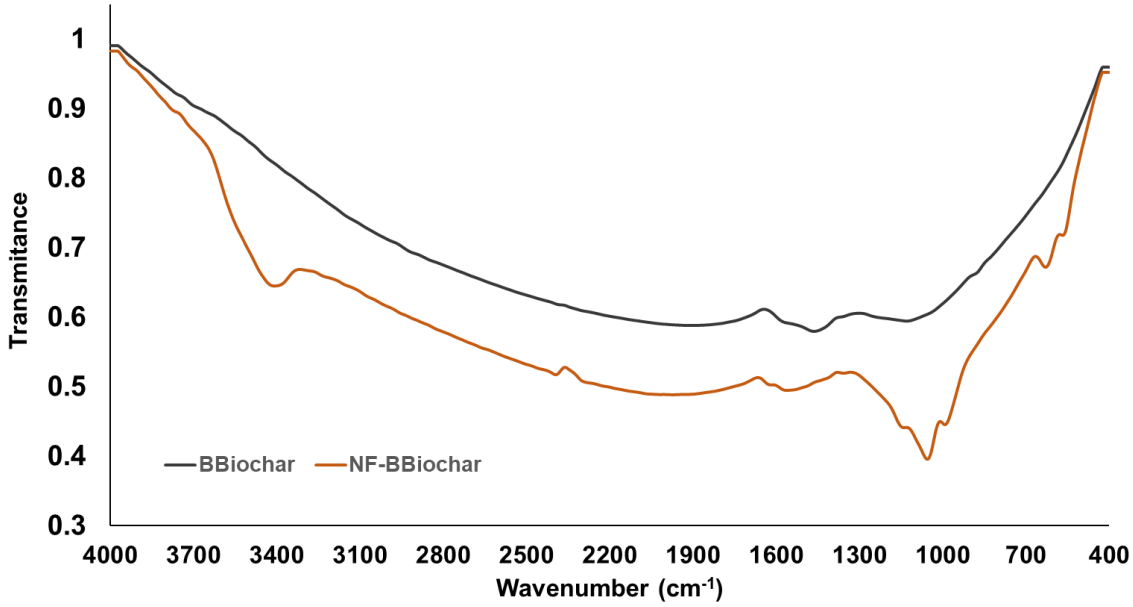

Figure 13. FTIR spectra of pristine biochar and the BC-NFs composite.

2.3.2.5 Surface Area and Porosity Analysis (BET)

The textural properties of pristine biochar (BC), CCPHNFs, and the BC-NFs composite were evaluated using nitrogen adsorption–desorption analysis. The BET surface area and pore characteristics are summarized in Table 6. Pristine BC exhibited a high specific surface area of 377.1 $m^2\ g^{-1}$, consistent with its highly porous structure. In comparison, CCPHNFs exhibited a substantially lower BET surface area of 44.9 $m^2\ g^{-1}$.

Following incorporation of CCPHNFs, the BET surface area of the BC-NFs composite decreased to 218.8 $m^2\ g^{-1}$. This reduction should primarily be considered in relation to the substantially lower surface area of the CCPHNF phase. Because BET surface area is normalized to the total mass of

the composite, incorporation of a lower-surface-area material into high-surface-area biochar can decrease the measured surface area of the resulting composite even when the overall porous structure is retained. Using an idealized weighted-average mixing relationship between pristine BC and CCPHNFs, the measured surface area of the BC-NFs composite corresponds to an apparent CCPHNF fraction of approximately 48 wt.%. This value should be regarded only as an approximate estimate because the surface areas of the individual components may not remain fully additive after composite formation.

The reduction in BET surface area may also be partly associated with coverage of biochar surfaces or partial occupation of accessible pores by deposited CCPHNFs. The formation and growth of CCPHNFs on the biochar surface may cover high-surface-area carbon regions and restrict access to some pore entrances. In addition, potential crystal growth within or near accessible pores could further reduce the surface area available for nitrogen adsorption. However, the close agreement between the experimentally measured composite surface area and the value predicted by the simple mixing relationship suggests that the decrease in surface area can largely be explained by the contribution of the lower-surface-area CCPHNF phase rather than being attributed solely to extensive pore blockage. Thus, surface coverage and possible pore occupation likely contribute to the observed reduction, but extensive pore blockage does not appear to be the dominant factor based on the BET results.

The calculated DA pore radius was 11.5 Å for BC and 11.3 Å for the BC-NFs composite, indicating that the characteristic pore dimension obtained from the adsorption analysis remained relatively similar after CCPHNF incorporation. In contrast, the 13.9 Å value obtained for CCPHNF should not be interpreted directly as the physical pore size of the nanoflower structures, as the calculated pore radius represents a model-dependent textural parameter derived from gas adsorption data.

Therefore, the pore-radius results primarily indicate that the characteristic pore structure of the biochar was not substantially altered following CCPHNF incorporation.

Table 6. BET surface area and pore characteristics of pristine BC, CCPHNF, and BC-NFs.

Specimen	Multipoint BET Surface Area (m^2/g)	Single Point BET Surface Area (m^2/g)	DFT Surface Area	DA Pore Radius (Å)
BC	377.1	376.1	370	11.5
CCPHNF	44.9	41	38.3	13.9
BC-NFs	218.8	213.7	212.8	11.3

The BET results demonstrate that the BC-NFs composite retained a substantial fraction of the high surface area of pristine biochar while incorporating the functional CCPHNF phase. The resulting composite therefore combines the porous structure of biochar with the surface functionality of CCPHNFs, providing an accessible surface for subsequent interactions with target contaminants and microorganisms.

In practice, the specific surface areas of biochar and CCPHNs may not remain independently accessible after composite formation. Surface coverage, pore occupation, aggregation, changes in pore accessibility, and interactions between the two phases can cause deviations from ideal additive behavior. Consequently, the calculated value should be interpreted as an estimate of the effective CCPHNFs contribution rather than an exact gravimetric loading. Direct determination of the loading could be further confirmed using complementary techniques such as thermogravimetric analysis (TGA), ICP-OES/AAS determination of copper content, or quantitative mass-balance analysis.

Despite this uncertainty, the estimated high CCPHNFs fraction, together with the SEM observations and the appearance of characteristic copper phosphate features in FTIR/XRD

analyses, provides complementary evidence that substantial nanoflower growth occurred on the biochar support. Therefore, the theoretical loading estimate supports three aspects of composite formation: substantial deposition of the CCPHNF phase, successful growth of CCPHNs during the in situ synthesis, and modification of the accessible biochar surface through nanoflower coverage.

2.3.3 Antibacterial Activity Against Escherichia coli

The antibacterial activity of the BC-NFs and CCPHNFs against Escherichia coli was evaluated using the agar well diffusion method. A 20 μL aliquot of the bacterial suspension was adjusted to an optical density (OD_{600}) of approximately 0.8–0.9, corresponding to an estimated bacterial concentration of 6.4–7.2 × 10^8 cells mL^{-1}. After incubation at 30 °C for 24 h, clear inhibition zones were observed around the wells containing BC-NFs and CCPHNFs (Figure 14).

As summarized in Table 6, the BC-NFs composite produced inhibition zones of 2.79 ± 0.07 mm and 3.54 ± 0.05 mm at concentrations of 100 and 200 mg mL^{-1}, respectively, indicating concentration-dependent antibacterial activity against E. coli. Similarly, CCPHNFs exhibited inhibition zones of 1.49 ± 0.16 mm and 2.61 ± 0.37 mm at 100 and 200 mg mL^{-1}, respectively, confirming that both materials possess antibacterial activity. However, the BC-NFs composite consistently produced larger inhibition zones than the corresponding CCPHNFs, suggesting that the biochar support enhanced the antibacterial performance of the nanoflowers.

Table 7. Antibacterial activity of BC-NFs and CCPHNFs against Escherichia coli determined by the agar well diffusion method.

Sample	Concentration	Inhibition Zone (mm)
BC-NFs-1	100 mg/mL	2.79 ±0.07
BC-NFs-2	200 mg/ml	3.54±0.05

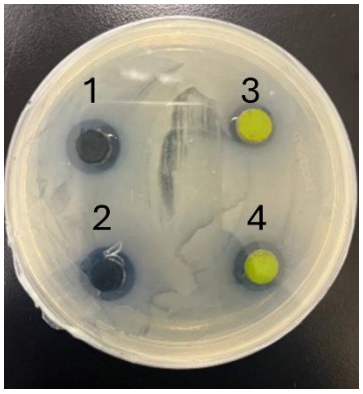

CCPHNFs-3	100 mg/mL	1.49±0.16
CCPHNFs-4	200 mg/ml	2.61±0.37

Figure 14- Antibacterial activity of BC-NFs and CCPHNFs against Escherichia coli was evaluated by the agar well diffusion method at concentrations of 100 and 200 mg mL^{-1} after incubation at 30 °C for 24 h

The antibacterial performance of the BC-NFs composite was further compared with ciprofloxacin (CIP) as a positive control and deionized (DI) water as a negative control. For this experiment, a 15 µL aliquot of the E. coli suspension (OD_{600} = 0.8–0.9; approximately 6.4–7.2 × 10^8 cells mL^{-1}) was uniformly spread onto the agar surface. After incubation at 30 °C for 24 h, a distinct inhibition zone was observed around the BC-NFs and ciprofloxacin wells, whereas no inhibition zone was detected around the DI water control (Figure 15).

As summarized in Table 8, the BC-NFs composite (100 mg mL^{-1}) produced an inhibition zone of 29.2 ± 0.6 mm, demonstrating significant antibacterial activity against E. coli. In comparison, ciprofloxacin (10 mg mL^{-1}) exhibited a substantially larger inhibition zone of 71.2 ± 3.3 mm, reflecting its strong antibacterial efficacy. No inhibition zone was observed for the DI water control, confirming that the solvent had no inhibitory effect on bacterial growth.

Table 8. Antibacterial activity of BC-NFs against Escherichia coli determined by the agar well diffusion method.

Sample	**Concentration**	**Inhibition Zone (mm)**
DI Water	—	0

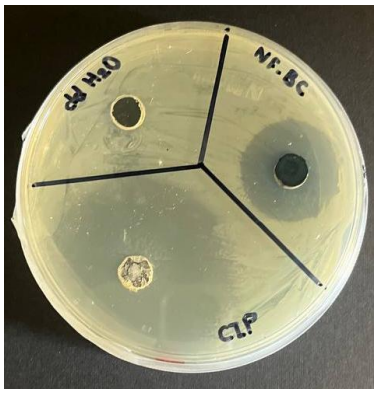

BC-NFs	100 mg/mL	29.2±0.6
Ciprofloxacin	10 mg/mL	71.2±3.3

Figure 15- Antibacterial activity of the BC-NFs composite against Escherichia coli evaluated by the agar well diffusion method. The agar plate shows the inhibition zones produced by BC-NFs, ciprofloxacin (positive control), and deionized (DI) water (negative control) after incubation at 30 °C for 72 h.

To further assess the contribution of the individual components, additional agar well diffusion experiments were conducted using curcumin and copper phosphate. A 15 µL aliquot of the *E. coli* suspension, adjusted to an OD_{600} of approximately 0.8–0.9, corresponding to an estimated bacterial concentration of 6.4–7.2 × 10^8 cells mL^{-1}, was spread onto the agar surface. Curcumin at 10 mg mL^{-1} did not produce a measurable inhibition zone, whereas copper phosphate at 100 mg mL^{-1} produced an inhibition zone of 10.65 ± 0.20 mm. These results indicate that copper phosphate exhibited measurable antibacterial activity under the tested conditions, while no detectable inhibition was observed for curcumin alone.

The observed antibacterial activity of BC-NFs and CCPHNFs is consistent with the contribution of the copper phosphate nanoflower component, while the absence of a measurable inhibition zone for curcumin alone suggests that curcumin at the tested concentration did not produce detectable activity under the agar diffusion conditions used here. The larger inhibition zones observed for BC-NFs compared with CCPHNFs may be associated with differences in the physical structure and dispersion of the materials, which could influence their interaction with bacterial cells and their behavior within the agar matrix. However, these effects cannot be established solely from

agar well diffusion measurements. In addition, because the BC-NFs composite contains only a fraction of CCPHNFs, comparison at the same total material concentration does not represent an equivalent amount of the active nanoflower component. Therefore, the observed difference should be interpreted as a difference in apparent antibacterial activity rather than definitive evidence of synergistic enhancement by biochar.

It is also important to consider that agar well diffusion is influenced by the ability of a material to diffuse through the agar matrix. Nanomaterials and particulate composites may exhibit limited diffusion, meaning that inhibition-zone diameter may not directly reflect their intrinsic antibacterial potency.

Overall, the results demonstrate measurable antibacterial activity for the copper phosphate-based materials, CCPHNFs, and BC-NFs against *E. coli* under the tested agar diffusion conditions. The BC-NFs composite produced clear inhibition zones and therefore demonstrates potential as an antimicrobial material for environmental and water-treatment applications.

2.3.4. Environmental relevance and potential application

The combination of a porous BC support with CCPHNFs provides a multifunctional material architecture with potential relevance to environmental applications. Biochar contributes a porous and carbon-rich framework that can serve as a support for the formation and distribution of CCPHNs, while the copper phosphate–curcumin phase introduces additional surface functionality and antibacterial properties. The integration of these components therefore combines the structural characteristics of biochar with the functional properties of the hybrid nanoflowers within a single composite material.

From a water-treatment perspective, this combination is particularly relevant because microbial contamination can be an important consideration alongside the removal of chemical contaminants. The porous biochar framework may provide accessible surfaces for interaction with contaminants, while the antibacterial CCPHN phase may provide an additional function for microbial control. The hierarchical structure observed by SEM, consisting of porous biochar decorated with interconnected nanoflower structures, may further provide a heterogeneous surface with multiple sites for interactions between the material and the surrounding aqueous environment. Biochar-supported metal nanomaterials have been investigated for environmental applications because the porous carbon matrix can help disperse and stabilize the supported active phase and reduce aggregation. This type of support can therefore be advantageous when developing multifunctional materials in which the active nanophase needs to remain distributed throughout a porous matrix.

The antibacterial properties observed in this study further support the potential use of BC–NFs in antimicrobial water-treatment materials. The BC–NFs composite demonstrated measurable antibacterial activity against *E. coli*, indicating that the material can provide microbial inhibition in addition to its structural and surface functionalities. This is particularly relevant for the development of biochar-based filtration media, where an antimicrobial function could complement contaminant removal. The composite could potentially be incorporated into packed-bed filtration media, porous treatment materials, or used as an antimicrobial component in membrane-based water-treatment systems. However, these applications remain prospective because the present study did not evaluate BC–NFs under continuous-flow or membrane-filtration conditions.

Another potential advantage of the composite architecture is the possibility of tailoring its properties for different environmental applications. The biochar support provides a relatively low-cost carbonaceous matrix, while the morphology and composition of the nanoflower phase can be

modified through synthesis conditions. In the present work, curcumin played an important role in the formation of the hybrid nanoflower structure, while incorporation onto biochar produced a composite with both porous carbon and hierarchical inorganic–organic features. Such tunability may be useful for designing multifunctional materials in which adsorption and antimicrobial functions are combined rather than relying on a single treatment mechanism.

Nevertheless, several factors must be evaluated before practical environmental implementation. In particular, the stability of the CCPHNFs phase under aqueous conditions, possible release of copper species or other components, long-term antibacterial performance, and regeneration or reusability of the composite should be investigated. In addition, agar well diffusion provides a qualitative or comparative assessment of antibacterial activity but does not directly represent bacterial removal or inactivation in a water-treatment system. Therefore, future studies should evaluate bacterial reduction using CFU or other quantitative viability measurements, continuous-flow filtration performance, material stability, copper leaching, regeneration/reusability, and performance in real water matrices. These experiments would establish whether the observed laboratory-scale antibacterial properties can be translated into practical water-treatment performance.

Overall, the BC–NFs composite demonstrates a combination of porous biochar structure, hierarchical copper phosphate–curcumin nanoflowers, and antibacterial activity, making it a potentially useful platform for multifunctional environmental materials. While the present results establish the material's structural characteristics and antibacterial response, further application-oriented studies are required to determine its effectiveness, stability, and safety in realistic water-treatment systems.

2.4. Conclusion

In this study, BC–NFs were successfully synthesized through a simple biomimetic self-assembly approach. The effect of $CuSO_4$ concentration on CCPHNF formation was investigated, and 100 mM $CuSO_4$ produced well-defined hierarchical flower-like structures with interconnected petal-like nanosheets. SEM, EDS, XRD, FTIR, fluorescence microscopy, and BET analyses provided complementary evidence for the formation of CCPHNs, the presence of curcumin, and their deposition on the porous biochar support. The estimated CCPHNF contribution based on the BET mixing calculation was approximately 48 wt.%, although this value represents an apparent loading estimate and is subject to uncertainty associated with changes in pore accessibility and surface-area additivity after composite formation.

Following nanoflower deposition, the BC–NFs composite exhibited a BET surface area of 218.8 $m^2\ g^{-1}$, demonstrating that substantial accessible surface area was retained after composite formation. The BC–NFs composite also exhibited measurable antibacterial activity against *E. coli*, producing an inhibition zone of 29.2 ± 0.6 mm at the tested concentration, whereas the deionized water control showed no inhibition. Copper phosphate also exhibited measurable antibacterial activity (10.65 ± 0.20 mm), while curcumin alone produced no detectable inhibition under the tested conditions. These results demonstrate that the synthesized composite possesses measurable antibacterial activity; however, the individual contributions of biochar, curcumin, and copper phosphate and any potential synergistic interactions were not quantitatively established in this study.

Overall, the results demonstrate the successful synthesis and characterization of a biochar-supported curcumin-copper phosphate nanoflower composite with measurable antibacterial activity. The combination of a porous biochar framework and antibacterial CCPHN phase makes

the material of potential interest for environmental and water-treatment applications. However, further studies are required to establish the underlying antibacterial mechanisms and practical performance, including evaluation of Cu^{2+}/metal leaching, bacterial viability and CFU reduction, MIC, long-term stability, reusability, cytotoxicity, and activity against a broader range of microorganisms. Future work should also investigate the performance of BC–NFs in continuous-flow filtration and membrane-based water-treatment systems to determine its suitability for practical environmental applications.

Chapter 3: Eggshell-Superabsorbent Polymer Composite for Chloride Mitigation in Road Salt-Impacted Freshwater

Sama Khalili Moradkhanloo, Ratul Kumar Das, Siu-Ning Leung, Satinder Kaur Brar
(to be submitted)

3.1 Introduction

Urban freshwater systems are increasingly impacted by nutrient pollution and road salt contamination. Chloride, primarily introduced through de-icing salts, is particularly challenging to remove because it is highly soluble, chemically stable, and persists in aquatic environments without natural degradation. Conventional treatment technologies, including reverse osmosis, electrodialysis, and ion exchange, can effectively remove chloride but are often costly and energy-intensive, limiting their widespread implementation. Consequently, there is an increasing need for sustainable, low-cost, and environmentally friendly approaches for chloride mitigation to protect freshwater ecosystems from long-term salinization. (Foller et al., 2023; Khor et al., 2024; Y. Li et al., 2022; A. Wei et al., 2023). Despite Canada's implementation of road salt management practices, chloride contamination remains a significant environmental challenge due to the persistence of chloride in aquatic systems, highlighting the need for effective chloride removal technologies.(Environment and Climate Change Canada. Code of Practice for the Environmental

Management of Road Salts: Annual Overview of Data Reported (2019–2024) in the Context of National Targets. Gatineau, QC, Canada; 2025., n.d.; Hintz & Relyea, 2019)

Water scarcity and the increasing demand for efficient water management technologies have driven research toward advanced functional materials capable of interacting with aqueous systems. Among these materials, superabsorbent polymers (SAPs) have emerged as promising hydrophilic materials because of their exceptional ability to absorb and retain large quantities of water within a three-dimensional cross-linked network (Q. Wang et al., 2026). Their swelling behavior is governed by osmotic pressure and polymer network expansion and is influenced by factors such as ionic strength, temperature, and polymer composition (Jin et al., n.d.). Owing to their high swelling capacity, porous structure, and abundant functional groups, SAPs have attracted increasing attention as sustainable materials for water and wastewater treatment. They have been widely investigated for the removal of heavy metals, dyes, and other hazardous pollutants and can be readily functionalized with natural polymers or inorganic materials to enhance adsorption capacity, selectivity, mechanical stability, and reusability (Ahmed, 2015; Batara et al., 2025). In addition, SAPs regulate moisture and mass transfer by reversibly absorbing and releasing water (Y. Yu et al., 2026). Recent studies have shown that dissolved salts strongly influence SAP swelling behavior through osmotic and ionic interactions, creating opportunities for controlled ion transport and precipitation within the polymer matrix. Despite these advantages, the application of SAPs for chloride removal from road salt-impacted freshwater remains largely unexplored (Jin et al., n.d.). Hydrogels remove contaminants through multiple mechanisms, including electrostatic interactions, ion exchange, hydrogen bonding, and diffusion within their interconnected porous networks, while their swelling behavior regulates ion transport and local mass transfer. Their three-dimensional structure provides a confined aqueous microenvironment in which dissolved ions can

become concentrated, facilitating localized chemical reactions when reactive components are incorporated into the polymer matrix. Although these mechanisms have been extensively exploited for the removal of heavy metals, dyes, and other ionic contaminants, their application to chloride sequestration has received very limited attention, particularly in calcium-containing hydrogel composites.(R. Zhou et al., 2025)

In recent years, bio-derived waste materials have attracted increasing attention as sustainable functional additives for environmental applications. Among them, EGS is particularly attractive because of its abundance, low cost, and high calcium carbonate content (approximately 94%), making it a naturally reactive calcium source. Processing EGS into fine particles increases its surface area and chemical reactivity, expanding its applicability in environmental systems (Mijan et al., 2014). The hierarchical calcite-based structure of EGS further contributes to its functional properties (Adimas, 2026; T. Li et al., 2024). Owing to its high calcium content, EGS has demonstrated significant potential in adsorption and water treatment applications by promoting ion binding and precipitation reactions. In particular, EGS-derived calcium has been successfully used to functionalize biochar, significantly enhancing phosphate adsorption through calcium-based active sites. In addition to improving treatment performance, the utilization of EGS supports waste valorization by converting food waste into a low-cost, sustainable functional material (Chandrappa & Kamath, 2021; Kang et al., 2010; X. Liu & Yue, 2024; Manikandan et al., 2021). These characteristics make EGS an attractive additive for integration into SAP systems because it provides a sustainable source of calcium capable of promoting localized calcium-assisted reactions within the swollen hydrogel. Rather than relying on direct chloride adsorption, the hydrogel network serves as a reaction medium that concentrates dissolved ions, enabling calcium-mediated immobilization of chloride under favorable conditions. (Ansari et al., 2025; J. Yin et al., 2023).

Although Polyacrylamide-based (PAM)-based SAPs have demonstrated excellent swelling capacity and water retention, they may undergo gradual degradation under prolonged environmental exposure. Nevertheless, their low residual monomer content and proven performance have enabled widespread application in water and wastewater treatment. Incorporating calcium-rich EGS into SAP matrices further enhances treatment performance through adsorption, ion exchange, and precipitation mechanisms, making SAP–EGS composites promising and sustainable materials for water treatment applications (Mohammadzadeh Pakdel & Peighambardoust, 2018; Xiong et al., 2018).

Integrating SAP with EGS presents a promising strategy for developing multifunctional composite systems that combine controlled water retention with calcium-assisted ion removal. Although SAPs have been widely investigated as adsorbents for wastewater treatment, and calcium-rich materials have been extensively employed for the removal of contaminants such as phosphate and heavy metals, their combined application for chloride control has received little attention. Existing hydrogel studies have primarily focused on adsorption through electrostatic interactions, ion exchange, chelation, and hydrogen bonding, whereas chloride removal using calcium-containing SAP composites has rarely been explored.

This study presents a novel and sustainable approach for chloride mitigation by developing a SAP–EGS composite that combines controlled water absorption with calcium-assisted chloride removal. Unlike conventional SAP-based adsorbents, which have mainly been applied for heavy metal and organic pollutant removal, the proposed composite exploits the confined aqueous environment of the swollen hydrogel to facilitate chloride capture. Chloride removal may involve a calcium-assisted mechanism, in addition to water absorption and ion concentration. However, the proposed mechanism has not been directly confirmed and warrants further investigation

through techniques such as X-ray diffraction (XRD), ion balance analysis, thermodynamic evaluation, and precipitate characterization. Furthermore, the use of waste EGSs as a reactive calcium source promotes resource recovery and circular economy practices while providing a low-cost alternative for treating road salt-contaminated freshwater. To the best of our knowledge, this is the first study to demonstrate the integration of SAP and waste EGS for chloride removal from a freshwater system.

3.2 Experimental Materials and Methods

3.2.1 Materials

Acrylamide (AM), acrylic acid (AA), N,N′-methylenebisacrylamide (MBA), ammonium persulfate (APS), methanol (MeOH), and Calcium carbonate ($CaCO_3$) were purchased from Sigma-Aldrich and used without further purification. Deionized water was used throughout all experiments. Waste EGSs were collected from commercially available chicken eggs purchased from local grocery stores in Ontario, Canada. The EGSs were washed thoroughly with deionized water to remove residual membranes and impurities, dried, ground into a fine powder, and sieved to obtain particles smaller than 75 μm (ASTM) before use as a calcium source.

Water samples were collected from Swan Lake, Markham, Ontario, at two representative locations: the dock area (Point 1) and the bridge area (Point 2). Based on the lake monitoring report and accessibility, these locations were selected to represent different hydrodynamic zones of the lake. Water samples were collected at a depth of 0.5 and 1.5 m and stored in clean containers for chloride analysis and adsorption experiments. Initial chloride concentrations were measured using a HACH DR3900 spectrophotometer with TNT879 chloride reagent kits (1–1000 mg/L Cl^-). The measured chloride concentrations of Swan Lake water were approximately 206–264 mg/L,

confirming elevated chloride contamination compared with the Canadian long-term environmental guideline of 120 mg/L. The lake water exhibited a pH ranging from 7.9 to 9.5, with total nitrogen concentrations averaging approximately 0.6 mg L^{-1} during the growing season, while ammonia and nitrate concentrations were generally very low and total phosphorus concentrations below 20 µg L^{-1}.

3.2.2 Synthesis of SAP-EGS Composite

The SAP-EGS composite hydrogel was synthesized via free radical polymerization. Initially, 0.6 g of AM and 0.6 g of AA were dissolved in deionized water under continuous stirring at 1500 rpm. Subsequently, 0.24 g of prepared EGS powder was added to the monomer solution and mixed to ensure uniform dispersion. A total of 0.12 g of NMBA was then introduced as a cross-linking agent. After complete mixing, 0.006 g of APS was added as the radical initiator. The polymerization reaction was carried out under a nitrogen atmosphere at 70 °C with continuous stirring at 1500 rpm for 3 hours. The synthesized SAP–EGS hydrogel was washed with ethanol to remove residual monomers and dried at 40 °C to constant weight. The dry mass recovery ranged from 1.48 to 1.55 g, with an average of 1.52 ± 0.02 g (n = 10). Based on the theoretical solid mass of 1.566 g the corresponding hydrogel synthesis yield, dry mass recovery, and apparent polymerization efficiency were 97.1 ± 1.3%. The resulting product was a crosslinked SAP-EGS hydrogel. To optimize the hydrogel formulation, the effects of EGS loading and monomer ratio on chloride removal performance were investigated. EGS concentrations of 0.12, 0.18, 0.24, 0.30, 0.36, and 0.48 g were evaluated. In addition, AA to AM ratios of 1:2, 1:1, and 2:1 was investigated while maintaining the total monomer content constant.(Tabesh, Zabihihesari, et al., 2025)

3.2.3 Physicochemical characterization of SAP-EGS Hydrogel

Fourier Transform Infrared Spectroscopy (FTIR), was employed using a PerkinElmer Spectrum Two FT-IR spectrometer equipped to investigate the chemical structure and functional groups present in the synthesized SAP-EGS hydrogel. FTIR analysis was performed on the raw EGS powder, the SAP-EGS composite hydrogel, before and after the chloride adsorption test to evaluate the interactions between the polymer matrix and the EGS component. Prior to analysis, the raw EGS, SAP-EGS hydrogel before chloride adsorption, and SAP-EGS hydrogel after chloride adsorption were dried at 60 °C until constant weight and finely ground into powder. The powdered samples were placed directly onto the ATR crystal, and the spectra were recorded over the range of 4000–400 cm^{-1}. The obtained spectra were used to identify characteristic functional groups associated with AA, AM, and $CaCO_3$, as well as to confirm successful incorporation of EGS particles into the hydrogel network and evaluate changes in functional groups after chloride removal experiments.

The surface morphology and microstructure of the synthesized SAP-EGS hydrogel were examined using Scanning Electron Microscopy (SEM) - Zeiss Gemini360 FESEM. Before analysis, the samples were dried and mounted on conductive sample holders. SEM imaging was performed at various magnifications to evaluate the surface texture, pore structure, and distribution of EGS particles within the polymer matrix. The micrographs were used to assess the structural characteristics of the hydrogel that may influence water absorption and chloride removal performance.

Energy Dispersive X-ray Spectroscopy (EDX) was conducted in conjunction with SEM analysis to determine the elemental composition of the SAP-EGS hydrogel. EDX spectra and elemental mapping were used to identify and quantify the major elements present in the composite

material. The analysis was used to verify the successful incorporation and distribution of calcium-containing particles within the hydrogel matrix and to support the proposed mechanism for chloride removal.

3.2.4 Study of Swelling and Adsorption

To evaluate chloride removal performance, 5 mL of water sample (collected from Swan Lake) was added to the prepared SAP-EGS hydrogel. The system was left undisturbed for 24 hours to allow swelling and interaction between the hydrogel and dissolved ions. During this period, the hydrogel absorbed water and concentrated ions within its network. After the swelling process, 2 mL of methanol was added to the hydrogel. The system was maintained at 4 °C for 24 hours to facilitate the release of absorbed water and dissolution of precipitated salts within the hydrogel matrix. Unless otherwise stated, 1.52 g of dry SAP-EGS hydrogel was used in each chloride removal experiment.

After complete desorption, the released liquid was collected and analyzed for residual chloride concentration using a HACH DR3900 spectrophotometer equipped with TNT879 Chloride reagent vials (1–1000 mg/L Cl^-). The chloride removal performance of the SAP-EGS hydrogel was evaluated using chloride removal efficiency and equilibrium chloride uptake capacity. Chloride concentrations before and after treatment were measured using a HACH DR3900 spectrophotometer. Because 2 mL of methanol was added during the desorption step, the resulting dilution was accounted for in the chloride concentration calculations. Accordingly, all chloride removal efficiencies and equilibrium uptake capacities were calculated based on the original 5 mL water-sample volume, with the effect of methanol addition on the measured chloride concentration taken into consideration.

A control experiment was performed using commercial $CaCO_3$ instead of EGS powder to evaluate the specific contribution of EGS-derived calcium to chloride removal. The SAP-$CaCO_3$ hydrogel was synthesized following the same polymerization conditions and tested under identical adsorption and desorption procedures. The SAP synthesized without EGS was also evaluated under identical experimental conditions to determine whether the polymer matrix alone exhibited any chloride adsorption.

3.2.5. Adsorption Isotherm Analysis

Although the SAP–EGS system is proposed to remove chloride through multiple mechanisms, including water absorption, ion concentration, and calcium-assisted precipitation, adsorption isotherm models were employed as empirical tools to describe and compare the equilibrium behavior of chloride removal under different initial concentrations. Therefore, the fitted isotherm parameters should not be interpreted as evidence that adsorption is the sole or dominant removal mechanism, but rather as mathematical models for evaluating equilibrium performance and facilitating comparison with previous studies.

The chloride removal efficiency was calculated using Equation (1):

$$\text{Removal Efficiency (\%)} = \left(\frac{C_0 - C_e}{C_0}\right) \times 100 \qquad \text{Equation (1)}$$

where C_0 and C_e represent the initial and equilibrium chloride concentrations (mg/L), respectively.

The equilibrium chloride uptake capacity, q_e was calculated using Equation (2):

$$q_e = \frac{(C_0 - C_e)V}{m} \qquad \text{Equation (2)}$$

where q_e is the equilibrium chloride uptake capacity (mg g^{-1}), (V) is the solution volume (L), and (m) is the dry mass of the SAP-EGS hydrogel (g).

To evaluate the equilibrium behavior of the system, the experimental data were fitted using Langmuir and Freundlich isotherm models. The Langmuir isotherm assumes monolayer adsorption on a homogeneous surface and is expressed as Equation (3):

$$q_e = \frac{q_{max} K_L C_e}{1 + K_L C_e} \quad \text{Equation (3)}$$

Where q_{max} is the maximum adsorption capacity (mg g^{-1}) and K_L is the Langmuir adsorption constant (L mg^{-1}).

Freundlich isotherm describes adsorption on heterogeneous surfaces and is represented by Equation (4):

$$q_e = K_F C_e^{\frac{1}{n}} \quad \text{Equation (4)}$$

where K_F is the Freundlich adsorption constant and (n) is the adsorption intensity parameter.

The isotherm parameters were obtained from the equilibrium chloride concentration and uptake capacity data.(Kataria & Garg, 2018; M. Song et al., 2025)

3.2.6. SAP-EGS Reusability Test

To assess hydrogel stability and repeated performance, the optimized SAP-EGS formulation underwent multiple adsorption- desorption cycles. After each chloride adsorption cycle, methanol-assisted water desorption and low-temperature storage (4°C) were applied before reusing the

hydrogel in subsequent chloride adsorption experiments. Chloride removal efficiency was monitored after each cycle.

3.2.7. Statistical Analysis

All experiments were performed in triplicate (n = 3), and the results are presented as mean ± standard deviation (SD). Statistical analyses were conducted using Microsoft Excel 365 (Microsoft Corporation, Redmond, WA, USA). Differences among multiple experimental groups were evaluated using one-way analysis of variance (ANOVA), followed by Tukey's post hoc test for pairwise comparisons. Comparisons between two groups were performed using an independent two-tailed Student's t-test. Statistical significance was accepted at $p < 0.05$. The goodness-of-fit of the Langmuir and Freundlich isotherm models was evaluated using the coefficient of determination (R^2).

3.3. Results and discussion

3.3.1 Optimization of EGS Concentration and Monomer Ratio

The chloride removal performance of the SAP–EGS hydrogel was optimized by investigating the effects of EGS loading and the AA-AM monomer ratio. EGS concentrations of 0.12, 0.18, 0.24, 0.30, 0.36, and 0.48 g were evaluated while maintaining identical synthesis and testing conditions. Methanol (MeOH) was introduced into the SAP-EGS system to alter the solvent environment and facilitate calcium chloride interactions through changes in ion solvation and water activity. The addition of methanol reduces the availability of free water molecules because of hydrogen-bonding interactions between methanol and water, thereby decreasing the effective solvation of dissolved ions and increasing local supersaturation conditions. Previous studies reported that increasing methanol concentration promotes calcium-based precipitation by reducing

solvent availability and enhancing supersaturation, which consequently increases the amount of precipitated calcium-containing species. In methanol-containing systems, calcium ion behavior is significantly influenced by solvent composition, as methanol modifies ion coordination and solvent structure around Ca^{2+}, while still maintaining strong calcium–water interactions. This altered solvent environment may favor the concentration and possible crystallization or phase separation of calcium–chloride species following chloride adsorption in the SAP-EGS matrix. Additionally, storing the system at low temperature (4 °C) after methanol addition may further facilitate ion stabilization and precipitation processes by reducing molecular mobility and promoting phase separation. Therefore, methanol was employed as a solvent-modifying agent to reduce water activity, influence Ca^{2+} solvation, and potentially enhance chloride recovery through calcium-associated species formation. (Alamdari & Saffari, 2012; Owczarek et al., 2007; Tanewska-Osinska & Barczynska, 1984)

As shown in Fig. 16.a, the chloride removal performance initially increased with increasing EGS content, reaching a maximum at 0.24 g EGS, where the chloride concentration decreased from 213 mg L^{-1} to 119 mg L^{-1}. This improvement is attributed to the increased availability of calcium-rich active sites supplied by the EGS particles, which promoted chloride removal through calcium-mediated interactions.

When the EGS loading exceeded 0.24 g, the chloride removal performance gradually decreased. The formulation containing 0.48 g EGS exhibited no measurable chloride removal. The reduced performance at higher EGS contents is likely due to non-uniform dispersion within the hydrogel matrix. Visible agglomeration of EGS particles was observed during mixing, leading to a heterogeneous composite structure. Excessive filler loading may also interfere with polymerization, resulting in a less uniform hydrogel structure with lower swelling capacity. Error

bars shown in Fig. 16 represent the standard deviation of three independent experiments. A one-way analysis of variance (ANOVA) was performed to evaluate the effect of EGS content on the final chloride concentration. The results showed a statistically significant difference among the formulations ($F(5, 12) = 328.41$, $p = 2.12 \times 10^{-12}$), indicating that EGS content significantly influenced chloride removal performance. The hydrogel containing 0.24 g EGS exhibited the highest chloride reduction (90.3 ± 3.5 mg L^{-1}), which was significantly greater than all other formulations. Increasing the EGS loading to 0.48 g resulted in no measurable chloride reduction because excessive EGS caused particle agglomeration and poor dispersion within the hydrogel matrix.

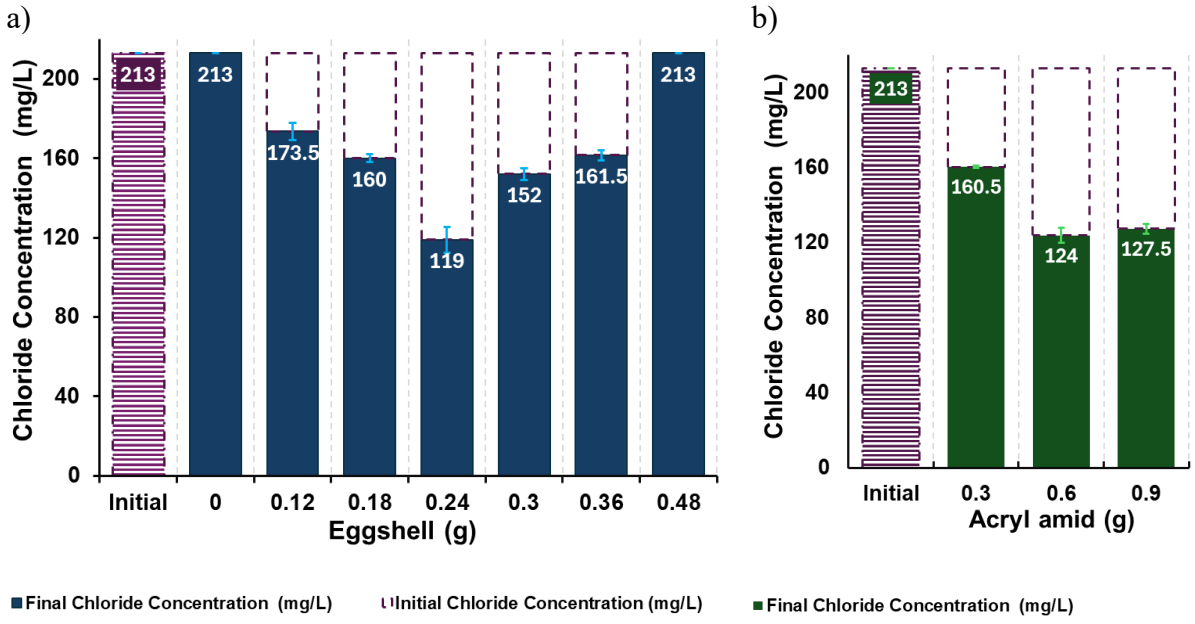

Figure 16- a) Effect of EGS loading on chloride removal performance of the SAP-EGS hydrogel. Error bars represent mean ± SD (n = 3). Different letters indicate significant differences ($p < 0.05$). b) Effect of acrylic acid-to-acrylamide ratio on chloride removal performance of the SAP-EGS hydrogel. Error bars represent mean ± SD (n = 3). Different letters indicate significant differences ($p < 0.05$).

The influence of monomer composition on chloride removal was also investigated by varying the AA-AM ratio while maintaining the optimized EGS loading of 0.24 g. As shown in Fig.16.b,

the 1:1 AA-AM ratio exhibited the highest chloride removal performance, reducing the chloride concentration from 213 mg L^{-1} to approximately 119–127 mg L^{-1}, corresponding to a chloride reduction of approximately 40–45%. Increasing the AM content improved the integrity and swelling behavior of the hydrogel, whereas excessive AA reduced structural stability and chloride removal performance. These observations suggested that a balanced monomer composition provides an optimal combination of hydrophilic functional groups and network stability, allowing efficient water absorption while maintaining sufficient mechanical strength for effective chloride removal. Based on these optimization results, the SAP–EGS hydrogel containing 0.24 g EGS and a 1:1 AA_AM ratio was selected for all subsequent characterization and chloride removal experiments. A one-way analysis of variance (ANOVA) was conducted to evaluate the effect of the acrylic acid-to-acrylamide (AA:AAm) ratio on the final chloride concentration. The analysis revealed a statistically significant effect of monomer composition ($F(2, 6) = 136.67$, $p = 9.91 \times 10^{-6}$), demonstrating that the AA:AAm ratio significantly affected the chloride removal performance of the SAP–EGS composite. The 1:1 formulation exhibited the highest chloride reduction (89.0 ± 4.4 mg L^{-1}), followed by the 1:2 formulation (86.0 ± 2.6 mg L^{-1}), whereas the 2:1 formulation showed a significantly lower chloride reduction (51.7 ± 1.5 mg L^{-1}, $p < 0.05$). The comparable performance of the 1:1 and 1:2 formulations suggest that increasing the acrylamide content did not substantially improve chloride removal under the investigated conditions.

No measurable chloride removal was observed, confirming that the SAP itself does not adsorb Cl^- and that the chloride removal capability of the SAP-EGS composite is attributed to the incorporation of EGS-derived calcium. Also, the superabsorbent polymer (SAP) was tested in the absence of EGS, and no detectable chloride removal was observed, confirming that the SAP itself does not adsorb chloride ions.

3.3.2 Physicochemical characterization

3.3.2.1 Chemical Structure Analysis

The FTIR spectra of EGS, SAP-EGS, and SAP-EGS after chloride removal are presented in Fig 17. The spectra provide evidence for the successful incorporation of EGS into the polymer matrix and the subsequent interaction of calcium ions with the functional groups of the hydrogel.

The FTIR spectrum of EGS exhibited the characteristic absorption bands of $CaCO_3$, the major constituent of EGS. A broad absorption band observed in the region of 3200–3400 cm^{-1} was attributed to the stretching vibration of hydroxyl groups associated with adsorbed moisture. The intense absorption band around 1410–1450 cm^{-1} corresponded to the asymmetric stretching vibration of carbonate ions (CO_3^{2-}). Additional characteristic carbonate peaks appeared at approximately 875 cm^{-1} and 710 cm^{-1}, corresponding to the out-of-plane and in-plane bending vibrations of CO_3^{2-}, respectively, confirming the presence of calcite-type $CaCO_3$ in the EGS material.(Gunasekaran et al., 2006; Gunasekaran & Anbalagan, 2007)

Following polymerization, the SAP-EGS spectrum displayed several new absorption bands that were absent in the EGS spectrum, confirming the successful formation of the superabsorbent polymer network. The bands observed at approximately 2930–2850 cm^{-1} were assigned to the stretching vibrations of aliphatic C–H groups from the polymer backbone. A prominent absorption peak near 1650 cm^{-1} was attributed to the amide I vibration (C=O stretching) of acrylamide units, while the band around 1540 cm^{-1} corresponded to the amide II vibration arising from N–H bending and C–N stretching. The broad band in the 3200–3400 cm^{-1} region was associated with overlapping O–H and N–H stretching vibrations originating from AA, AM, and adsorbed water molecules. The retention of carbonate-related bands together with the appearance of characteristic

polymer peaks confirmed the successful incorporation of EGS particles within the SAP matrix. Compared with the reported SAP, the SAP-EGS composite exhibited additional absorption bands at approximately 1406, 879, and 710 cm^{-1}, corresponding to the asymmetric stretching and bending vibrations of carbonate (CO_3^{2-}) groups. These peaks originated from the EGS-derived $CaCO_3$ phase and were also observed in the FTIR spectrum of the pristine EGS sample. The coexistence of characteristic SAP and carbonate bands demonstrated the successful incorporation of EGS particles into the hydrogel matrix. Furthermore, the increased intensity of several absorption bands in the SAP-EGS spectrum suggested interactions between the polymer functional groups and the $CaCO_3$ filler, indicating the formation of a composite structure rather than a simple physical mixture.(Tabesh, Zabihihesari, et al., 2025)

Significant spectral changes were observed after the incorporation of $CaCl_2$, indicating interactions between calcium ions and the functional groups of the hydrogel network. The SAP-EGS after chloride removal spectrum exhibited a broader absorption band in the hydroxyl region (3200–3400 cm^{-1}), suggesting enhanced hydrogen bonding and increased bound water associated with the calcium-containing hydrogel structure. Noticeable changes in the region between 1650 and 1400 cm^{-1} were also observed. These variations are attributed to the interaction of Ca^{2+} ions with carboxylate ($–COO^-$) and carbonyl-containing groups present in the polymer network.

The increased intensity and slight shifts observed in the carboxylate region indicated the formation of calcium–carboxylate complexes. Calcium ions can act as ionic crosslinking agents by forming bridges between neighboring carboxylate groups. This ionic crosslinking mechanism increases the structural stability of the hydrogel and contributes to the formation of a denser polymer network. Furthermore, changes were observed in the fingerprint region (1200–800 cm^{-1})

suggesting alterations in the local chemical environment of both the polymer chains and EGS particles following calcium incorporation.

It should be noted that chloride ions do not possess characteristic IR-active vibrations and therefore cannot be directly identified by FTIR spectroscopy. Consequently, the observed spectral modifications were primarily attributed to the interaction of Ca^{2+} ions with the functional groups of the SAP-EGS matrix rather than direct detection of chloride ions. Nevertheless, the FTIR results clearly demonstrated the successful incorporation of calcium ions into the hydrogel structure and provide evidence of enhanced ionic crosslinking within the SAP-EGS after chloride removal.

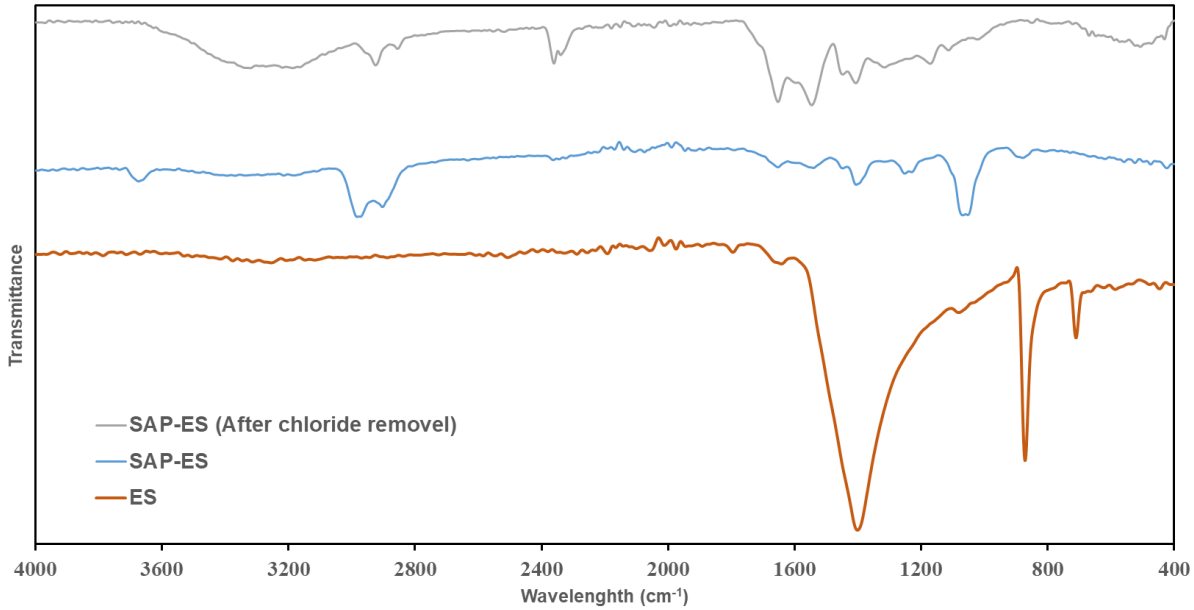

Figure 17- FTIR spectra of (a) raw EGS, (b) SAP-EGS composite hydrogel before chloride adsorption, and (c) SAP-EGS hydrogel after chloride removal, showing the characteristic functional groups and chemical interactions associated with chloride removal.

Overall, the FTIR analysis confirmed the presence of EGS-derived calcium carbonate, successful synthesis of the SAP polymer network, and the effective incorporation of calcium ions into the SAP-EGS structure, resulting in a chemically and structurally modified hydrogel with enhanced crosslinking characteristics.

3.3.2.2 Morphological Analysis

The surface morphology of the synthesized SAP–EGS composite, pristine SAP, and EGS was investigated using SEM and the corresponding micrographs are presented in Fig. 18(a–j).

The SEM images of the SAP–EGS composite (Fig. 18.a–c) revealed a three-dimensional porous architecture consisting of interconnected cavities and irregular polymer walls. The formation of pores with various sizes provides a large internal surface area that facilitates water absorption and enhances mass transfer during chloride removal. The polymer matrix appeared continuous and well developed, indicating successful hydrogel formation. In addition to the porous network, irregular bright particulate domains were observed on and within the polymer surface (Fig. 18.c), suggesting the presence of embedded mineral particles originating from the incorporated EGS.

A higher-magnification SEM image (Fig. 18.d) clearly shows an irregular rough particle attached to the polymer surface. The particle exhibits a dense and granular morphology that differs from the surrounding smooth polymer matrix, indicating successful incorporation of the EGS filler into the SAP network. The intimate contact between the mineral particle and the hydrogel matrix suggested that the EGS became physically embedded during polymerization rather than remaining loosely attached to the surface.

Additional SEM images of the SAP–EGS composite (Fig. 18.e–f) further demonstrated the continuity of the polymer network and the presence of fracture lines generated during sample preparation and drying. Despite these localized cracks, the hydrogel retained its interconnected porous structure, which is advantageous for rapid water uptake and diffusion of chloride ions throughout the composite.

For comparison, SEM images of the pristine SAP without EGS (Fig. 3g–i) exhibited a relatively smooth polymer surface with layered fracture patterns and fewer mineral-like features. The absence of bright particulate domains confirmed that the observed particles in the SAP–EGS composite originated from the incorporated EGS rather than the polymer itself. The pristine SAP maintained its characteristic hydrogel morphology with interconnected pores, demonstrating that incorporation of EGS did not disrupt formation of the polymer network.

The morphology of the raw EGS powder (Fig. 18.j) exhibited irregularly shaped particles with rough surfaces and a porous texture, providing numerous potential active sites for interaction with a chloride-containing solution. The rough mineral surface may also promote mechanical anchoring within the polymer matrix during composite synthesis.

Overall, the SEM observations demonstrated that the SAP–EGS composite combined the highly porous three-dimensional structure of the SAP polymer with embedded EGS particles, producing a composite morphology favorable for water absorption and enhanced contact between chloride ions and the calcium-rich mineral phase.

3.3.2.3 Energy-Dispersive X-ray Spectroscopy (EDS)

The elemental composition of the synthesized materials was analyzed using EDS, and the corresponding spectra are presented in Fig. 18(k–m).

The EDS spectrum of the pristine SAP (Fig. 18.k) was dominated by carbon (57.79 wt.%) and oxygen (7.53 wt.%), which are the principal constituents of the polymer backbone. Small amounts of sodium, sulfur, and potassium were also detected, originating from the polymer synthesis and residual reagents. Notably, calcium was absent, confirming that the pristine SAP contained no mineral filler.

After incorporation of EGS, the EDS spectrum of the SAP–EGS composite before chloride treatment (Fig. 18.l) showed the appearance of a distinct calcium (Ca) peak, together with increased oxygen content, confirming successful incorporation of the calcium carbonate-rich EGS into the polymer matrix. Carbon remained the dominant element due to the organic nature of the hydrogel, while the detected calcium verified the presence of the mineral phase within the composite. These results aligned with the SEM observations and confirmed that mineral particles were embedded in the polymer network.

Following chloride removal (Fig. 18.m), calcium remained detectable in the SAP–EGS composite, indicating that the EGS-derived mineral phase was retained within the hydrogel after treatment. In addition, the appearance of chlorine (Cl) in the EDS spectrum confirmed the presence of chloride associated with the composite after exposure to a chloride-containing solution, providing direct evidence of chloride uptake. The simultaneous detection of calcium and chlorine supports the proposed chloride removal mechanism involving interaction between chloride ions and the calcium-rich EGS incorporated within the SAP matrix. The decrease in carbon content after treatment is consistent with greater exposure of the mineral phase following swelling and desorption of the hydrogel. The aluminum (Al) signal originated from the aluminum SEM mounting stub and was not considered part of the sample composition.

The combined SEM and EDS analyses demonstrated the successful fabrication of the SAP–EGS composite, confirming both the incorporation of EGS-derived calcium-rich particles into the porous polymer matrix and the association of chloride with the composite after treatment. This integrated porous-mineral structure is expected to enhance chloride removal by combining the high-water absorption capacity of the SAP with the calcium-rich reactive sites provided by the EGS.

a)

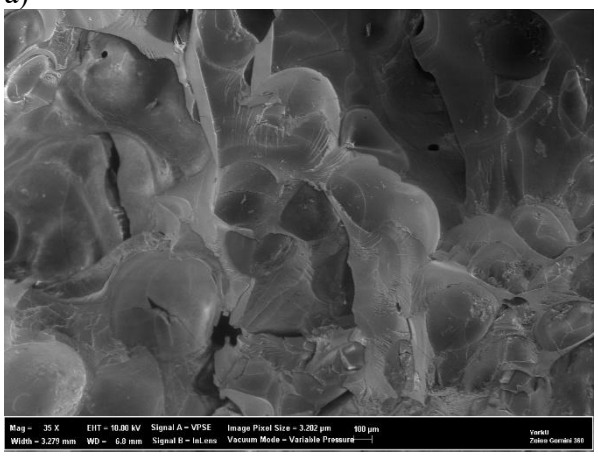
Mag = 35 X EHT = 10.00 kV Signal A = VPSE Image Pixel Size = 3.202 µm 100 µm
Width = 3.279 mm WD = 6.0 mm Signal B = InLens Vacuum Mode = Variable Pressure
YorkU
Zeiss Gemini 360

b)

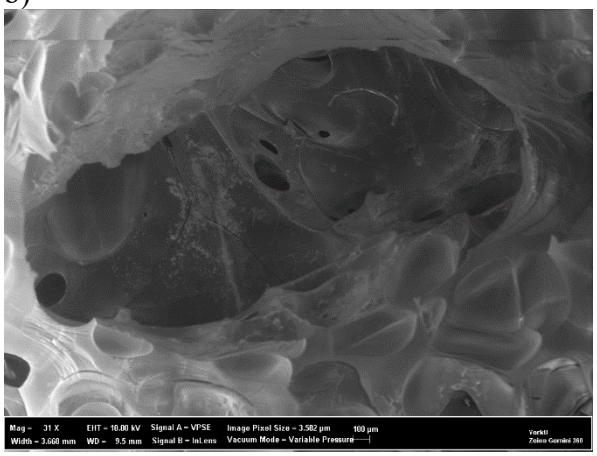
Mag = 31 X EHT = 10.00 kV Signal A = VPSE Image Pixel Size = 3.582 µm 100 µm
Width = 3.668 mm WD = 9.5 mm Signal B = InLens Vacuum Mode = Variable Pressure
YorkU
Zeiss Gemini 360

c)


Mag = 75 X EHT = 10.00 kV Signal A = VPSE Image Pixel Size = 1.489 µm 100 µm
Width = 1.524 mm WD = 9.4 mm Signal B = InLens Vacuum Mode = Variable Pressure
YorkU
Zeiss Gemini 360

d)

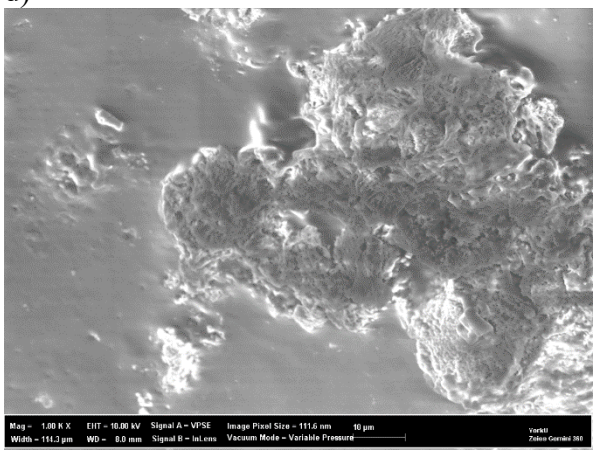
Mag = 1.80 K X EHT = 10.00 kV Signal A = VPSE Image Pixel Size = 111.6 nm 10 µm
Width = 111.3 µm WD = 8.0 mm Signal B = InLens Vacuum Mode = Variable Pressure
YorkU
Zeiss Gemini 360

e)

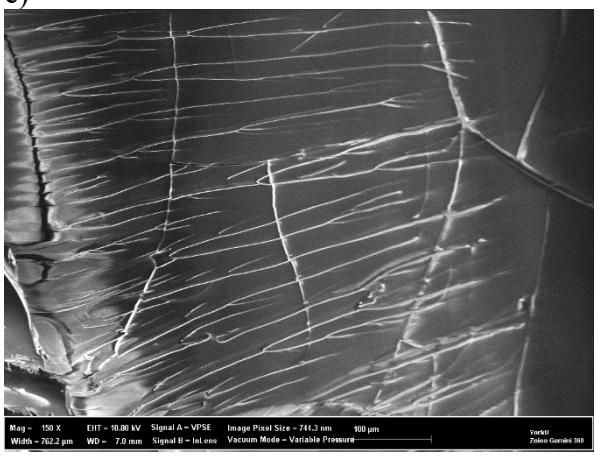
Mag = 150 X EHT = 10.00 kV Signal A = VPSE Image Pixel Size = 741.3 nm 100 µm
Width = 762.2 µm WD = 7.0 mm Signal B = InLens Vacuum Mode = Variable Pressure
YorkU
Zeiss Gemini 360

f)

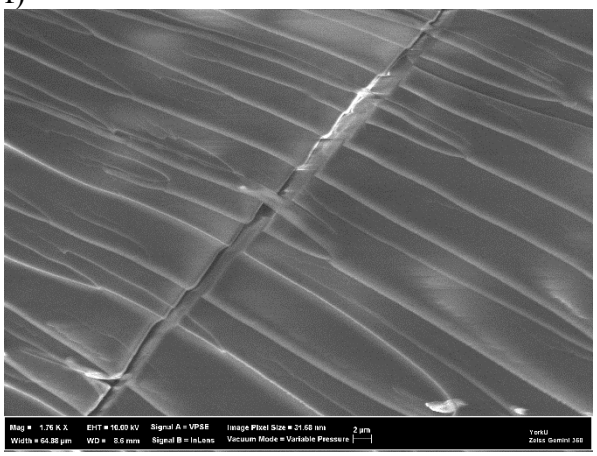
Mag = 1.76 K X EHT = 10.00 kV Signal A = VPSE Image Pixel Size = 31.68 nm 2 µm
Width = 64.88 µm WD = 8.6 mm Signal B = InLens Vacuum Mode = Variable Pressure
YorkU
Zeiss Gemini 360

g)

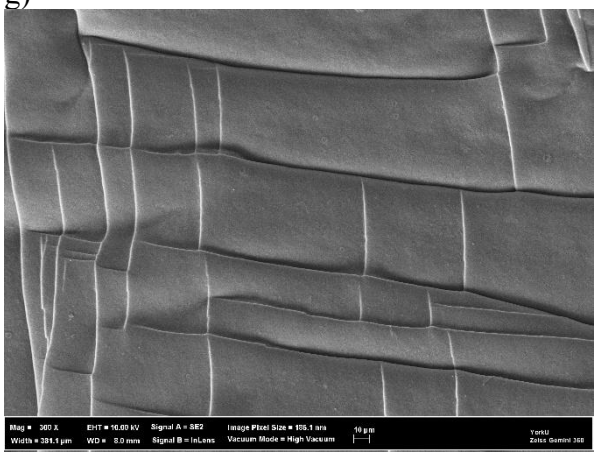

h)

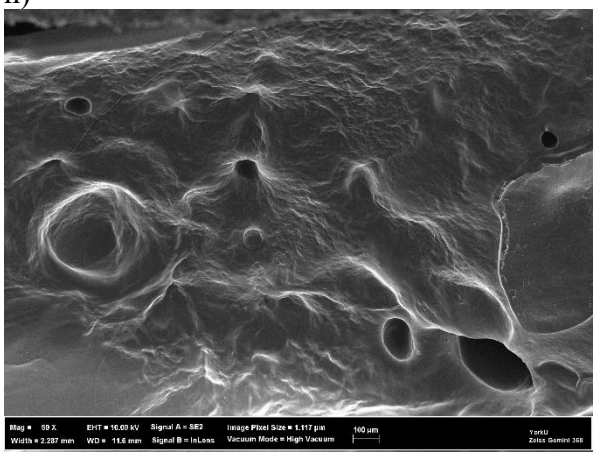

i)

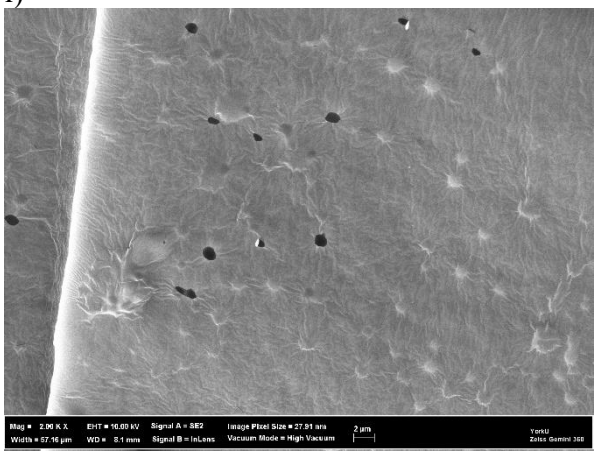

j)

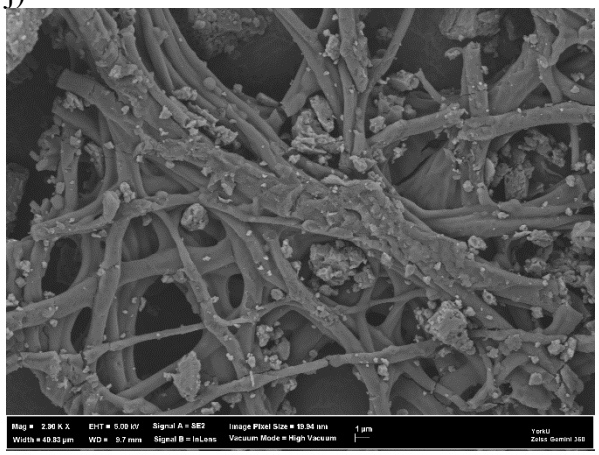

k)

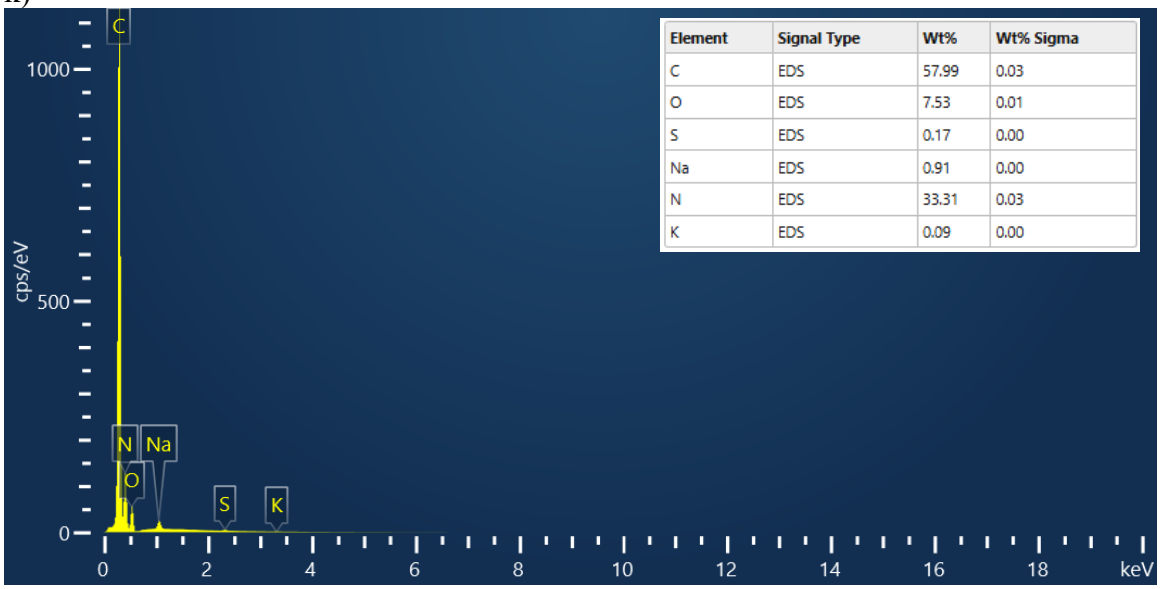

Element	Signal Type	Wt%	Wt% Sigma
C	EDS	57.99	0.03
O	EDS	7.53	0.01
S	EDS	0.17	0.00
Na	EDS	0.91	0.00
N	EDS	33.31	0.03
K	EDS	0.09	0.00

l)

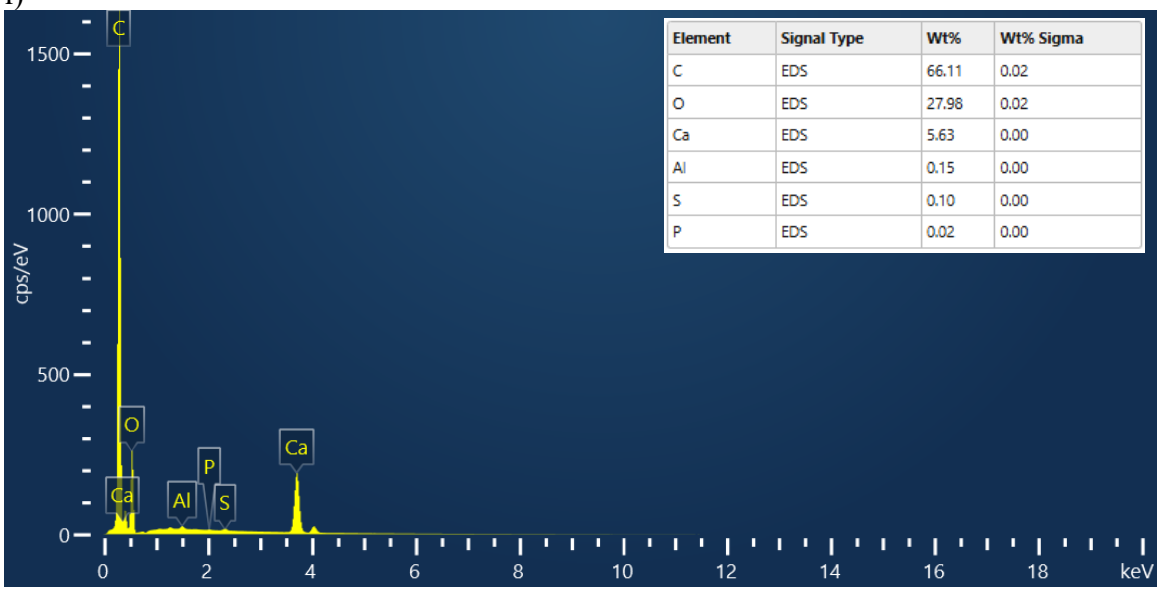

Element	Signal Type	Wt%	Wt% Sigma
C	EDS	66.11	0.02
O	EDS	27.98	0.02
Ca	EDS	5.63	0.00
Al	EDS	0.15	0.00
S	EDS	0.10	0.00
P	EDS	0.02	0.00

m)

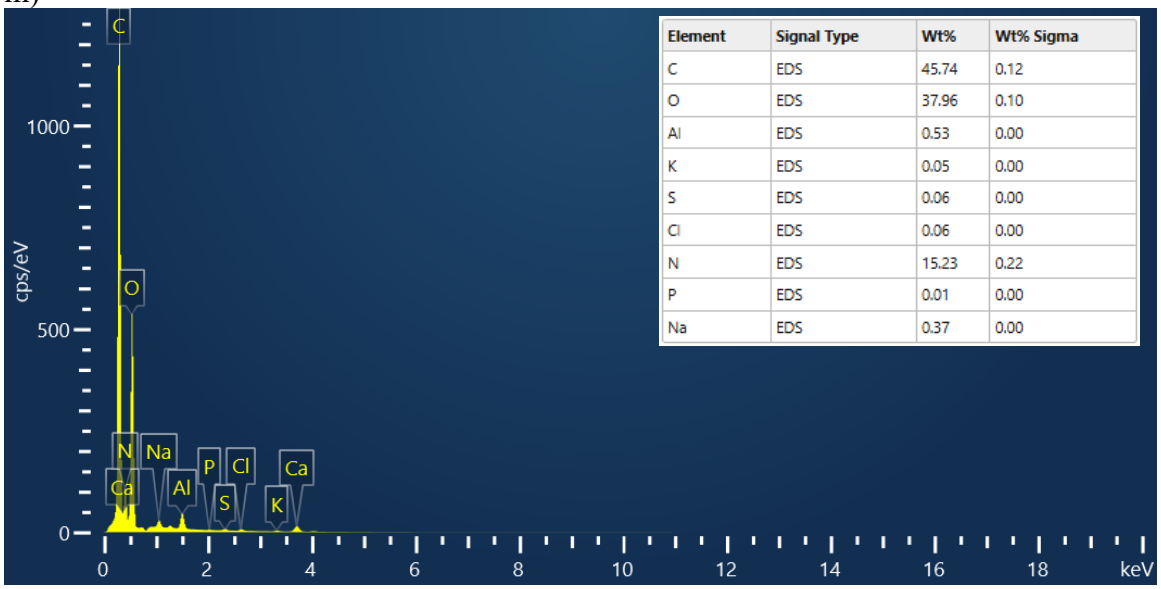

Element	Signal Type	Wt%	Wt% Sigma
C	EDS	45.74	0.12
O	EDS	37.96	0.10
Al	EDS	0.53	0.00
K	EDS	0.05	0.00
S	EDS	0.06	0.00
Cl	EDS	0.06	0.00
N	EDS	15.23	0.22
P	EDS	0.01	0.00
Na	EDS	0.37	0.00

Figure 18- Morphological and elemental characterization of the synthesized materials. SEM micrographs of the SAP–EGS composite hydrogel at different magnifications (a–f), pristine SAP hydrogel (g–i), and raw EGS powder (j). EDS spectra of pristine SAP (k), SAP–EGS composite before chloride removal (l), and SAP–EGS composite after chloride removal (m), confirming the incorporation of EGS-derived calcium into the hydrogel matrix and the presence of chloride following treatment.

3.3.3 Chloride Adsorption Performance

The optimized SAP–EGS hydrogel was evaluated for chloride removal using Swan Lake water containing elevated chloride concentrations. Under the optimized conditions, the hydrogel reduced the chloride concentration from an initial value of 213 mg L^{-1} to approximately 119 mg L^{-1}, approaching the Canadian long-term freshwater guideline of 120 mg L^{-1}. These results demonstrated the potential of the SAP–EGS composite as a sustainable material for mitigating chloride pollution in freshwater systems impacted by road salt application.

The chloride removal mechanism is proposed to involve several sequential processes. Initially, the superabsorbent polymer rapidly absorbs the contaminated water, causing chloride ions to become concentrated within the swollen hydrogel network. Simultaneously, calcium ions released from the embedded EGS-derived calcium carbonate become available within the confined aqueous environment. Following methanol-assisted desorption and low-temperature storage, the concentrated chloride-containing solution interacts with the calcium species, promoting calcium-mediated chloride capture and facilitating chloride removal from the recovered solution.

To distinguish the contribution of each component of the composite, two control experiments were performed under identical experimental conditions. In the first control, the synthesized SAP without EGS was evaluated. No detectable chloride removal was observed, confirming that the polymer matrix alone does not adsorb chloride ions and does not contribute directly to chloride removal. This finding demonstrated that the SAP polymer primarily functions as a water-absorbing support matrix rather than an active chloride-removing material.

A second control experiment was conducted using 0.2256 g of commercial $CaCO_3$, corresponding to the amount of calcium carbonate present in 0.24 g of EGS incorporated into the

SAP–EGS composite. The commercial $CaCO_3$ reduced the chloride concentration from 213 mg L^{-1} to 111 mg L^{-1}, exhibiting chloride removal behavior very similar to that of the SAP–EGS composite. These results confirmed that the EGS effectively functions as a natural source of $CaCO_3$ and can replace commercial $CaCO_3$ without compromising chloride removal performance. Consequently, the active component responsible for chloride removal is the $CaCO_3$ naturally present in EGS, whereas the SAP enhances the overall process by absorbing water, concentrating chloride ions around the embedded EGS particles, and facilitating the interaction between chloride ions and calcium-containing reactive species.

Overall, the control experiments demonstrated the complementary roles of the two components in the composite. The EGS provided the reactive calcium source responsible for chloride removal, while the SAP polymer served as a porous, water-retaining matrix that improves the efficiency of the calcium-mediated removal process. The combination of these functions resulted in an environmentally sustainable composite capable of utilizing waste EGS as an effective alternative to commercial $CaCO_3$ for chloride mitigation in freshwater systems.

3.3.4 Effect of Initial Chloride Concentration

The effect of the initial chloride concentration on the equilibrium chloride uptake capacity of EGS and the SAP–EGS composite was evaluated over a concentration range of 20–380 mg L^{-1} (Fig. 19). The results demonstrated that EGS exhibited a substantially higher chloride uptake capacity than the SAP–EGS composite at all tested chloride concentrations.

For the EGS sample, the equilibrium chloride uptake capacity (q_e) increased from approximately 0.15 mg g^{-1} at an initial chloride concentration of 20 mg L^{-1} to a maximum value of approximately 2.20 mg g^{-1} at 260 mg L^{-1}. A slight decrease was subsequently observed at

higher chloride concentrations, with q_e values of approximately 2.12 and 1.86 mg g^{-1} at 320 and 380 mg L^{-1}, respectively. This trend suggested that increasing chloride concentration enhanced chloride uptake by providing a greater mass-transfer driving force until the available calcium-containing reactive sites approached saturation.

In contrast, the SAP–EGS composite exhibited significantly lower uptake capacities, increasing gradually from approximately 0.02 mg g^{-1} at 20 mg L^{-1} to a maximum of approximately 0.33 mg g^{-1} at 260 mg L^{-1}, followed by a slight decline to approximately 0.32 and 0.28 mg g^{-1} at 320 and 380 mg L^{-1}, respectively. The lower q_e values are expected because the uptake capacity was normalized to the total mass of the composite, which includes the SAP polymer. Since the polymer itself does not directly contribute to chloride removal, the active $CaCO_3$ content per gram of SAP–EGS is considerably lower than that of pure EGS, resulting in a lower apparent uptake capacity.

Despite the lower mass-normalized uptake capacity, the SAP matrix played a crucial role in the chloride removal process by absorbing the contaminated water and concentrating chloride ions around the embedded EGS particles. This localized enrichment promoted interaction between chloride ions and calcium species released from the EGS-derived $CaCO_3$, enabling efficient chloride removal while utilizing a sustainable waste-derived calcium source.

The similar uptake profiles were observed for both EGS and SAP–EGS, with maximum chloride uptake occurring at an initial chloride concentration of 260 mg L^{-1}, indicating the chloride removal mechanism is primarily governed by the availability of calcium-containing reactive sites rather than by the polymer matrix itself. The decrease in q_e at higher chloride concentrations suggested that the reactive calcium species approached saturation, limiting further chloride uptake.

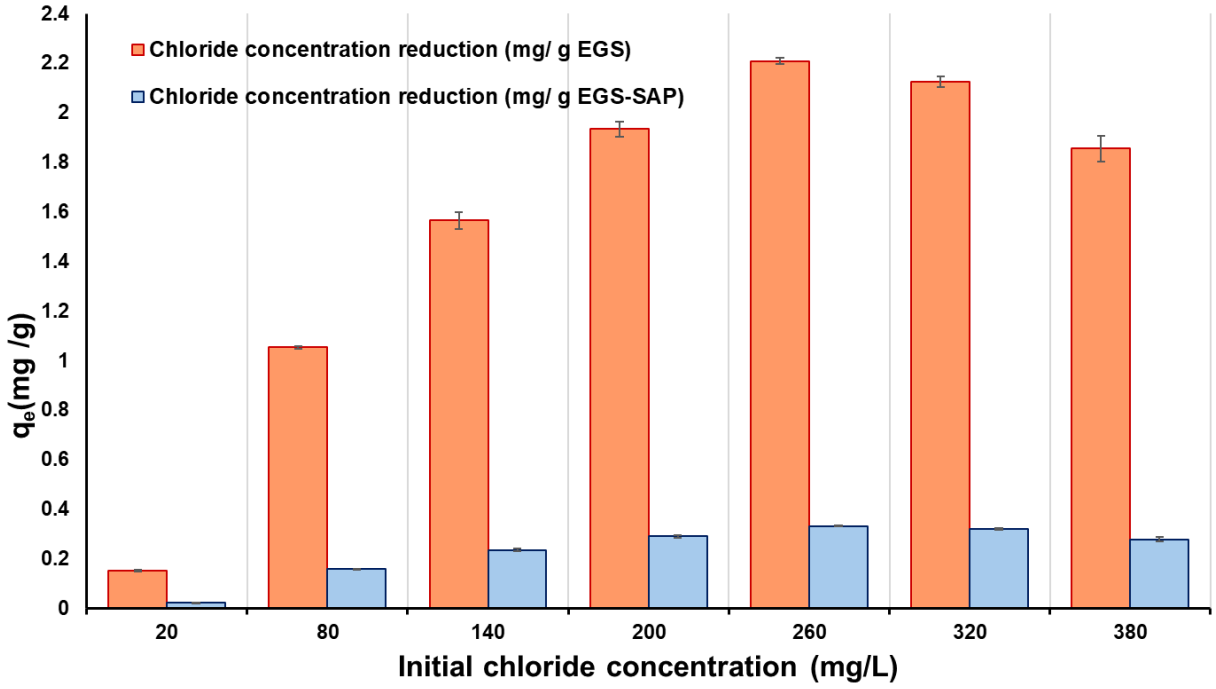

Figure 19- Effect of initial chloride concentration on the equilibrium chloride uptake capacity of EGS and the SAP–EGS composite.

The influence of desorption time was also evaluated following chloride uptake. After absorption of the chloride-containing solution, methanol was added to the swollen SAP–EGS hydrogel to facilitate water release from the polymer network. Complete liquid recovery was achieved after approximately 24 h at 4 °C. Chloride measurements performed after liquid recovery showed no significant changes beyond this period, indicating that equilibrium had been reached. Therefore, a desorption time of 24 h was selected for all subsequent experiments.

3.3.5 Equilibrium Isotherm Analysis

The data point at 20 mg L^{-1} was excluded from the isotherm analysis because it deviated substantially from the linear adsorption trend observed over the concentration range of 80–380 mg L^{-1}. At this low initial chloride concentration, the limited driving force for mass transfer resulted in a disproportionately low equilibrium uptake compared with the remaining data points. Consequently, inclusion of this point reduced the quality of the isotherm fit without representing

the equilibrium behavior observed over the practical concentration range. Similar approaches have been adopted in adsorption studies when low-concentration data fall outside the linear adsorption region. Therefore, the isotherm parameters were determined using the concentration range of 80–380 mg L^{-1}, which better represents the equilibrium behavior of the SAP–EGS composite.

The calculated isotherm parameters are presented in Table 9 and Figure 20. The Langmuir model provided a better fit to the experimental data than the Freundlich model, with correlation coefficients (R^2) of 0.9663 and 0.7428, respectively. The Langmuir maximum adsorption capacity (q_{max}) and adsorption constant (K_L) were determined to be 0.315 mg g^{-1} and 0.0663 L mg^{-1}, respectively. Considering that EGS represents the primary calcium-containing reactive component within the composite, the corresponding chloride uptake capacity normalized to EGS content was approximately 2.10 mg g^{-1} EGS. The maximum chloride uptake capacity of the SAP–EGS composite normalized to the EGS content (2.10 mg g^{-1}) was lower than those reported for other sustainable biomass-derived chloride adsorbents, including unmodified Salix alba leaf biochar (5.54 mg g^{-1}), unmodified apricot seed shell biochar (6.37 mg g^{-1}), and cassava peel biochar (31.25 mg g^{-1}). The lower uptake observed for the SAP–EGS composite is likely related to its design as a proof-of-concept hydrogel system that combines controlled water absorption with a waste-derived calcium source, rather than a conventional porous adsorbent optimized for maximum chloride adsorption (Ishaq et al., 2025; Nyangi, 2024). The superior fit of the Langmuir model suggests that chloride removal by the SAP–EGS hydrogel can be reasonably described by monolayer adsorption on relatively homogeneous active sites within the investigated concentration range. Furthermore, the Freundlich adsorption intensity parameter (n=3.56) was greater than unity, indicating favorable chloride uptake by the SAP–EGS hydrogel.

Table 9. Equilibrium adsorption isotherm parameters for chloride removal by the SAP-EGS hydrogel obtained from the Langmuir and the Freundlich models.

Model	Parameter	Value	R^2
Langmuir	q_{max} (mg g^{-1} SAP-EGS)	0.315	0.966
	q_{max} (mg g^{-1} ES)	2.10	
	K_L (L mg^{-1})	0.066	
Freundlich	K_F	0.069	0.743
	n	3.56	

Although the Langmuir model adequately described the equilibrium data, the observed decrease in chloride uptake at concentrations above 260 mg L^{-1} suggested that the chloride removal mechanism cannot be attributed solely to conventional adsorption processes.

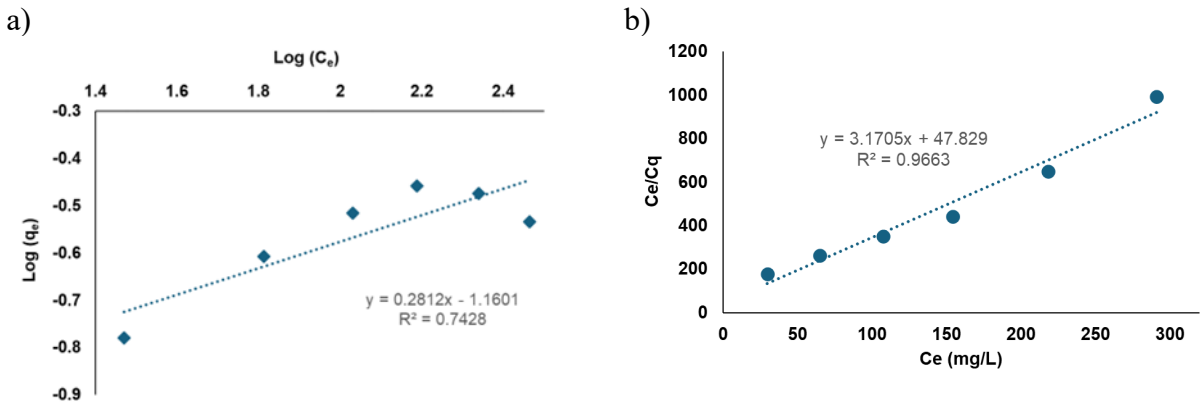

Figure 20- Adsorption isotherm analysis of chloride removal by the SAP-EGS hydrogel: (a) Langmuir isotherm model and (b) Freundlich isotherm model fitted to the experimental equilibrium data.

The overall removal behavior is likely influenced by a combination of hydrogel swelling, water absorption, ion concentration within the polymer network, and calcium-mediated chloride interactions associated with EGS-derived calcium carbonate. These results demonstrated that the SAP–ES hydrogel functions as a multifunctional chloride removal system and exhibited optimum

chloride removal performance at intermediate chloride concentrations, where the balance between chloride availability and active removal sites were maximized.

3.3.6 Reusability Test

The reusability of the optimized SAP–EGS hydrogel was evaluated over five consecutive adsorption–desorption cycles (Fig. 20). The chloride reduction gradually decreased from 87.3 ± 1.2 mg L^{-1} in the first cycle to 81.0 ± 1.0, 61.0 ± 6.2, 57.0 ± 7.0, and 48.7 ± 3.8 mg L^{-1} in the second, third, fourth, and fifth cycles, respectively. A one-way analysis of variance (ANOVA) was performed to assess the effect of reuse cycles on the final chloride concentration. The results indicated a statistically significant difference among the five reuse cycles ($F(4, 10) = 38.75$, $p = 4.66 \times 10^{-6}$), confirming that repeated reuse significantly influenced the chloride removal performance of the SAP–EGS composite. Relative to the initial cycle, the hydrogel retained approximately 93%, 70%, 65%, and 56% of its chloride removal capacity after the second, third, fourth, and fifth cycles, respectively. All experiments were performed in triplicate, and the results are presented as mean ± standard deviation.

The gradual decline in chloride removal indicated that the SAP–EGS composite remained functional after repeated use but experienced a progressive loss in performance. This behavior may be attributed to structural changes within the hydrogel network caused by repeated swelling–deswelling cycles and incomplete regeneration. However, calcium release and chloride mass balance were not quantified in the present study; therefore, the exact mechanism responsible for the performance decline could not be conclusively established. Future work will include calcium release measurements, chloride mass balance analysis, and post-use structural characterization to better understand the regeneration behavior of the SAP–EGS composite.

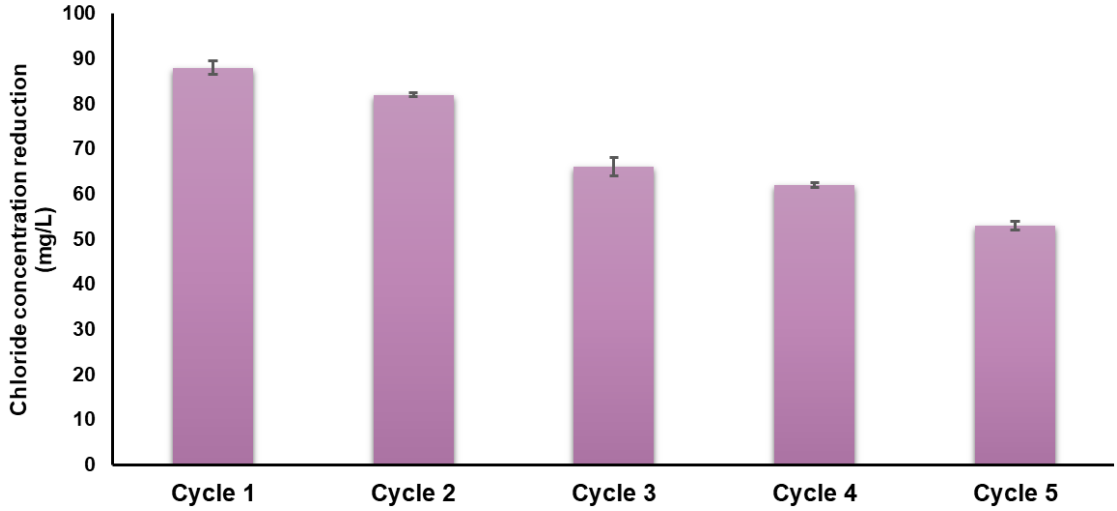

Figure 21- Reusability of the optimized SAP-EGS hydrogel over consecutive adsorption–desorption cycle

3.4 Conclusion

This study presents a proof-of-concept for the use of a waste EGS-integrated superabsorbent polymer (SAP–EGS) hydrogel as a sustainable material for reducing chloride concentrations in road salt-contaminated freshwater. By combining the high-water absorption capacity of SAP with calcium-rich waste EGSs, the developed composite provides a simple and sustainable approach for chloride reduction while promoting the valorization of food waste within a circular economy framework.

The optimized SAP–EGS hydrogel, containing 0.24 g EGS and a 1:1 acrylic acid-to-acrylamide ratio, reduced chloride concentrations from approximately 213 to 119 mg L^{-1}, corresponding to a maximum chloride removal efficiency of 63.1% in different initial concentration of chloride. SEM and EDS analyses confirmed the successful incorporation of EGS particles into the polymer matrix and detected chlorine on the composite after treatment. Control experiments further demonstrated that the SAP matrix alone exhibited no measurable chloride

removal, whereas the incorporation of EGS was essential for the observed reduction in chloride concentration.

The developed composite offers several sustainability advantages, including the utilization of an abundant waste material, mild synthesis conditions, and the potential to reduce reliance on commercially sourced calcium-based materials. Although the chloride removal mechanism could not be conclusively established in the present study, the results demonstrate the feasibility of the SAP–EGS composite as a promising material for chloride reduction in freshwater.

Future work should focus on confirming the underlying removal mechanism through complementary analyses, including XRD, calcium mass balance, and ion balance measurements, as well as evaluating regeneration performance, long-term stability, and continuous-flow operation under environmentally relevant conditions. Overall, this work establishes a foundation for the further development and optimization of waste-derived hydrogel composites for sustainable freshwater treatment.

Chapter 4: Conclusion and future work

4.1 Conclusion

This thesis investigated the development of sustainable functional materials for water treatment, with emphasis on chloride mitigation and antimicrobial applications. By integrating a comprehensive literature review with two experimental investigations, this work established a systematic pathway from material design to practical environmental application.

The literature review critically evaluated recent advances in nanoflower-based membrane engineering and established a structure–transport–reactivity framework linking nanoflower morphology, surface chemistry, and membrane architecture with separation, adsorption, photocatalytic activity, and antifouling performance. The review also identified key challenges associated with material stability, scalability, and practical implementation, providing the scientific foundation for the experimental studies conducted in this thesis.

Guided by these findings, a biochar-supported curcumin–copper phosphate hybrid nanoflower (BC–NFs) composite was successfully synthesized through a biomimetic self-assembly approach. SEM, EDS, XRD, FTIR, fluorescence microscopy, and BET analyses confirmed the successful formation of hierarchical crystalline copper phosphate nanoflowers and their uniform immobilization on the porous biochar surface. Although the composite demonstrated limited chloride adsorption, it exhibited strong antibacterial activity against Escherichia coli, demonstrating its potential as a multifunctional material for water disinfection and biofouling control.

To address chloride contamination caused by road salt, a waste-derived EGS–superabsorbent polymer (SAP–EGS) composite was developed. Experimental optimization identified the optimum EGS loading and monomer composition for chloride removal. Under optimized conditions, the SAP–EGS hydrogel achieved a maximum chloride removal efficiency of 63.13% from chloride-contaminated water. Adsorption equilibrium was successfully described using Langmuir and Freundlich isotherm models, while reusability experiments demonstrated stable performance over five consecutive adsorption–desorption cycles, confirming the regeneration potential of the composite for repeated use.

Overall, this research demonstrates that bio-inspired and waste-derived materials can provide complementary solutions for sustainable water treatment. While the BC–NFs composite offers effective antimicrobial functionality, the SAP–EGS hydrogel provides an economical and environmentally friendly approach for chloride mitigation. Together, these materials contribute to the development of multifunctional treatment technologies that support circular-economy principles by utilizing renewable and waste-derived resources while addressing emerging freshwater quality challenges.

4.2. Future Work

Although promising results were achieved, several opportunities exist to further improve the developed materials and expand their practical applications.

For the BC–NF composite, future studies should investigate the mechanism of nanoflower nucleation and growth on the biochar surface to better understand how biochar properties influence nanoflower morphology, distribution, and stability. Optimizing synthesis parameters such as precursor concentration, pH, reaction time, and temperature may improve nanoflower loading and enhance adsorption performance. Surface modification of biochar before nanoflower growth may

also increase the density and uniformity of nanoflower formation. In addition, the antimicrobial activity should be evaluated against a broader range of pathogenic microorganisms, and the long-term stability and potential copper ion release should be investigated under different environmental conditions.

As detailed in Appendix A, biochar-based materials were investigated as an additional approach for chloride removal. While their chloride-removal performance was limited, the subsequent development of biochar-supported nanoflowers (BC-NFs) demonstrated promising antimicrobial activity. These findings highlight the potential of biochar-based functional materials for multifunctional water-treatment applications beyond chloride removal. However, further studies are recommended to explore the modification and functionalization of biochar to enhance its chloride-removal capacity and improve its applicability for chloride-contaminated water treatment.

Future work should focus on scaling up the SAP–EGS system from laboratory-scale batch experiments to continuous-flow column systems and pilot-scale treatment units. Its hydraulic performance, long-term durability, regeneration, and operational costs should then be evaluated under realistic environmental conditions using natural surface water with varying water chemistry. A comprehensive techno-economic analysis and life-cycle assessment would provide valuable information regarding the commercial feasibility and environmental sustainability of the technology.

For the SAP–EGS composite, future research should extend its application beyond chloride removal to other environmentally significant contaminants, including phosphate, nitrate, sulfate, fluoride, heavy metals, and emerging contaminants. The simultaneous removal of multiple pollutants from complex wastewater matrices should also be investigated. Since methanol was

used to facilitate water release from the swollen hydrogel, environmentally safer and more sustainable alternatives should be explored to improve the practicality and environmental compatibility of the process. Further optimization of the SAP formulation and EGS content may enhance adsorption capacity, mechanical strength, and regeneration efficiency.

Finally, integrating multifunctional materials such as BC–NFs with SAP-based composites may offer a promising strategy for simultaneously achieving microbial disinfection and contaminant removal, leading to the development of next-generation sustainable materials for integrated water treatment applications.

References:

Adimas, Z. T. (2026). Effect of eggshell powder incorporation on the physical and mechanical properties of potato-based edible films. Next Research, 9, 101734. https://doi.org/10.1016/j.nexres.2026.101734

Ahmad, A., Khan, Z. U. H., Sabahat, S., Sun, J., Shah, N. S., Khan, Z. U., Muhammad, N., Mir, S., Rahim, A., Nadeem, M., & Khasim, S. (2024). Innovations in metal oxides-biochar nanoparticles for dye removal. In Nano-Structures and Nano-Objects (Vol. 39). Elsevier B.V. https://doi.org/10.1016/j.nanoso.2024.101269

Ahmed, E. M. (2015). Hydrogel: Preparation, characterization, and applications: A review. In Journal of Advanced Research (Vol. 6, Number 2, pp. 105–121). Elsevier B.V. https://doi.org/10.1016/j.jare.2013.07.006

Alamdari, A., & Saffari, M. (2012). Kinetic study of calcium carbonate precipitation in gas field brine containing methanol. Journal of Natural Gas Science and Engineering, 5, 17–24. https://doi.org/10.1016/j.jngse.2011.10.003

Alobaidi, R., & Rahmah, M. I. (2026). A facile method to prepare NiO/Cu2O nanoflowers with antibacterial activity. Next Nanotechnology, 9. https://doi.org/10.1016/j.nxnano.2026.100490

An, Z., Sánchez-Montes, I., Chelme-Ayala, P., Chen, C., & Gamal El-Din, M. (2024). Efficient degradation of naphthenic acids in water using a sustainable engineered biochar/ZnO composite under simulated solar light. Chemical Engineering Journal, 489. https://doi.org/10.1016/j.cej.2024.151308

Ansari, S., Bello-Mendoza, R., O'Sullivan, A., Basharat, S., & Barker, D. (2025). Nitrate and phosphate removal from water using a novel cellulose-based anion exchange hydrogel. Environmental Technology and Innovation, 39. https://doi.org/10.1016/j.eti.2025.104289

Aydin, D., Gübbük, İ. H., & Ersöz, M. (2024). Recent advances and applications of nanostructured membranes in water purification. In Turkish Journal of Chemistry (Vol. 48, Number 1, pp. 1–20). TUBITAK. https://doi.org/10.55730/1300-0527.3635

Batara, B., Steven, S., Mulyana, M., Saputra, A. S., Hutahaean, A. C., Yemensia, E. V., Soekotjo, E. S. A., Abidin, A. Z., & Graha, H. P. R. (2025). Recent Advances, Applications, and Challenges in Superabsorbent Polymers to Support Water Sustainability. In Journal of Applied Polymer Science (Vol. 142, Number 11). John Wiley and Sons Inc. https://doi.org/10.1002/app.56588

Bjorge, D., Daels, N., De Vrieze, S., Dejans, P., Van Camp, T., Audenaert, W., Hogie, J., Westbroek, P., De Clerck, K., & Van Hulle, S. W. H. (2009). Performance assessment of electrospun nanofibers for filter applications. Desalination, 249(3), 942–948. https://doi.org/https://doi.org/10.1016/j.desal.2009.06.064

Bombuwala Dewage, N., Fowler, R. E., Pittman, C. U., Mohan, D., & Mlsna, T. (2018). Lead (Pb2+) sorptive removal using chitosan-modified biochar: Batch and fixed-bed studies. RSC Advances, 8(45), 25368–25377. https://doi.org/10.1039/c8ra04600j

Bour, A., Mouchet, F., Silvestre, J., Gauthier, L., & Pinelli, E. (2015). Environmentally relevant approaches to assess nanoparticles ecotoxicity: A review. In Journal of Hazardous Materials (Vol. 283, pp. 764–777). Elsevier. https://doi.org/10.1016/j.jhazmat.2014.10.021

Brunelli, A., Calgaro, L., Semenzin, E., Cazzagon, V., Giubilato, E., Marcomini, A., & Badetti, E. (2021). Leaching of nanoparticles from nano-enabled products for the protection of cultural heritage surfaces: a review. In Environmental Sciences Europe (Vol. 33, Number 1). Springer Science and Business Media Deutschland GmbH. https://doi.org/10.1186/s12302-021-00493-z

Cairone, S., Hasan, S. W., Choo, K. H., Li, C. W., Zarra, T., Belgiorno, V., & Naddeo, V. (2024). Integrating artificial intelligence modeling and membrane technologies for advanced wastewater treatment: Research progress and future perspectives. Science of the Total Environment, 944. https://doi.org/10.1016/j.scitotenv.2024.173999

Chandrappa, R., & Kamath, S. (2021). The Egg shell as a filler in composite materials - a review. Journal of Mechanical and Energy Engineering, 4, 335–340. https://doi.org/10.30464/jmee.2020.4.4.335

Chen, C., Luo, L., Song, S., Chen, Y., Wang, J., Gao, C., Huang, F., & Xue, L. (2025). Self-assembled nanoflower-mediated interfacial polymerization through tunable intra- and inter-layer channels to boost total heat exchange performance. Journal of Membrane Science, 715. https://doi.org/10.1016/j.memsci.2024.123448

Cui, J., & Jia, S. (2017). Organic–inorganic hybrid nanoflowers: A novel host platform for immobilizing biomolecules. In Coordination Chemistry Reviews (Vol. 352, pp. 249–263). Elsevier B.V. https://doi.org/10.1016/j.ccr.2017.09.008

Dadi, S., Celik, C., & Ocsoy, I. (2020). Gallic acid nanoflower immobilized membrane with peroxidase-like activity for m-cresol detection. Scientific Reports, 10(1). https://doi.org/10.1038/s41598-020-73778-7

Dai, B., Ding, Y., Chen, C., Shen, L., Zhao, D. L., Jiao, Y., Lin, H., & Xu, Y. (2024). Super-hydrophilic membranes fabricated by synergistic integration of covalent organic framework nanoflowers and hydrophilic layers for efficient oil-water separation. Desalination, 592, 118095. https://doi.org/https://doi.org/10.1016/j.desal.2024.118095

Dai, B., Hu, Y., Ding, Y., Shen, L., Li, R., Zhao, D., Jiao, Y., Xu, Y., & Lin, H. (2024a). Innovative construction of nano-wrinkled polyamide membranes using covalent organic framework nanoflowers for efficient desalination and antibiotic removal. Desalination, 570. https://doi.org/10.1016/j.desal.2023.117083

Deng, Y., Zhang, W., Ma, C., Li, C., Hong, Y., Sun, Y., Niu, J., Guo, S., & Yao, S. (2025). Self-assembled MoS2 nanoflowers decorated nitrogen/phosphorous/fluorine heteroatoms co-doped carbon nanotubes as enhanced catalyst for Li-CO2 batteries. Journal of Energy Storage, 113. https://doi.org/10.1016/j.est.2025.115640

Di, J., Wang, H., Zhang, L., Chen, Z., Zhang, Y., Mamba, B. B., Qiu, M., Guo, J., & Shao, L. (2024). Recent progress in advanced polyamide nanofiltration membranes via interfacial polymerization for desalination and beyond. In Desalination (Vol. 592). Elsevier B.V. https://doi.org/10.1016/j.desal.2024.118167

Di, L., Zhang, M., Jiang, Y., Yan, X., Yan, Y., Pan, J., Moradian, J. M., & Shahnavaz, Z. (2024). Electrostatically assembled nanoflower-like MXene/NiCu-layered double hydroxide composite thin-film: A high capacitive energy storage for flexible supercapacitors. Surfaces and Interfaces, 53. https://doi.org/10.1016/j.surfin.2024.105070

Ekata, D., Ankush Salunkhe, K., & Rajendra Shedage, A. (n.d.). Review on Nanoflowers (Vol. 2, Number 2). Retrieved http://e-currentscience.com/journal/e/CTPPC

El-Kattan, N., Ibrahim, M. A., Emam, A. N., Metwally, K., Youssef, F. S., Nassar, N. A., & Mansour, A. S. (2025). Evaluation of the antimicrobial activity of chitosan- and curcumin-capped copper oxide nanostructures against multi-drug-resistant microorganisms. Nanoscale Advances, 7(10), 2988–3007. https://doi.org/10.1039/d4na00955j

Environment and Climate Change Canada. Code of Practice for the Environmental Management of Road Salts: Annual Overview of Data Reported (2019–2024) in the Context of National Targets. Gatineau, QC, Canada; 2025. (n.d.).

Foller, T., Wen, X., Khine, Y. Y., Ji, D., Gupta, T., Muller, M., Scret, C., & Joshi, R. (2023). Removal of chlorine and monochloramine from tap water using graphene oxide membranes. Journal of Membrane Science, 686. https://doi.org/10.1016/j.memsci.2023.122022

Gao, C., Tan, W., Liang, B., Guo, Y., Xing, Y., & Ji, S. (2025). Ultrahigh antifouling ultrafiltration membrane based on Ag NPs photoreduction modified PVP/BiOCl nanoflower for efficient membrane fouling removal. Environmental Research, 270. https://doi.org/10.1016/j.envres.2025.120842

García-Ávila, F., Zambrano-Jaramillo, A., Velecela-Garay, C., Coronel-Sánchez, K., & Valdiviezo-Gonzalez, L. (2024). Effectiveness of membrane technologies in removing emerging contaminants from wastewater: Reverse Osmosis and Nanofiltration. Water Cycle. https://doi.org/10.1016/j.watcyc.2024.12.004

Ge, J., Lei, J., & Zare, R. N. (2012a). Protein-inorganic hybrid nanoflowers. Nature Nanotechnology, 7(7), 428–432. https://doi.org/10.1038/nnano.2012.80

Gunasekaran, S., & Anbalagan, G. (2007). Spectroscopic characterization of natural calcite minerals. Spectrochimica Acta Part A: Molecular and Biomolecular Spectroscopy, 68(3), 656–664. https://doi.org/https://doi.org/10.1016/j.saa.2006.12.043

Gunasekaran, S., Anbalagan, G., & Pandi, S. (2006). Raman and infrared spectra of carbonates of calcite structure. Journal of Raman Spectroscopy, 37(9), 892–899. https://doi.org/https://doi.org/10.1002/jrs.1518

Guo, W., Yan, X., Lu, Q., Zheng, A., Wang, J., Jiang, N., Wang, W., Li, G., Liu, L., Li, G., Li, H., & Ren, Z. (2025). Mo-modified NiFe LDH nanoflower anode catalyst synthesized via a top-down etching method for anion exchange membrane water electrolysis. International Journal of Hydrogen Energy, 145, 237–249. https://doi.org/10.1016/j.ijhydene.2025.05.409

Gwon, K., Park, J. D., Lee, S., Yu, J. S., & Lee, D. N. (2024). Fabrication of silicon-based nickel nanoflower-encapsulated gelatin microspheres as an active antimicrobial carrier. International Journal of Biological Macromolecules, 264. https://doi.org/10.1016/j.ijbiomac.2024.130617

Hang, Z., Zhou, L., Bian, X., Liu, G., Cui, F., Du, H., & Wen, Y. (2024). Potential application of aptamers combined with DNA nanoflowers in neurodegenerative diseases. In Ageing Research Reviews (Vol. 100). Elsevier Ireland Ltd. https://doi.org/10.1016/j.arr.2024.102444

Hassan, S. S. M., El-Shalakany, H. H., Fathy, M. A., & Kamel, A. H. (2024). A magnetic macroporous α-Fe2O3/Mn2O3 nanocomposite as an efficient adsorbent for simple and rapid removal of Pb(II) from wastewater and electronic waste leachate. Environmental Science and Pollution Research, 31(57), 65648–65660. https://doi.org/10.1007/s11356-024-35452-7

Hassan, S. S. M., Fathy, M. A., El-Aswar, E. I., Ibrahim, S. S., Ismael, A. M., Yehia, M. M., & Rashad, M. M. (2026). A novel magnetic AC/bentonite/Fe3O4/CeO2nanocomposite catalyst for photocatalytic degradation of persistent chlorinated pesticides in water. RSC Advances, 16(14), 12713–12724. https://doi.org/10.1039/d5ra09280a

Hassan, S. S. M., Mohamed, N. R. G., Saad, M. M. A., Salem, A. M., Ibrahim, Y. H., Elshakour, A. A., & Fathy, M. A. (2025). A novel non-woven fabric sandwich filter with activated carbon/polypyrrole nanocomposite for the removal of CO, SO2 and NOx emitted from gasoline engines. Fuel, 401. https://doi.org/10.1016/j.fuel.2025.135838

Hintz, W. D., & Relyea, R. A. (2019). A review of the species, community, and ecosystem impacts of road salt salinisation in fresh waters. In Freshwater Biology (Vol. 64, Number 6, pp. 1081–1097). John Wiley and Sons Inc. https://doi.org/10.1111/fwb.13286

Ignacz, G., Bader, L., Beke, A. K., Ghunaim, Y., Shastry, T., Vovusha, H., Carbone, M. R., Ghanem, B., & Szekely, G. (2025). Machine learning for the advancement of membrane science and technology: A critical review. In Journal of Membrane Science (Vol. 713). Elsevier B.V. https://doi.org/10.1016/j.memsci.2024.123256

Imteyaz, S., Maheshwari, A., & Rafiuddin. (2025). An outlook on membranes: Types, synthesis, and application in membrane technology. In Hybrid Advances (Vol. 8). Elsevier B.V. https://doi.org/10.1016/j.hybadv.2024.100351

Ishaq, M., Chhipa, R. C., Sharma, A., & Ali, G. (2025). Evaluation of adsorption isotherms and kinetics of chloride ion in water using biochar derived from locally available agro-waste. Environmental Research and Technology, 8(2), 288–296. https://doi.org/10.35208/ert.1491915

Izadi, A., Hosseini, M., Darzi, G. N., Bidhendi, G. N., & Shariati, F. P. (2019). Performance of an integrated fixed bed membrane bioreactor (FBMBR) applied to pollutant removal from paper-recycling wastewater. Water Resources and Industry, 21, 100111. https://doi.org/https://doi.org/10.1016/j.wri.2019.100111

Jafari-Nodoushan, H., Mojtabavi, S., Faramarzi, M. A., & Samadi, N. (2022a). Organic-inorganic hybrid nanoflowers: The known, the unknown, and the future. In Advances in Colloid and Interface Science (Vol. 309). Elsevier B.V. https://doi.org/10.1016/j.cis.2022.102780

Jiang, L., Zhang, J., Li, H., He, C., Yuan, R., Zhao, Y., Huang, J. A., Zhuo, Y., & Yang, X. (2023). Band gap tuning of Sn1-xCexO2 nanoflower for improved SERS activity of bioassay. Chemical Engineering Journal, 461. https://doi.org/10.1016/j.cej.2023.142102

Jin, Z.-F., Asako, Y., Yamaguchi, Y., & Yoshida, H. (n.d.). Thermal and water storage characteristics of super-absorbent polymer gel which absorbed aqueous solution of calcium chloride. Retrieved www.elsevier.com/locate/ijhmt

Kamali, M., Appels, L., Kwon, E. E., Aminabhavi, T. M., & Dewil, R. (2021). Biochar in water and wastewater treatment - a sustainability assessment. In Chemical Engineering Journal (Vol. 420). Elsevier B.V. https://doi.org/10.1016/j.cej.2021.129946

Kang, D. J., Pal, K., Park, S. J., Bang, D. S., & Kim, J. K. (2010). Effect of eggshell and silk fibroin on styrene-ethylene/butylene-styrene as bio-filler. Materials and Design, 31(4), 2216–2219. https://doi.org/10.1016/j.matdes.2009.10.033

Kanth, M. S., Sandhya Rani, S. L., & Raja, V. K. (2025). Advancing ceramic membrane technology in chemical industries applications by evaluating cost-effective materials, fabrication and surface modification methods. In Hybrid Advances (Vol. 8). Elsevier B.V. https://doi.org/10.1016/j.hybadv.2025.100380

Kataria, N., & Garg, V. K. (2018). Optimization of Pb (II) and Cd (II) adsorption onto ZnO nanoflowers using central composite design: isotherms and kinetics modelling. Journal of Molecular Liquids, 271, 228–239. https://doi.org/10.1016/j.molliq.2018.08.135

Kaur, M., & Kaur, H. (2022a). Synergistic effect of biochar impregnated with ZnO nano-flowers for effective removal of organic pollutants from wastewater. Applied Surface Science Advances, 12. https://doi.org/10.1016/j.apsadv.2022.100339

Khor, Y., Aziz, A. R. A., & Chong, S. S. (2024). Recent developments and sustainability in monitoring chlorine residuals for water quality control: a critical review. In RSC Sustainability (Vol. 2, Number 9, pp. 2468–2485). Royal Society of Chemistry. https://doi.org/10.1039/d4su00188e

Khraisheh, M., Elhenawy, S., Almomani, F., Al-Ghouti, M., Hassan, M. K., & Hameed, B. H. (2021). Recent progress on nanomaterial-based membranes for water treatment. In Membranes (Vol. 11, Number 12). MDPI. https://doi.org/10.3390/membranes11120995

Kim, J., & Rhee, J. Il. (2023). Preparation and characterization of optical temperature-sensing membranes based on various fluorescent material-doped polyacrylonitrile nanoflowers. Optical Materials, 140. https://doi.org/10.1016/j.optmat.2023.113847

Koca, F. D., Demirezen Yilmaz, D., Ertas Onmaz, N., & Ocsoy, I. (2020). Peroxidase-like activity and antimicrobial properties of curcumin-inorganic hybrid nanostructure. Saudi Journal of Biological Sciences, 27(10), 2574–2579. https://doi.org/10.1016/j.sjbs.2020.05.025

Kong, P., Sun, Z., Gui, H., Chen, Z., Song, Y., Wang, Y., Wang, Y., Kipper, M. J., Tang, J., & Huang, L. (2024). Advances in the application of graphene oxide composite loose nanofiltration membranes for dye and salt separation. In Journal of Environmental Chemical Engineering (Vol. 12, Number 6). Elsevier Ltd. https://doi.org/10.1016/j.jece.2024.114278

Kühnel, D., & Nickel, C. (2014). The OECD expert meeting on ecotoxicology and environmental fate - Towards the development of improved OECD guidelines for the testing of nanomaterials. Science of the Total Environment, 472, 347–353. https://doi.org/10.1016/j.scitotenv.2013.11.055

Lead, J. R., Batley, G. E., Alvarez, P. J. J., Croteau, M. N., Handy, R. D., McLaughlin, M. J., Judy, J. D., & Schirmer, K. (2018). Nanomaterials in the environment: Behavior, fate, bioavailability, and effects—An updated review. In Environmental Toxicology and Chemistry (Vol. 37, Number 8, pp. 2029–2063). Wiley Blackwell. https://doi.org/10.1002/etc.4147

Lee, D. N., Gwon, K., Yu, J.-H., Kim, Y. R., Park, G., Han, I., Lee, S. J., Shin, J. H., & Yu, J.-S. (2023). Intracellular NO Delivery by Si-Based Ni Composite Nanoflowers. ACS Applied Nano Materials, 6(2), 846–855. https://doi.org/10.1021/acsanm.2c03960

Lee, S. Y., Tan, Y. H., Lau, S. Y., Mubarak, N. M., Tan, Y. Y., Tan, I. S., Lee, Y. H., Ibrahim, M. L., Karri, R. R., Khalid, M., Chan, Y. S., & Adeoye, J. B. (2024a). A state-of-the-art review of metal oxide nanoflowers for wastewater treatment: Dye removal. In Environmental Research (Vol. 259). Academic Press Inc. https://doi.org/10.1016/j.envres.2024.119448

Lee, S. Y., Tan, Y. H., Lau, S. Y., Mubarak, N. M., Tan, Y. Y., Tan, I. S., Lee, Y. H., Ibrahim, M. L., Karri, R. R., Khalid, M., Chan, Y. S., & Adeoye, J. B. (2024b). A state-of-the-art review of metal oxide nanoflowers for wastewater treatment: Dye removal. In Environmental Research (Vol. 259). Academic Press Inc. https://doi.org/10.1016/j.envres.2024.119448

Lee, Y. Y., Chang-Chien, G. P., Li, I. C., Huang, B. W., Nguyen, M. K., Pham, M. T., & Wu, C. H. (2024). Advanced ceramic membranes: Novel strategies for sulfamethoxazole removal in wastewater treatment. In Journal of Environmental Chemical Engineering (Vol. 12, Number 6). Elsevier Ltd. https://doi.org/10.1016/j.jece.2024.114674

Li, M., Luo, M., Li, F., Wang, W., Liu, K., Liu, Q., Wang, Y., Lu, Z., & Wang, D. (2016). Biomimetic Copper-Based Inorganic-Protein Nanoflower Assembly Constructed on the Nanoscale Fibrous Membrane with Enhanced Stability and Durability. Journal of Physical Chemistry C, 120(31), 17348–17356. https://doi.org/10.1021/acs.jpcc.6b03537

Li, S., Tian, S., Wu, J., Zhou, P., He, Y., & Guo, X. (2023). Nanoflower-branched layered double hydroxide (LDH)-wrapped electrospun membrane synthesized with ZIF-67 templates for oil-containing emulsified wastewater separation. Journal of Membrane Science, 685. https://doi.org/10.1016/j.memsci.2023.121957

Li, T., Li, R., Luo, H., Peng, L., Wang, J., Li, S., Zhou, M., Yuan, X., Zhang, Z., & Wu, H. (2024). Eggshell powder as a bio-filler for starch and gelatin: Ternary biodegradable composite films manufactured by extrusion compression molding. Food Hydrocolloids, 150. https://doi.org/10.1016/j.foodhyd.2023.109632

Li, T., Tong, Z., Gao, B., Li, Y. C., Smyth, A., & Bayabil, H. K. (2020). Polyethyleneimine-modified biochar for enhanced phosphate adsorption. Environmental Science and Pollution Research, 27(7), 7420–7429. https://doi.org/10.1007/s11356-019-07053-2

Li, X., Zhou, H., Wang, L., Wang, H., Adili, A., Li, J., & Zhang, J. (2023). SERS paper sensor based on three-dimensional ZnO@Ag nanoflowers assembling on polyester fiber membrane for rapid detection of florfenicol residues in chicken. Journal of Food Composition and Analysis, 115. https://doi.org/10.1016/j.jfca.2022.104911

Li, Y., Ma, S., Xu, S., Fu, H., Li, Z., Li, K., Sheng, K., Du, J., Lu, X., Li, X., & Liu, S. (2020). Novel magnetic biochar as an activator for peroxymonosulfate to degrade bisphenol A: Emphasizing the synergistic effect between graphitized structure and CoFe2O4. Chemical Engineering Journal, 387. https://doi.org/10.1016/j.cej.2020.124094

Li, Y., Wang, X., Ren, L., Dai, R., Qiu, Z., Zhou, H., & Wang, Z. (2025). Membrane modification strategies for virus removal from water. In iScience (Vol. 28, Number 3). Elsevier Inc. https://doi.org/10.1016/j.isci.2025.111944

Li, Y., Yang, Z., Yang, K., Wei, J., Li, Z., Ma, C., Yang, X., Wang, T., Zeng, G., Yu, G., Yu, Z., & Zhang, C. (2022). Removal of chloride from water and wastewater: Removal mechanisms

and recent trends. In Science of the Total Environment (Vol. 821). Elsevier B.V. https://doi.org/10.1016/j.scitotenv.2022.153174

Li, Z., Davar, F., Chen, J., Li, Z., & Fang, X. (2020). CdS/CdSO4 Nanoflower-Based Photodetector with Enhanced Photoelectric Performances. ACS Applied Nano Materials, 3(10), 10190–10199. https://doi.org/10.1021/acsanm.0c02166

Liang, H., Kong, H., Min, Y., Wang, Y., Ma, Y., Sun, H., Wang, Y., & Zheng, Y. (2024). Construction of Ultrathin CuAuAg Nanosheet-Assembled Three-Dimensional Nanoflowers for Photothermal Conversion and Electrocatalytic Hydrogen Evolution. ACS Applied Nano Materials, 7(15), 17987–17995. https://doi.org/10.1021/acsanm.4c03360

Liang, L., Lu, D., Qin, Y., Chen, J., & Zhang, L. (2025). Machine learning in membrane science: Bridging materials, structures, and performance for next-generation membrane design. In Separation and Purification Technology (Vol. 369). Elsevier B.V. https://doi.org/10.1016/j.seppur.2025.133091

Liu, M., Yu, F., Niu, L., & Chi, H. (2025). Advances in nanofiltration membrane pore size adjustment techniques: A review. Environmental Functional Materials. https://doi.org/10.1016/j.efmat.2025.02.002

Liu, X., Sui, B., Camargo, P. H. C., Wang, J., & Sun, J. (2021). Tuning band gap of MnO2 nanoflowers by Alkali metal doping for enhanced Ferroptosis/phototherapy synergism in Cancer. Applied Materials Today, 23. https://doi.org/10.1016/j.apmt.2021.101027

Liu, X., & Yue, Y. (2024). Phosphate adsorption from phosphorus-polluted wastewater by peanut hull-derived biochar functionalized with eggshell-based calcium chloride: preparation, adsorption performance and mechanism. Desalination and Water Treatment, 320. https://doi.org/10.1016/j.dwt.2024.100880

Liu, Y., Dai, X., Li, J., Cheng, S., Zhang, J., & Ma, Y. (2024a). Recent progress in TiO2-biochar-based photocatalysts for water contaminants treatment: strategies to improve photocatalytic performance. In RSC Advances (Vol. 14, Number 1, pp. 478–491). Royal Society of Chemistry. https://doi.org/10.1039/d3ra06910a

Liu, Y., Dai, X., Li, J., Cheng, S., Zhang, J., & Ma, Y. (2024b). Recent progress in TiO2-biochar-based photocatalysts for water contaminants treatment: strategies to improve photocatalytic performance. In RSC Advances (Vol. 14, Number 1, pp. 478–491). Royal Society of Chemistry. https://doi.org/10.1039/d3ra06910a

Liu, Y., Zhu, J., Chi, M. S., Eygen, G. Van, Guan, K., & Matsuyama, H. (2025). Comprehensive review of nanofiltration membranes for efficient resource recovery from textile wastewater. In Chemical Engineering Journal (Vol. 506). Elsevier B.V. https://doi.org/10.1016/j.cej.2025.160132

Luo, M., Li, M., Jiang, S., Shao, H., Razal, J., Wang, D., & Fang, J. (2020). Supported growth of inorganic-organic nanoflowers on 3D hierarchically porous nanofibrous membrane for enhanced enzymatic water treatment. Journal of Hazardous Materials, 381. https://doi.org/10.1016/j.jhazmat.2019.120947

Manholi, S., & Athiyanathil, S. (2024). Eco-friendly poly (ε-caprolactone) based Microfiltration polymeric membranes - influence of dope composition on morphology and performance concerning oil-water separation. Journal of Polymer Research, 31(12). https://doi.org/10.1007/s10965-024-04212-z

Manikandan, R., Abbas, S. M., Sathish, S., Ahamed, J. I., Ahamed, A. T., Miandad, M. K. J., & Thovheed, S. Z. (2021). Experimental analysis of basalt fiber reinforced egg shell/water hyacinth loaded epoxy composites. Materials Today: Proceedings, 45, 1660–1663. https://doi.org/10.1016/j.matpr.2020.08.557

Mankomal, Kaur, H., & Roy, T. (2024). Sustainable removal of organic pollutants using biochar based ZnO composites: Experimental and theoretical studies of remediation process. In Surfaces and Interfaces (Vol. 49). Elsevier B.V. https://doi.org/10.1016/j.surfin.2024.104399

Mannina, G., Ekama, G. A., Capodici, M., Cosenza, A., Di Trapani, D., & Ødegaard, H. (2018). Integrated fixed-film activated sludge membrane bioreactors versus membrane bioreactors for nutrient removal: A comprehensive comparison. Journal of Environmental Management, 226, 347–357. https://doi.org/10.1016/j.jenvman.2018.08.006

Mijan, M. Al, Kim, D. H., & Kwak, H. S. (2014). Physicochemical properties of nanopowdered eggshell. International Journal of Food Science and Technology, 49(7), 1751–1757. https://doi.org/10.1111/ijfs.12451

Mohamad Esham, M. I., Ahmad, A. L., Othman, M. H. D., & Adam, M. R. (2025). Durable hybrid photocatalytic/microfiltration titania nanoflowers-calcium bentonite hollow fiber membrane with exceptional antifouling performance for real refinery-produced water treatment. Separation and Purification Technology, 373. https://doi.org/10.1016/j.seppur.2025.133616

Mohammadzadeh Pakdel, P., & Peighambardoust, S. J. (2018). A review on acrylic based hydrogels and their applications in wastewater treatment. In Journal of Environmental Management (Vol. 217, pp. 123–143). Academic Press. https://doi.org/10.1016/j.jenvman.2018.03.076

Nayak, D., Kumar, A., & Thangavel, R. (2023). Synthesis of MoS2 Nanoflowers for Photocatalytic Degradation of Organic Dyes. ACS Applied Nano Materials, 6(20), 19476–19490. https://doi.org/10.1021/acsanm.3c04316

Nyangi, M. J. (2024). Simultaneous removal of chloride and hardness from groundwater by cassava peel biosorption: Optimization and sorption studies. Remediation Journal, 34(1), e21770. https://doi.org/https://doi.org/10.1002/rem.21770

Owczarek, E., Rybicki, M., & Hawlicka, E. (2007). Solvation of calcium ions in methanol-water mixtures: Molecular dynamics simulation. Journal of Physical Chemistry B, 111(51), 14271–14278. https://doi.org/10.1021/jp076233v

Pervez, M. N., Balakrishnan, M., Hasan, S. W., Choo, K. H., Zhao, Y., Cai, Y., Zarra, T., Belgiorno, V., & Naddeo, V. (2020). A critical review on nanomaterials membrane bioreactor (NMS-MBR) for wastewater treatment. In npj Clean Water (Vol. 3, Number 1). Nature Research. https://doi.org/10.1038/s41545-020-00090-2

Petriev, I., Pushankina, P., Bolotin, S., Lutsenko, I., Kukueva, E., & Baryshev, M. (2021). The influence of modifying nanoflower and nanostar type Pd coatings on low temperature hydrogen permeability through Pd-containing membranes. Journal of Membrane Science, 620. https://doi.org/10.1016/j.memsci.2020.118894

Qi, T., Chen, X., Fan, Y., & Zhong, J. (2025). Ceramic membrane technology for the separation and purification of bioactive compounds: A critical review of applications, diafiltration modeling, and fouling prevention. In Separation and Purification Technology (Vol. 361). Elsevier B.V. https://doi.org/10.1016/j.seppur.2024.131301

Rahbari-Sisakht, M., & Ismail, A. F. (2025a). A comprehensive review of pressure and osmosis driven membrane processes: Processes, characteristics and materials. In Desalination (Vol. 598). Elsevier B.V. https://doi.org/10.1016/j.desal.2024.118427

Rahbari-Sisakht, M., & Ismail, A. F. (2025b). Covalent organic framework membranes for water purification: Current status and future research directions. In Separation and Purification Technology (Vol. 359). Elsevier B.V. https://doi.org/10.1016/j.seppur.2024.130759

Rahbari-Sisakht, M., Mousavian, S., Ariana, M. A., & Ismail, A. F. (2025). Thin-film nanocomposite membranes for water treatment: Evolution, applications, challenges, and advancement strategies. Journal of Environmental Chemical Engineering, 13(3). https://doi.org/10.1016/j.jece.2025.116392

Rahimi-Kashkouli, Y., Rahbari-Sisakht, M., & Ghadami Jadval Ghadam, A. (2020). Thin film nanocomposite nanofiltration membrane incorporated with cellulose nanocrystals with superior anti-organic fouling affinity. Environ. Sci.: Water Res. Technol., 6(3), 715–723. https://doi.org/10.1039/C9EW00963A

Raj, V. J., Ghosh, R., Girigoswami, A., & Girigoswami, K. (2022). Application of zinc oxide nanoflowers in environmental and biomedical science. In BBA Advances (Vol. 2). Elsevier B.V. https://doi.org/10.1016/j.bbadva.2022.100051

Sahu, L. R., Yadav, D., & Ingole, P. G. (2025). Recent developments and innovations in thin-film nanocomposite nanofiltration: The next-generation selective membrane for heavy metal ion removal from water. In Chemical Engineering Journal (Vol. 513). Elsevier B.V. https://doi.org/10.1016/j.cej.2025.162579

Samavati, Z., Goh, P. S., Fauzi Ismail, A., Lau, W. J., Samavati, A., Ng, B. C., & Sohaimi Abdullah, M. (2025). Advancements in membrane technology for efficient POME treatment: A comprehensive review and future perspectives. In Journal of Environmental Sciences (China) (Vol. 155, pp. 730–761). Chinese Academy of Sciences. https://doi.org/10.1016/j.jes.2024.11.010

Shende, P., Kasture, P., & Gaud, R. S. (2018). Nanoflowers: the future trend of nanotechnology for multi-applications. Artificial Cells, Nanomedicine, and Biotechnology, 46(sup1), 413–422. https://doi.org/10.1080/21691401.2018.1428812

Song, C., Luo, S., He, M., Zhao, X., & Sun, M. (2025). Antibacterial mechanism of water-soluble CeO2 nanoflowers and its product design in antibacterial application. Applied Surface Science, 679. https://doi.org/10.1016/j.apsusc.2024.161249

Song, G., Chen, D., Zhang, X., Wang, T., Zhang, L., Fan, F., Chen, J., Li, Y., & Fu, Y. (2021a). Direct and ultrafast preparation of Cu3(PO4)2 nanoflower by ultrasonic spray method without protein assistant and its applications: Large-scale simulation and catalytic reduction. Journal of Molecular Liquids, 328. https://doi.org/10.1016/j.molliq.2021.115348

Song, M., Zhu, L., Tian, M., Wang, L., Tao, H., Zhou, Y., & Donaev, S. (2025). Efficient removal of phthalic acid esters from water using nanofiltration membranes: Adsorption mechanisms and hydraulic factors. Surfaces and Interfaces, 72. https://doi.org/10.1016/j.surfin.2025.107250

Song, Q., Kong, F., Liu, B. F., Song, X., & Ren, H. Y. (2024). Biochar-based composites for removing chlorinated organic pollutants: Applications, mechanisms, and perspectives. In Environmental Science and Ecotechnology (Vol. 21). Editorial Board, Research of Environmental Sciences. https://doi.org/10.1016/j.ese.2024.100420

Sun, J., Wang, Y., Dong, R., Ding, W., Li, Y., & Bao, M. (2025). Review of the recent six-year chlorination resistance strategies of polyamide reverse osmosis and nanofiltration membrane. In Desalination (Vol. 601). Elsevier B.V. https://doi.org/10.1016/j.desal.2025.118540

Sun, W., Yue, D., Wang, S., Sun, D., Yin, L., & Wang, Y. (2025). Prewetting induced underwater super oleophobic hydroxyethyl cellulose-SiO2-graphene microfiltration membranes for emulsion separation. Separation and Purification Technology, 358. https://doi.org/10.1016/j.seppur.2024.130421

Sun, W., Zhang, J., Sun, D., Zhang, G., & Gong, D. (2026). Black@ZnO/Gr modified carbon fiber self-cleaning membrane for Resource Disposal of degreasing wastewater. Journal of Membrane Science, 738. https://doi.org/10.1016/j.memsci.2025.124723

Tabesh, E., Grumme, D., Herb, M., Rezai, P., Maleki, H. (Homa), & Leung, S. N. (2025). Fabrication of MXene integrated superabsorbent polymers composites hydrogels for bacterial

enrichment. Separation and Purification Technology, 368. https://doi.org/10.1016/j.seppur.2025.133022

Tabesh, E., Zabihihesari, A., Rezai, P., & Leung, S. N. (2025). In Situ Investigation of Swelling Dynamics of Acrylamide-Acrylic Acid Superabsorbent Microparticles at a Single Particle Level. Macromolecular Rapid Communications, 46(14). https://doi.org/10.1002/marc.202500014

Tanewska-Osinska, S., & Barczynska, J. (1984). Enthalpy of Solution of Calcium Chloride in Aqueous Mixtures of Methanol, Ethanol and Propan-1-01 at 298.15 K. In J. Chem. SOC., Faraday Trans. 1 (Vol. 80).

Tao, F., Zhang, Y., Cao, S., Yin, K., Chang, X., Lei, Y., Fan, R., Dong, L., Yin, Y., & Chen, X. (2018). CuS nanoflowers/semipermeable collodion membrane composite for high-efficiency solar vapor generation. Materials Today Energy, 9, 285–294. https://doi.org/10.1016/j.mtener.2018.06.003

Tran, T. K., Nguyen, M. K., Lin, C., Hoang, T. D., Nguyen, T. C., Lone, A. M., Khedulkar, A. P., Gaballah, M. S., Singh, J., Chung, W. J., & Nguyen, D. D. (2024). Review on fate, transport, toxicity and health risk of nanoparticles in natural ecosystems: Emerging challenges in the modern age and solutions toward a sustainable environment. In Science of the Total Environment (Vol. 912). Elsevier B.V. https://doi.org/10.1016/j.scitotenv.2023.169331

Vo, T. S., Lwin, K. M., & Kim, K. (2024). Recent developments of nano-enhanced composite membranes designed for water/wastewater purification—a review. In Advanced Composites and Hybrid Materials (Vol. 7, Number 4). Springer Science and Business Media B.V. https://doi.org/10.1007/s42114-024-00923-5

Wang, K., Ye, Q., Shen, Y., Wang, Y., Hong, Q., Zhang, C., Liu, M., & Wang, H. (2023). Biochar Addition in Membrane Bioreactor Enables Membrane Fouling Alleviation and Nitrogen Removal Improvement for Low C/N Municipal Wastewater Treatment. Membranes, 13(2). https://doi.org/10.3390/membranes13020194

Wang, Q., Li, Q., Li, C., Jin, Y., & Ho, J. (2026). Variation of dry and pre-soaked super absorbent polymer (SAP) on the rheology, strength and drying shrinkage of mortar. Construction and Building Materials, 518. https://doi.org/10.1016/j.conbuildmat.2026.145774

Wei, A., Li, J., Shan, M., Lv, W., Chen, J., Fu, P., Liu, Y., Xu, W., Dai, L., & Wang, H. (2023). Removal of chlorine, microparticles and water from high-viscosity liquids by a sand filter coupling hydrocyclone. Process Safety and Environmental Protection, 170, 636–646. https://doi.org/10.1016/j.psep.2022.12.020

Wei, J., Nian, P., Wang, Y., Wang, X., Wang, Y., Xu, N., & Wei, Y. (2022). Preparation of superhydrophobic-superoleophilic ZnO nanoflower@SiC composite ceramic membranes for

water-in-oil emulsion separation. Separation and Purification Technology, 292. https://doi.org/10.1016/j.seppur.2022.121002

Weidner, E., Karbassiyazdi, E., Altaee, A., Jesionowski, T., & Ciesielczyk, F. (2022). Hybrid Metal Oxide/Biochar Materials for Wastewater Treatment Technology: A Review. In ACS Omega (Vol. 7, Number 31, pp. 27062–27078). American Chemical Society. https://doi.org/10.1021/acsomega.2c02909

Wen, T., Zheng, Y., Wang, H., & Zou, J. (2025). Constructing black phosphorus nanosheet/CoNiSe2 nanoflower heterojunction with effective built-in electric field for robust H2 evolution in anion exchange membrane water electrolyzer. Applied Catalysis B: Environmental, 378. https://doi.org/10.1016/j.apcatb.2025.125588

Widiyandari, H., Pratama, E., Parasdila, H., Suryana, R., Arutanti, O., & Astuti, Y. (2023). Synthesis of ZnO-Cdots nanoflower by hydrothermal method for antibacterial agent and dye photodegradation catalyst. Results in Materials, 20, 100491. https://doi.org/10.1016/j.rinma.2023.100491

Witoon, T., Numpilai, T., Phongamwong, T., Donphai, W., Boonyuen, C., Warakulwit, C., Chareonpanich, M., & Limtrakul, J. (2018). Enhanced activity, selectivity and stability of a CuO-ZnO-ZrO2 catalyst by adding graphene oxide for CO2 hydrogenation to methanol. Chemical Engineering Journal, 334, 1781–1791. https://doi.org/10.1016/j.cej.2017.11.117

Wu, T., Yang, Y., Cao, Y., Song, Y., Xu, L.-P., Zhang, X., & Wang, S. (2018). Bioinspired DNA–Inorganic Hybrid Nanoflowers Combined with a Personal Glucose Meter for Onsite Detection of miRNA. ACS Applied Materials & Interfaces, 10(49), 42050–42057. https://doi.org/10.1021/acsami.8b15917

Xiong, B., Loss, R. D., Shields, D., Pawlik, T., Hochreiter, R., Zydney, A. L., & Kumar, M. (2018). Polyacrylamide degradation and its implications in environmental systems. In npj Clean Water (Vol. 1, Number 1). Nature Research. https://doi.org/10.1038/s41545-018-0016-8

Xu, H., Xu, L., & Ahmed, A. (2023). Carbon quantum dots-decorated ZnO heterostructure nanoflowers grown on nanofiber membranes as high-efficiency photocatalysts. Diamond and Related Materials, 136. https://doi.org/10.1016/j.diamond.2023.109972

Xu, W., Liang, J., Li, J., Pillai, S. C., Liang, F., Li, M., Xiao, K., Li, J., Wang, Y., Jiang, X., Liu, Z., Beiyuan, J., & Wang, H. (2024). Biochar encapsulated metal nanoflowers for high efficient degradation of metronidazole via peroxymonosulfate activation. Separation and Purification Technology, 328. https://doi.org/10.1016/j.seppur.2023.125081

Ye, H., Zhang, J., Yang, G., Jiao, R., Han, S., Lv, J., Zhang, Y. Z., Zhao, L., Xin, Q., Lin, L., Ding, X., & Li, H. (2024). Hierarchical biocatalytic membranes embedded with trypsin–inorganic hybrid nanoflowers for effective β-lactoglobulin hydrolysis. Colloids and Surfaces A:

Physicochemical and Engineering Aspects, 699. https://doi.org/10.1016/j.colsurfa.2024.134706

Yilmaz, S. G., Demirbas, A., Karaagac, Z., Dadi, S., Celik, C., Yusufbeyoglu, S., Ildiz, N., Mandal, A. K., Cimen, B., & Ocsoy, I. (2022). Synthesis of taurine-Cu3(PO4)2 hybrid nanoflower and their peroxidase-mimic and antimicrobial properties. Journal of Biotechnology, 343, 96–101. https://doi.org/10.1016/j.jbiotec.2021.11.009

Yin, H., Zhang, Q., Hu, S., Sun, X., Peng, L., Zhao, H., Kong, Q., Mitomo, H., Matsuo, Y., Ijiro, K., & Wang, G. (2024). Hierarchical Au Nanoflowers Formed in an Ionic Liquid/Water System for Bacterial Inhibition. ACS Applied Nano Materials, 7(14), 16998–17008. https://doi.org/10.1021/acsanm.4c03100

Yin, J. kun, Zhang, C., Ding, S. ying, Du, H., Tan, Z. liang, Li, M. min, Wang, B., & Wang, T. (2025). The strategies to improve the interfacial compatibility in mixed-matrix membranes: A review. In Materials Today Energy (Vol. 49). Elsevier Ltd. https://doi.org/10.1016/j.mtener.2025.101811

Yin, J., Yan, G., Lv, Y., Zheng, H., Hou, Y., Chen, S., Dang, J., & Zhu, C. (2023). Study on neutron shielding performance of high strength mortar modified by saturated super absorbent polymer. Construction and Building Materials, 409. https://doi.org/10.1016/j.conbuildmat.2023.133841

Yıldırım, M., Aminzai, M. T., & Yabalak, E. (2025). Nanoflowers: A multifunctional nanomaterial revolutionizing medicine, environmental protection, and sustainable agriculture. Inorganic Chemistry Communications, 177, 114311. https://doi.org/https://doi.org/10.1016/j.inoche.2025.114311

Yu, M., Dong, R. H., Yan, X., Yu, G. F., You, M. H., Ning, X., & Long, Y. Z. (2017). Recent Advances in Needleless Electrospinning of Ultrathin Fibers: From Academia to Industrial Production. In Macromolecular Materials and Engineering (Vol. 302, Number 7). Wiley-VCH Verlag. https://doi.org/10.1002/mame.201700002

Yu, Y., Meng, R., Jin, Z., & Zhang, X. (2026). Super absorbent polymer-modified coconut fiber (SMCF): Its preparation, microstructure and effect on cement mortar strength and shrinkage properties. Construction and Building Materials, 509. https://doi.org/10.1016/j.conbuildmat.2026.145261

Zhang, J., Zhang, Z., Wang, X., Ma, Y., Zhou, Z., Du, X., & Lu, X. (2024). Ultra-thin FeCoNi-LDH hollow nanoflower as solid-phase microextraction coating for targeted capture of six pesticides by electrostatic adsorption. Talanta, 276. https://doi.org/10.1016/j.talanta.2024.126258

Zhang, W., Xu, Y., Wang, Y., Wu, X., Liu, X., Guo, F., Wu, Q., Li, C., & Chen, M. (2024). Double Z-Scheme Heterojunctions of CdS and ZnS Nanoparticles on Bimetallic Metal–Organic

Frameworks for Photocatalytic H2 Production. ACS Applied Nano Materials, 7(18), 21993–22001. https://doi.org/10.1021/acsanm.4c04005

Zhao, J., Li, P., Zhang, Q., Ye, Z., Wang, Y., Tian, J., Xu, Z., Peng, N., Ren, H., & Zhang, X. (2024). MOF nanoflowers-based flexible portable NO sensors for human airway inflammation detection. Chemical Engineering Journal, 499. https://doi.org/10.1016/j.cej.2024.156184

Zhao, P., Hu, Y., An, X., Ji, R., Liu, H., Zhao, H., Song, W., Dong, Y., & Wang, X. (2023). Polymeric PDI-based photocatalytic nanoarchitectures promoting the performance of thin film composite membrane for forward osmosis water purification. Chemical Engineering Journal, 476. https://doi.org/10.1016/j.cej.2023.146747

Zhou, R., Cai, R., Chen, Y., Qiao, J., Ding, K., Tan, X., Ding, M., & Chen, Y. (2025). Research progress on the application of hydrogel adsorbent materials in wastewater treatment: A review. In Chemical Engineering Research and Design (Vol. 216, pp. 1–24). Institution of Chemical Engineers. https://doi.org/10.1016/j.cherd.2025.02.025

Zhou, Y., Zhao, H. jian, Ma, F., Li, X., Miao, X. shan, & Han, Z. bing. (2024). Synthesis and photocatalytic degradation performance of BiOBr nanoflowers with tunable exposed (001) facet and band gap. Inorganic Chemistry Communications, 164. https://doi.org/10.1016/j.inoche.2024.112386

Zhu, F., Zhan, Y., Chen, X., Chen, Y., Lei, Y., Jia, H., Li, Y., & Duan, X. (2024). Photocatalytic PAN Nanofibrous Membrane through Anchoring a Nanoflower-Branched CoAl-LDH@PANI Heterojunction for Organic Hazards Degradation and Oil-Containing Emulsified Wastewater Separation. Langmuir, 40(28), 14368–14383. https://doi.org/10.1021/acs.langmuir.4c00980

Zhu, J., Wen, M., Wen, W., Du, D., Zhang, X., Wang, S., & Lin, Y. (2018a). Recent progress in biosensors based on organic-inorganic hybrid nanoflowers. In Biosensors and Bioelectronics (Vol. 120, pp. 175–187). Elsevier Ltd. https://doi.org/10.1016/j.bios.2018.08.058

APPENDICES

APPENDIX A: Experimental Challenges

Preliminary Investigations on Biochar for Chloride Removal

Prior to the development of the BC–NFs and SAP–EGS materials presented in this thesis, a series of preliminary investigations was conducted to evaluate the feasibility of using biochar as a direct adsorbent for chloride removal. These experiments played an important role in understanding the limitations of conventional adsorption-based approaches and guided the development of the sustainable materials investigated in the main chapters of this thesis.

Five biochar obtained from three different suppliers were evaluated. Comprehensive physicochemical characterization, including FTIR, SEM, and BET surface area analysis, was performed to compare their structural and surface properties.

Before conducting adsorption experiments, the intrinsic chloride content of each biochar was evaluated by immersing the materials in deionized water for three days under batch conditions. The chloride concentration released from each biochar was quantified using a HACH DR3900 spectrophotometer equipped with TNT879 Chloride Test Kits (1–1000 mg/L Cl^-). As shown in Figure 22 The presence of background chloride was further verified using the silver nitrate ($AgNO_3$) precipitation test, which produced the characteristic formation of AgCl precipitates, confirming that all investigated biochar contained measurable intrinsic chloride.

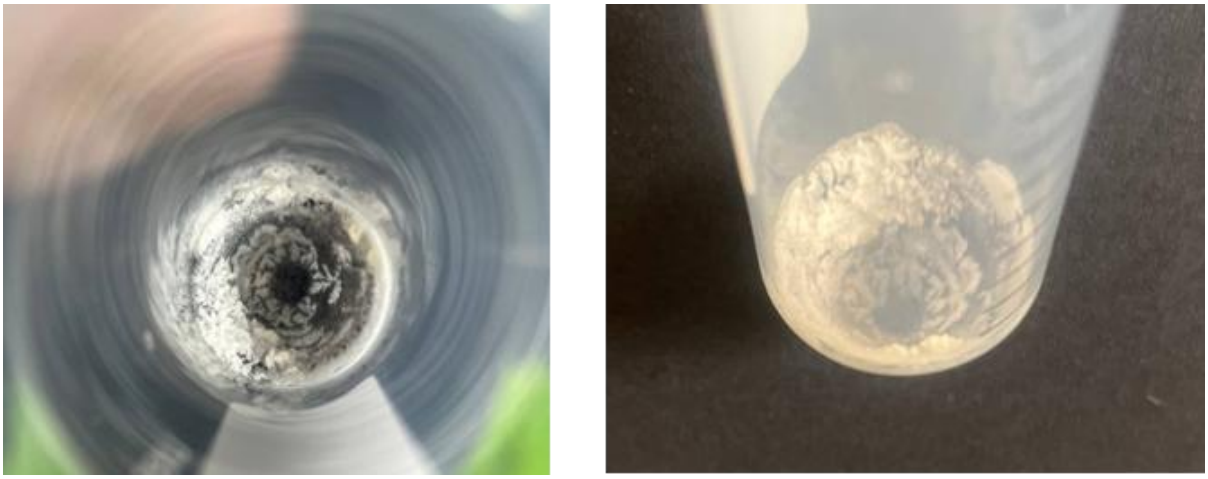

Figure 22- AgCl Precipitation on Biochar

Batch adsorption tests conducted using a three-day contact time demonstrated that unmodified biochar exhibited very limited chloride adsorption capacity, indicating that conventional biochar adsorption alone was insufficient for effective chloride removal.

Among the investigated materials, Bella biochar was selected for all subsequent experiments because it exhibited the lowest background chloride concentration among the high-surface-area biochar, together with a well-developed porous structure, a high BET surface area (377.1 $m^2 g^{-1}$), and abundant oxygen-containing surface functional groups. These characteristics provided a favorable platform for subsequent adsorption studies, surface modification, and the development of the BC–NFs composite.

Surface Functionalization of Biochar for Chloride Removal

To improve chloride adsorption, Bella biochar was subsequently modified using two commonly employed surface functionalization strategies.

The first approach involved coating the biochar with chitosan to introduce positively charged amine functional groups through a precipitation process (Bombuwala Dewage et al., 2018). The

second approach employed polyethyleneimine (PEI) grafting using glutaraldehyde as a cross-linking agent to increase the density of surface amine groups (T. Li et al., 2020).

The modified biochar was evaluated through chloride adsorption experiments and characterized using zeta potential measurements to assess changes in surface charge.

Both modification strategies successfully altered the surface chemistry of the biochar. Zeta potential analysis confirmed that the modification of chitosan and PEI shifted the surface charge toward more positive values, indicating the successful incorporation of amine-containing functional groups capable of enhancing electrostatic attraction toward chloride ions.

Despite these improvements, only a limited enhancement in chloride adsorption was observed. The results suggested that increasing positive surface charge alone was insufficient to overcome the inherently weak interaction between chloride ions and carbonaceous surfaces. The high hydration energy and low adsorption affinity of chloride ions likely limited the effectiveness of purely electrostatic adsorption mechanisms. These findings demonstrate that although surface functionalization successfully modifies the physicochemical properties of biochar, adsorption-based strategies alone cannot achieve satisfactory chloride removal.

Although the preliminary studies did not achieve the desired chloride removal performance, they provided valuable insight into material selection, surface modification strategies, and the need for alternative removal mechanisms.

APPENDIX B: Supplementary information for Chapter 2

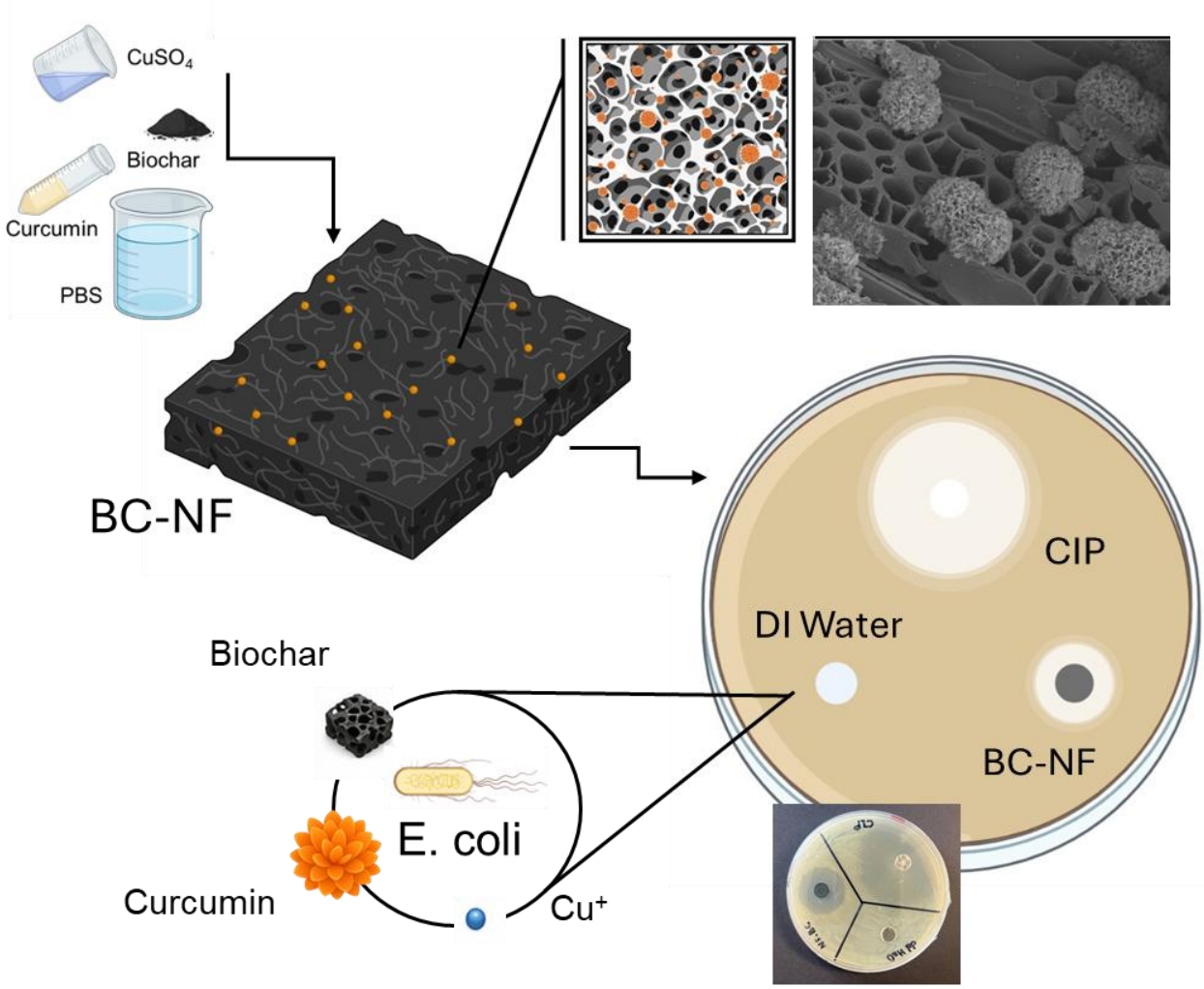

Figure 23- Schematic illustration of the synthesis and antibacterial evaluation of the biochar-supported curcumin–copper phosphate hybrid nanoflowers (BC–NFs). Curcumin and $CuSO_4$ were self-assembled in phosphate-buffered saline (PBS) to form copper phosphate hybrid nanoflowers directly on the biochar surface. The resulting BC–NFs composite was characterized by SEM and evaluated for antibacterial activity against Escherichia coli using the agar well diffusion method, with ciprofloxacin (CIP) and deionized (DI) water serving as the positive and negative controls, respectively.

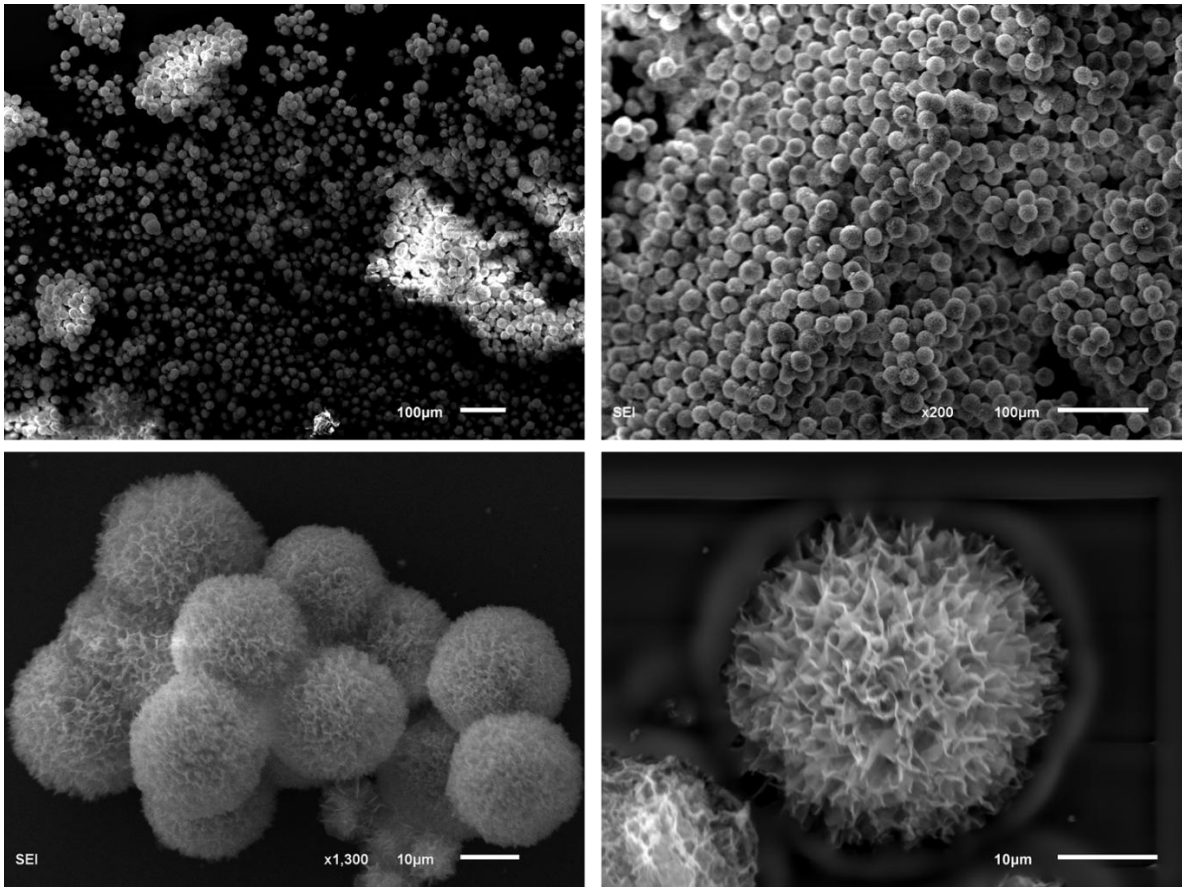

Figure 24- SEM images of CCPHNFs synthesized using 100 mM $CuSO_4$ in the presence of 0.5 µM curcumin. Four representative SEM images at different magnifications.

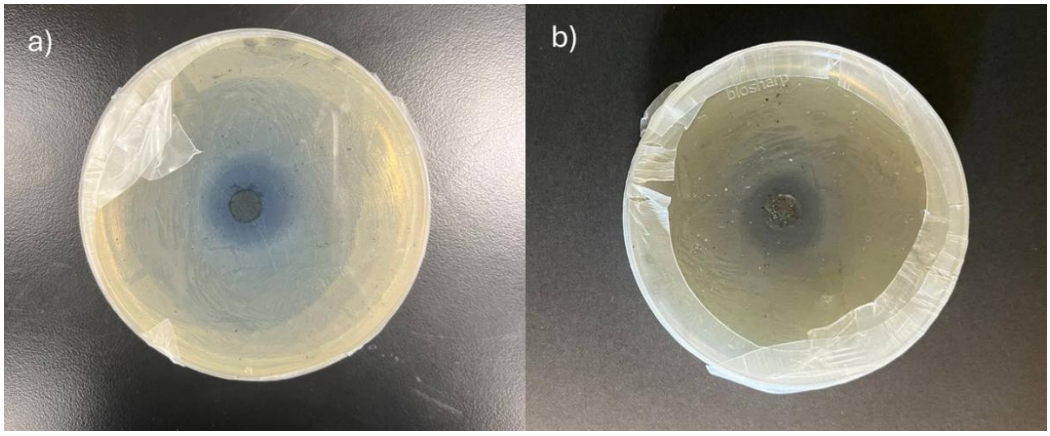

Figure 25- Antibacterial activity of the biochar-supported curcumin–copper phosphate hybrid nanoflowers (BC–NFs) against Escherichia coli determined by the agar well diffusion assay after ***(a)*** *18 h and* ***(b)*** *4 days of incubation. The BC–NFs composite maintained a distinct inhibition zone over the incubation period, indicating sustained antibacterial activity.*

APPENDIX C: Supplementary information for Chapter 3

Preliminary Chloride Removal Using Eggshell Powder

Prior to developing the SAP–EGS composite, preliminary adsorption experiments were conducted to evaluate the chloride removal capability of EGS powder alone.

Collected EGSs were thoroughly washed with deionized water to remove impurities, dried at room temperature, and ground into a fine powder. Swan Lake water samples (15 mL) were transferred into centrifuge tubes, and the solution pH was adjusted to 6.0 using dilute acetic acid. Subsequently, 1.5 g of EGS powder was added to each tube, and the suspensions were agitated on a mechanical shaker at 300 rpm for 24 h at room temperature.

After adsorption, the samples were centrifuged at 5000 rpm for 5 min to separate the solid and liquid phases. To recover the absorbed solution from the EGS matrix, 5 mL of methanol was added, followed by storage at 4 °C for approximately 4 h. The recovered solution was then analyzed for residual chloride concentration using the Hach DR3900 spectrophotometer (TNT879 chloride test kit).

The preliminary adsorption experiment demonstrated that EGS powder possesses an inherent ability to remove chloride from Swan Lake water. Under the optimized conditions (pH 6.0), the initial chloride concentration decreased from 244 mg L^{-1} to 121 mg L^{-1}, corresponding to a chloride removal efficiency of 50.4%.

The moderate chloride removal was attributed to the calcium carbonate-rich composition of EGSs, which provides active calcium sites capable of interacting with chloride ions. However, the adsorption capacity of EGS powder alone was insufficient for practical application because of its limited surface area, relatively slow mass transfer, and lack of a three-dimensional adsorption

network. These findings provided the rationale for incorporating EGS powder into a superabsorbent polymer matrix to improve water uptake, enhance chloride concentration within the hydrogel, and increase the overall chloride removal efficiency.



Figure 26- White salt precipitate observed following the preliminary chloride removal experiment using EGS powder after methanol extraction and cooling at 4 °C.

Study of Swelling and Adsorption

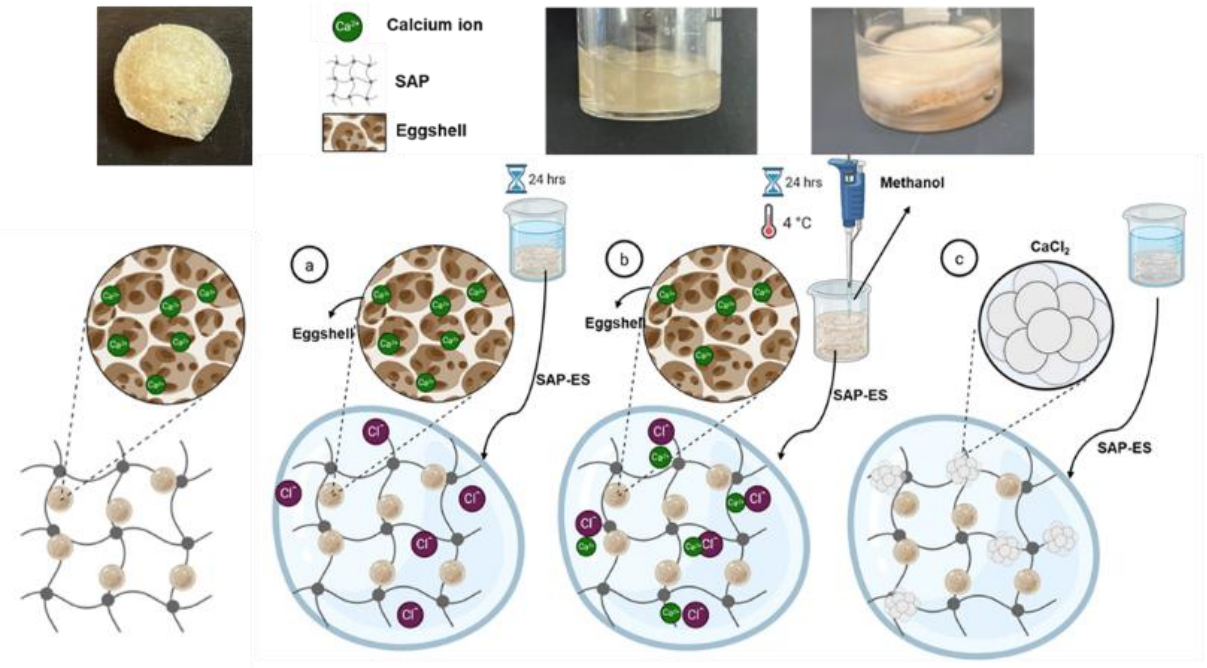

Figure 27- Proposed mechanism of chloride removal by the SAP–EGS. (a) The SAP–EGS hydrogel absorbs chloride-containing water while calcium ions are gradually released from the incorporated EGS particles. (b) Methanol addition promotes water desorption from the swollen hydrogel, increasing ion concentration and facilitating interactions between calcium and chloride

ions. (c) Upon cooling at 4 °C, calcium-assisted chloride precipitation occurs within the hydrogel matrix, enabling chloride removal from the aqueous phase.

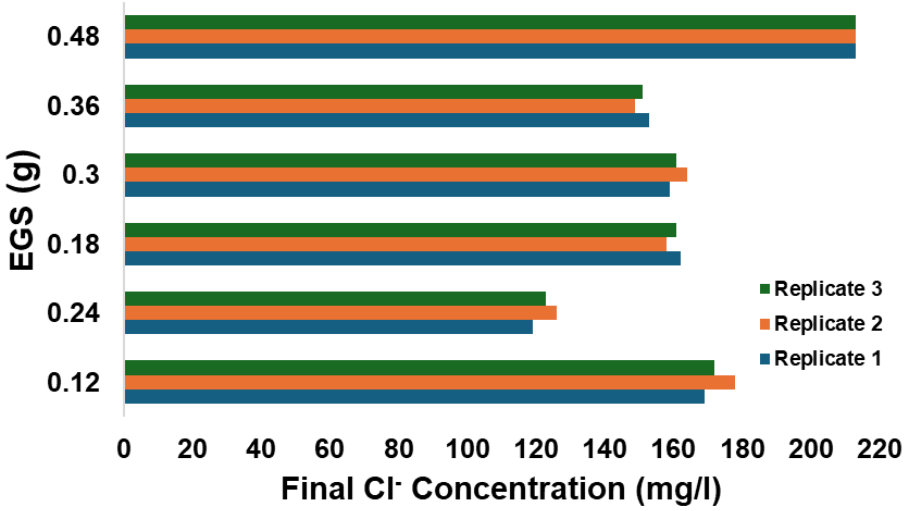

Figure 28- Raw triplicate measurements of the final chloride concentration for different EGS loadings used during optimization of the SAP–EGS composite. Each treatment was performed in triplicate (n = 3) under identical experimental conditions.

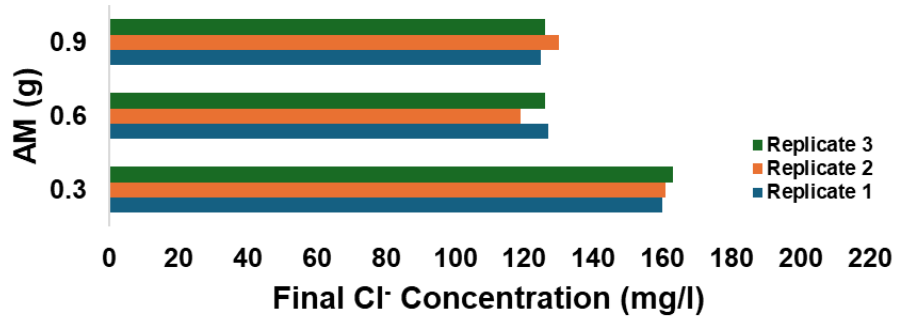

Figure 29- Raw triplicate measurements of the final chloride concentration for different acrylamide (AM) contents during optimization of the SAP–EGS composite. Each formulation was tested in triplicate (n = 3) under identical experimental conditions.

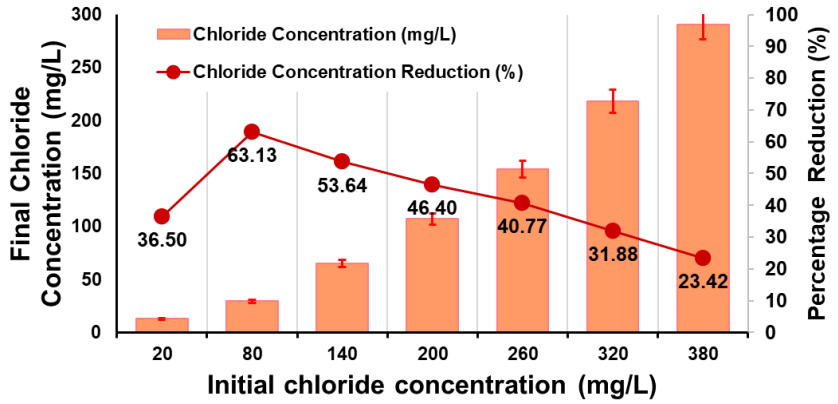

Figure 30- Effect of the initial chloride concentration on the chloride removal performance of the optimized SAP–EGS composite. Bars represent the final chloride concentration after treatment, while the line indicates the corresponding chloride reduction efficiency. Error bars represent the standard deviation of triplicate measurements (n = 3).

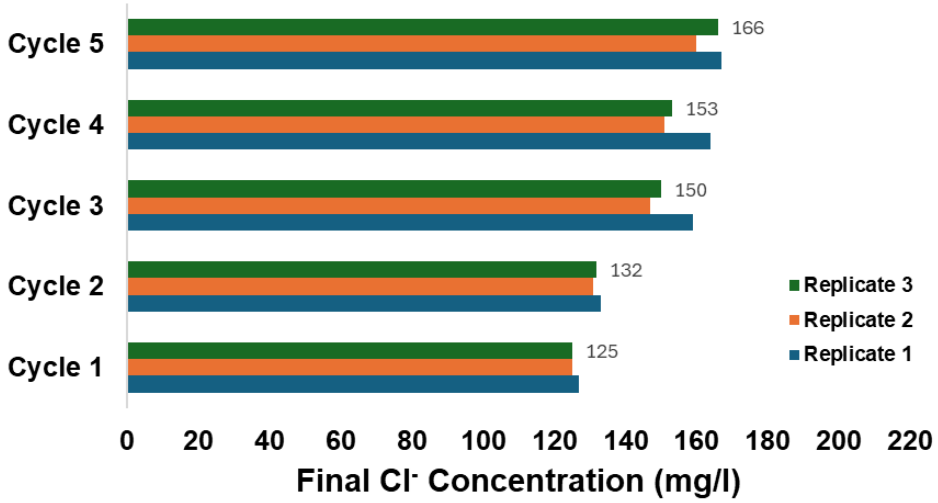

Figure 31- Raw triplicate measurements of the final chloride concentration obtained during five consecutive adsorption–desorption cycles of the optimized SAP–EGS composite. Each cycle was performed in triplicate (n = 3) to evaluate the reusability and stability of the composite.

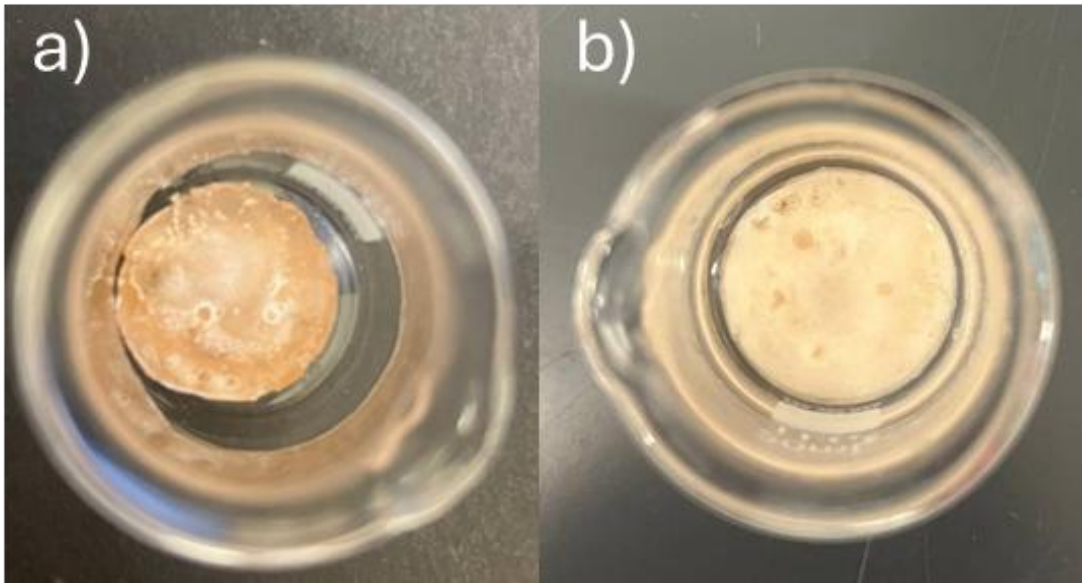

Figure 32- Representative photographs of the SAP–EGS hydrogel (a) before and (b) after the chloride removal experiment, illustrating the physical appearance of the composite following adsorption and methanol-assisted chloride precipitation.

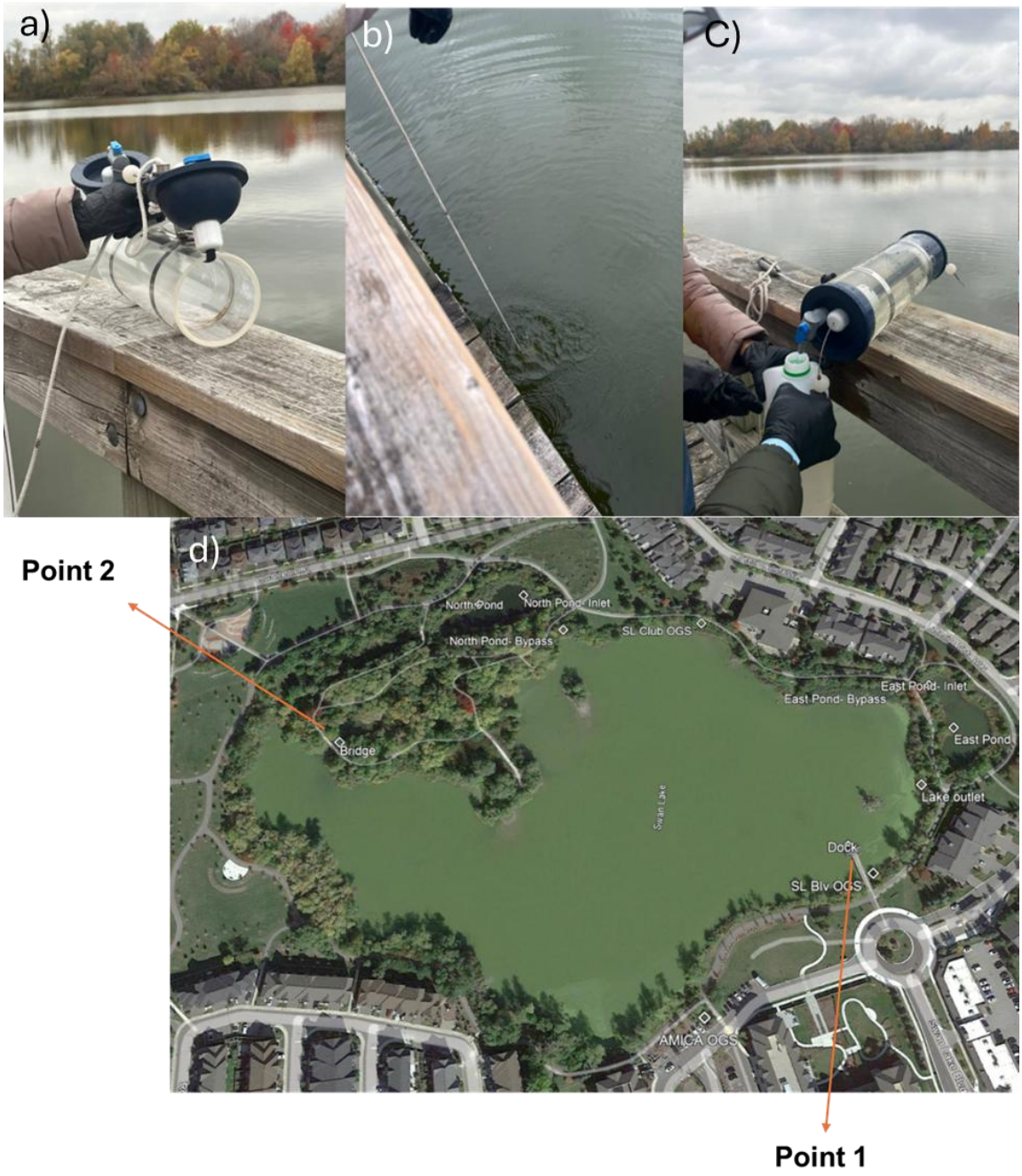

Figure 33- Water Sampling Procedure and Sampling Locations at Swan Lake, Markham, Ontario. (a) Preparation of the water sampling device prior to collection. (b) Collection of water samples from the lake using a depth sampler. (c) Transfer of collected water into a clean sample bottle for laboratory analysis. (d) Aerial map of Swan Lake showing the water sampling locations, including the Bridge and Dock sampling sites.

Absorption Isotherm Analysis

Table 10. Experimental equilibrium chloride concentrations (Ce), adsorption capacities (qe), and transformed parameters used for Freundlich and Langmuir adsorption isotherm modeling.

Ce	qe	Log (Ce)	Log(qe)	Ce/qe
12.7	0.024	1.10380372	-1.62	528.87
29.5	0.16	1.46982202	-0.78	177.58
64.9	0.24	1.8122447	-0.61	262.71
107.2	0.30	2.03019479	-0.51	351.17
154	0.35	2.18752072	-0.46	441.66
218	0.33	2.33845649	-0.47	649.72
291	0.29	2.46389299	-0.53	993.97